Thermally Poled Fibre Devices

Wei Xu

March, 1999

Thesis submitted in fulfillment of the requirement of the University of Sydney, Australia for the award of the degree of Doctor of Philosophy (Ph.D.).

Declaration of Originality

To the best of my knowledge and belief, I hereby declare that this thesis is my own work and that any work in this thesis which is not my own has been duly referenced and/or acknowledged. It contains no material previously published or written by another person nor materials which to a substantial extent has been accepted for the award of any other degree or diploma of a university or other institute of higher learning. All other forms of dissemination of this thesis follow the standard procedures as outlined in the University of Sydney Statutes.

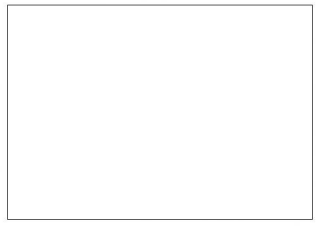

Wei Xu

March 1999

To my parents and two sisters

Acknowledgements

Nothing would be done successfully without help from others. I, therefore, would like to acknowledge those people who gave me encouragement, advice as well as sharing disappointments, ups and downs.

I would like to thank my supervisor Dr. Simon Fleming, Technical Director of the Optical Fibre Technology Centre at the University of Sydney, for his wisdom and understanding, for his careful guidance, and for his constant encouragement and his friendship. Simon's broad knowledge and comprehension of science have astounded me all the time. I would also like to thank my co-supervisor, Dr. Ian Bassett, for introducing me to the field of optical fibre technology.

I am deeply indebted to Dr. Danny Wong, the manager of the poling project. His perfect management abilities, state-of-art technical skills, stimulating discussions, constant encouragement deserve specific thanks. I could not write this thesis without his professional instructions. I am indebted to his critical reading of the entire manuscript and his constantly reminding me of writing up this thesis. His friendship is gratefully acknowledged.

I would like to express my sincere thanks to Dr. Peter Hill, Dr. Hugh Inglis, Dr. Mark Janos, and Jesper Arentoft, who worked with me in the poling project. Their

knowledge in silica glass, their technical skills in fibre optics, their stimulating suggestions, and their constant interest in poling deserve specific thanks. Special thanks go to Dr. Danny Wong and Dr. Mark Janos because we worked together to build up two sets of very nice Mach-Zehnder interferometers and develop the *in situ* measurement technique. Thanks are also due to Thomas Ryan and Rodney Hall, who are working on the poling project. I would love to express my deep thanks to Dr. Danny Wong, Ron Bailey, Andrew Higley, Justin Digweed and Thomas Ryan for fabricating the preforms and fibres.

I would like to thank Dr. Kai Ming Lo for calculating the modal distributions and the cutoff value of the twin-hole fibres. I feel very grateful to Dr. Shane Huntington for etching thermally poled silica fibres in HF acid and carrying out the atomic force microscopic measurements on them. Dr. John Canning deserves specific thanks for stimulating suggestions and constant encouragement. I would also like to express my thanks to Dr. Yuxing Zhao, Dr. Dmitrii Stepanov, Dr. Adrian Carter, Dr. Leon Poladian, Dr. Martijn de Sterke, Dr. David Moss, Dr. Francois Ouellette and Dr. Peter Krug for their help and interest.

I would like to express many thanks to the Optical Fibre Technology Centre for providing a very friendly and state-of-art academic environment. My deep thanks also go to Congji Zha and Zourab Brodzeli for sharing an office with me. They also share my ups and downs.

Now, I would like to thank Dr G. Fergus Brand and Dr. Brian James, Postgraduate Coordinators of School of Physics at the University of Sydney for guiding me to win an Overseas Postgraduate Research Scholarship from the Department of Employment, Education, Training and Youth Affairs of Australia. They also support me to carry out my PhD project at the Optical Fibre Technology Centre.

I am deeply indebted to Dr. Simon Fleming and Dr. Danny Wong for employing me as a part-time research assistant throughout the years of my degree. The financial support from Australian Photonics, IBM Australia, ABB Sweden, Transgrid Australia, the New Energy and Industrial Technology Development Organization of Japan are gratefully acknowledged.

Finally, thanks to my parents and my two older sisters for their support throughout the years of my degree.

Abstract

Poling of silica glass, silica fibre and silica planar waveguides is an exciting research field. The thermal poling technique has been demonstrated to produce large second order nonlinearities and linear electro-optic coefficients in silica glass, silica fibre and silica planar waveguides. In this thesis, efforts have been made both to obtain large, stable and reliable linear electro-optic coefficients in silica fibre using thermal poling and to understand the mechanisms for the thermal poling effects in silica fibre.

Firstly, the thermal poling conditions for boron co-doped germanosilicate fibre were optimized and the dependence of the thermal poling induced linear electro-optic coefficient on the poling voltage, poling temperature and poling time were analyzed. To improve the efficiency of optimizing the poling conditions for different types of silica fibre, an *in situ* poling technique was deployed to study aluminum co-doped germanosilicate fibre. It is found that the thermal poling history has significant influence on the induced linear electro-optic effect. Furthermore, the *in situ* technique was also employed to measure and analyze the decay behavior of the induced linear electro-optic coefficient in boron co-doped germanosilicate fibre.

Secondly, an innovative method was proposed to investigate the frozen-in fields existing in the thermally poled fibres. The frozen-in fields are the cause for the induced linear electro-optic effect in silica fibre. This method can be used to measure

both the magnitude and the direction of the frozen-in fields. Furthermore, this method is able to measure the third order nonlinearity of the fibre core. It is the first time that it has been observed that the third order nonlinearity of the fibre core increases after thermal poling.

Next, it was found that the time evolution of the linear electro-optic coefficient in thermally poled silica fibre is very different for different polarity of the poling voltage. There are two distinct processes in thermal poling: the faster linear process of charge migration and the subsequent single exponential process of charge ionization. It is the first time that it has been shown that there are two frozen-in fields in thermally poled fibre: the shielding field and the ionization field. Both the fields are able to produce a linear electro-optic effect in silica fibre. Furthermore, It was found that the charge distributions in thermally poled fibre could move during thermal poling. It is the first time that the competition between the shielding field and the ionization field seen by the core has been analyzed and it is shown to be a linear process. The third order nonlinearity of the poled fibre core is fairly constant during this competition, but it is still larger than that of the unpoled fibre core.

Finally, the thermal poling technology and the Bragg grating technology were integrated to demonstrate a single fibre (low frequency) intensity modulator.

Publication List

1. W. Xu, D. Wong, and S. Fleming, "Evolution of the linear electro-optic coefficient and the third order nonlinearity in prolonged negative thermal poling," submitted to Electronics Letters.
2. D. Wong, W. Xu, and S. Fleming, "Charge dynamics and distributions in thermally poled silica fibre," submitted to SPIE/Photonics East'99, Boston, USA, 1999.
3. W. Xu, J. Arentoft, D. Wong, and S. Fleming, "Evidence of space-charge effects in thermal poling," submitted to IEEE Photonics Technology Letters.
4. W. Xu, M. Janos, D. Wong, and S. Fleming, "Thermal poling of boron-doped germano-silicate fibre," submitted to IEICE Transactions on Communications and IEICE Transactions on Electronics, Japan.
5. M. Janos, W. Xu, D. Wong, H.G. Inglis and S. Fleming, "Growth and decay of the electro-optic effect in thermally poled B/Ge co-doped fibre," submitted to Journal of Lightwave Technology.
6. D. Wong, W. Xu, J. Arentoft, and S. Fleming, "Positive and negative thermal poling of germanosilicate fibres," Technical Digest of OFC/IOOC'99 (Thursday, February 25), ThG4, pp. 90-92, San Diego, USA, 1999.
7. J. Arentoft, M. Kristensen, J. Hübner, W. Xu, and M. Bazylenko, "Poling of UV-written wave-guides," Technical Digest of OFC/IOOC'99 (Wednesday, February 24), WM19, pp. 250-252, San Diego, USA, 1999.

8. D. Wong, W. Xu, S. Fleming and M. Janos, "Recent results with thermal poling of fibre," Proceedings of SPIE, vol. 3542, pp. 120-123, 1998.

9. D. Wong, W. Xu, S. Fleming, M. Janos, and K. M. Lo, "Frozen-in field in thermally poled fibres," invited paper in Optical Fiber Technology.

10. W. Xu, M. Janos, D. Wong, and S. Fleming, "Optimisation of poling conditions for thermal poling of boron-doped germanosilicate fibre," Technical Digest of the Third Optoelectronics and Communications Conference (OECC'98), Japan, pp. 516-517, July 1998.

11. D. Wong, W. Xu, R. Hall, and M. Janos, "Thermal poling of aluminium co-doped germano- silicate fibres," Proceedings of the 23rd Australian Conference of Optical Fibre Technology, pp.197-200, Melbourne, Australia, July 1998.

12. W. Xu, D. Wong, S. Fleming, M. Janos, and K. M. Lo, "Direct measurement of frozen-in field in thermally poled fibres," Proceedings of the 23rd Australian Conference of Optical Fibre Technology (ACOFT'98), pp. 201-204, Melbourne, Australia, July 1998.

13. D. Wong, W. Xu, M. Janos, J. Chow, R. Hall, and S. Fleming, "Time evolution of electro-optic effect in fibre during thermal poling," Japanese Journal of Applied Physics, vol. 37, Suppl. 37-1, pp. 68-70, 1998.

14. D. Wong, W. Xu, M. Janos, J. Chow, R. Hall, and S. Fleming, "Evolution of electro-optic effect in fibre during poling", International Workshop on "Structure and Functional Optical Properties of Silica and Silica-Related Glasses", Shizuoka, Japan, July 10-11, 1997.

15. D. Wong, S. Fleming, H.G. Inglis, and W. Xu, "Poled fibre devices", Invited paper, Conference Proceedings of LEOS'96, 9TH Annual Meeting, IEEE Lasers and Electro-Optics Society, Boston, WC1, P15, 1996.

16. S. Fleming, D. Wong, H.G. Inglis, W. Xu, T. Fujiwara and P. Hill, "Poled fibre devices for electro-optic modulation", Invited paper, Proceedings of SPIE, vol. 2893, pp. 450-460, 1996.

Table of Abbreviations

DWDM	Dense Wavelength Division Multiplexing
EFILEOM	Electrical Field Induced Linear Electro Optic Modulation
EFISH	Electrical Field Induced Second Harmonic Generation
INAA	Instrumental Neutron Activation Analysis
LEO	Linear Electro Optic
MCVD	Modified Chemical Vapor Deposition
MZI	Mach-Zehnder Interferometer
NA	Numerical Aperture
SHG	Second Harmonic Generation
SON	Second Order Nonlinearity
TE Mode	The mode's polarization is parallel to the poling field
TM Mode	The mode's polarization is orthogonal to the poling field
UV	Ultra Violet

Contents

Chapter 1 Introduction to Poling

1.1 Why Poling of Bulk Silica Glass, Silica Fibres & Planar Waveguides?

Optical glass fibres and waveguides play a ubiquitous role in the telecommunications industry. Low-loss silica fibres led to a telecommunications revolution in the early 1980s. Low-loss silica waveguides are used to produce a variety of optical integrated circuits, such as optical splitters, filters, switches and routers. However, unlike its related quartz crystalline phase, the glass matrix is amorphous with macroscopic inversion symmetry and thus has zero second-order nonlinearity (SON), which forbids second-order nonlinear processes and linear electro-optic (LEO) modulation. Therefore, the availability of SON or LEO coefficient in silica fibres and waveguides will result in many new active fibre and waveguide devices, for example, electro-optic modulators and switches, electrically tunable Bragg gratings and long period gratings, frequency converters and parametric oscillators, etc. Potential devices for spectral inversion, all-optical switching through cascading of nonlinearities and up- and down-conversion can also be realized. Silica glass has excellent properties, such as low optical losses, wide transparent range, low dispersion, high optical damage threshold, low cost, high environmental durability, good fibre connectivity and straightforward integrability with silicon and silica fibre networks. These unbeatable properties would ensure widespread use of active silica devices with SON and LEO coefficients.

The most promising way of realizing useable SON and LEO coefficients in silica is the process of poling, whereby a large external field is applied to the material simultaneously with suitable perturbations, such as heat/temperature enhancement [1.1, 1.2], and UV light irradiation [1.3, 1.4, 1.5].

1.2 Review of Poling of Silica Glass, Silica Fibres & Planar Waveguides

In the late 1980's Österberg and Margulis discovered unusually efficient second-harmonic generation (SHG) in phosphorous-doped silica fibre pre-treated by optical fields [1.6]. Using 1064 nm pump light with input intensities of 100-200 GW/cm, they found conversion efficiencies as high as 5% in silica fibre less than one meter long after 532 nm harmonic light had built up over many hours. Stolen and Tom proposed that the SHG was due to electrical-field-induced nonlinearities in which the field arises from a third-order optical rectification process [1.7]. Bergot *et al.* showed large permanent enhancements in second-order optical nonlinearity in germanosilicate fibre by application of a transverse DC electrical poling field in the presence of high-intensity light [1.8]. Furthermore, Kashyap demonstrated phase-matched electric-field-induced second-harmonic generation in silica fibre using a simple interdigitated electrode structure, which can be rotated to permit phase matching between all propagating modes [1.9]. A conversion efficiency of 4.0×10^{-4}% has been obtained on unoptimized devices. Ouellette *et al.* found that a combined hydrogen and heat treatment resulted in an average enhancement of second-harmonic conversion efficiency in silica optical fibre by as much as a factor of 4 [1.10]. Nevertheless, the

phenomenon of SHG in silica fibres showed that the levels of the second order nonlinearity are typically three to four orders of magnitude less than in the nonlinear crystals such as $LiNbO_3$.

In 1991, however, Myers *et al.* induced a second order nonlinear coefficient $\chi^{(2)}$ of ~1 pm/V (~0.2 $\chi_{22}^{(2)}$ of $LiNbO_3$) into commercial fused-silica optical flats by means of thermal poling at temperatures of 250-325 °C with an electrical field of $\sim 5\times10^6$ V/m [1.1]. This excited extensive scientific and commercial interest in inducing $\chi^{(2)}$ into silica. In addition to thermal poling, different poling techniques were developed to induce $\chi^{(2)}$ into silica. In 1992, Okada *et al.* obtained $\chi^{(2)}$ of ~1 pm/V in glass films using a corona poling technique [1.11]. Kazansky *et al.* used an electron-beam implantation method to achieve $\chi^{(2)}$ in lead silicate glass as high as 0.7 pm/V in 1993 [1.12]. Kazansky *et al.* also employed vacuum poling for improving reproducibility and quality of the induced second-order susceptibility [1.13]. In 1995, Fujiwara *et al.* induced an electro-optic coefficient r of ~6 pm/V (i.e. $\chi^{(2)}$ of ~12 pm/V) into germanosilicate fibres using UV-excited poling [1.3]. More recently, Fujiwara *et al.* obtained d_{33} of ~3.4 pm/V (i.e. $\chi_{33}^{(2)}$ of ~6.8 pm/V) in Ge-doped bulk silica glass by UV-excited poling as well [1.4, 1.14].

While developing different poling techniques to enhance the induced second-order nonlinearities, researchers carried out tremendous materials studies of poling. Observation of second harmonic generation has been reported in silica glass fibre

doped with GeO_2 and P_2O_5 [1.8], aluminosilicate glass fibre doped with rare earth [1.15], fused bulk silica glass [1.1], and glass film [1.11, 1.16]. Tanaka *et al.* demonstrated second harmonic generation in electrically poled tellurite glass in 1993 [1.17]. Moreover, Tanaka *et al.* reported highly efficient optical second harmonic generation in poled Ti-doped silica glasses in 1995 [1.18]. The second-order nonlinearity, d_{33}, of the TiO_2 and SiO_2 glasses ranges from 0.2 to 0.5 pm/V. Hirama *et al.* reported a large second-order nonlinearity d_{33} of 7.5 pm/V, i.e. $d_{33} = 15 \times d_{11}$ (quartz d_{11}=0.5 pm/V [1.11, 1.19]), from Sol-Gel processed poled silica and germanosilicate thin films in 1996 [1.20]. Garcia *et al.* induced a large second-order nonlinearity in alkali-rich glasses, i.e. soft glasses, such as soda lime glass by thermal poling in 1998 [1.21].

In addition to the fundamental research activities on silica poling, people have attempted to make useful active devices from poled silica fibres and waveguides. Li and Payne first demonstrated linear electro-optic modulation in optical fibres in 1989 [1.22]. They poled twin-hole fibres at room temperature using internal gallium electrodes and obtained an electro-optic coefficient of ~0.002 pm/V. In 1994, Long *et al.* measured the linear electro-optic coefficients in thermally poled fused bulk silica and obtained r_{31} of ~0.1 pm/V and r_{33} of ~0.3 pm/V [1.23]. Moreover, they also reported an electro-optic coefficient of $r = 0.05 \pm 0.02$ pm/V for temperature/electric field poled Ge:SiO_2 fibres [1.24]. Kazansky *et al.* obtained an electro-optic coefficient of 0.05 pm/V in silica fibres using vacuum thermal poling [1.25], which is about 25 times higher than the results of Li and Payne. Fujiwara *et al.* achieved the half-wave

voltage and electrode overlap length product $V_\pi L$ of 32 Vcm in UV-excited poled twin-hole germanosilicate fibres [1.3] and of 244 Vcm in thermally poled twin-hole germanosilicate fibres [1.26]. Long *et al.* demonstrated a half-wave voltage of 75 V for a 12-cm electrode overlap length in thermally poled D-shape fibres [1.27]. The corresponding electro-optic coefficient was 0.3 pm/V and did not show any decay at room temperature for over four months. Fujiwara *et al* demonstrated electrical tuning of a Bragg grating of 0.01 nm in 1V/μm and a corresponding intensity modulation of 10 dB for 300 V applied voltage [1.28].

Regarding the applications of electro-optic modulation to silica planar waveguides, Liu *et al.* demonstrated electro-optic phase modulation in a thermally poled fused-silica channel waveguide in 1994 [1.29]. A phase shift of 32 mrad was measured at λ = 633 nm for a device interaction length of 4.8 mm and an applied electric field of 7.3 V/μm in the channel waveguide. Abe *et al.* reported a 2×2 electro-optic switch in an integrated Mach-Zehnder interferometer constructed with thermally poled GeO_2-SiO_2 channel waveguides on a silicon substrate in 1996 [1.30]. The switching voltage is 1700 V and the electro-optic coefficient is estimated about 0.02 pm/V. Margulis *et al.* fabricated single mode channel waveguides in soda lime glass by thermal poling in 1997 [1.31]. The refractive index of the glass was reduced by 1.5% due to the depletion of sodium ions, making possible the formation of waveguides in a depressed cladding configuration.

For the applications of poled silica fibres to frequency doubling, Kazansky *et al.* reported CW quasi-phase-matched frequency conversion to the blue light in thermally poled optical fibres in 1995 [1.32]. The experimental bandwidth of phase-matched second harmonic conversion in poled silica fibres (0.78 nm cm) is an order of magnitude larger than in an equal length of the periodically poled bulk lithium niobate (0.06 nm cm). Pruneri *et al.* increased the second harmonic conversion efficiency by a factor of ~10 in comparison with the previous results in Ref. 1.32 in 1997 [1.33]. Furthermore, Pruneri *et al.* generated blue powers up to ~76 μW at ~422 nm with an average second harmonic conversion efficiency of ~0.22 % in periodically poled D-shape silica fibres in 1997 [1.34, 1.35]. Pruneri *et al.* also reported efficient quasi-phase-matched frequency conversion around 1.5 μm in periodically poled D-shape silica fibres in 1998 [1.36]. By frequency doubling ~100 fs pulses in a second-order nonlinear grating ~ 4 cm long and with a period of 57.15 μm, ~1.05 mW average power at 768 nm has been generated, with an average conversion efficiency ~1.2 %.

1.3 Poling Techniques for Silica Fibres

1.3.1 In-core Optical Irradiation Poling

Fig. 1.1 shows the in-core optical irradiation poling. The laser beam at the wavelength of 488 nm is launched into the fiber core while the poling voltage is applied to the fibre. A fibre was poled using this technique [1. 37]. The 488 nm blue laser with ~150 mW was focused into the fibre core for 1 hour with a poling voltage of 2 kV. The induced residual LEO coefficient is ~ 0.04 pm/V.

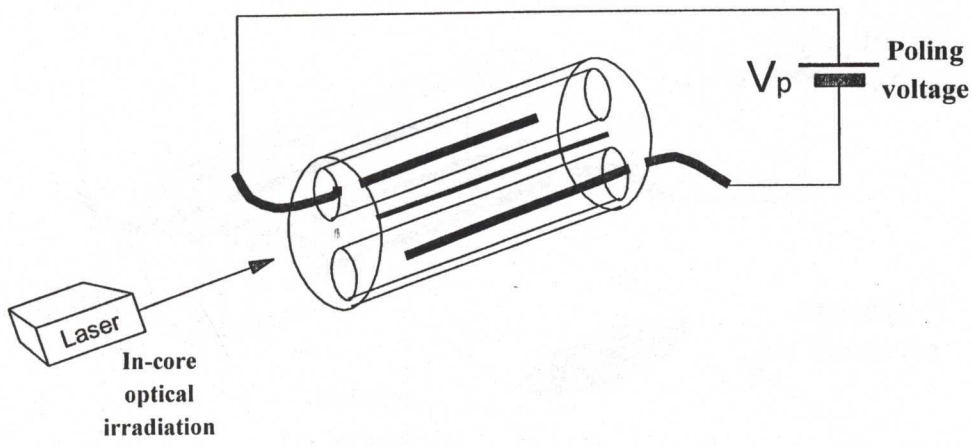

Fig. 1.1 In-core optical irradiation poling setup (after Wong *et al.* [1.38]).

1.3.2 UV Poling

UV poling is carried out in two ways, as shown in Fig. 1.2. One is side UV uniform irradiation and the other is side UV periodic irradiation. The periodic UV irradiation is by placing a phase mask in front of the fibre device before irradiation, and has the advantage of poling a fibre and writing a grating into the fibre simultaneously. The poling voltage is always turned on before UV irradiation begins and turned off after UV irradiation finishes. Different types of silica fibres were UV poled. 193 nm UV laser pulses are used for UV poling. The intensity of the laser pulses used is between 40 mJ/cm^2 and 100 mJ/cm^2. The poling voltage ranges from 1 kV to 4.5 kV. The poling time ranges from a few seconds to a few hours. However, the maximum LEO coefficient induced by UV poling is as little as ~0.02 pm/V. This result is very different from those reported by Fujiwara [1.3, 1.4].

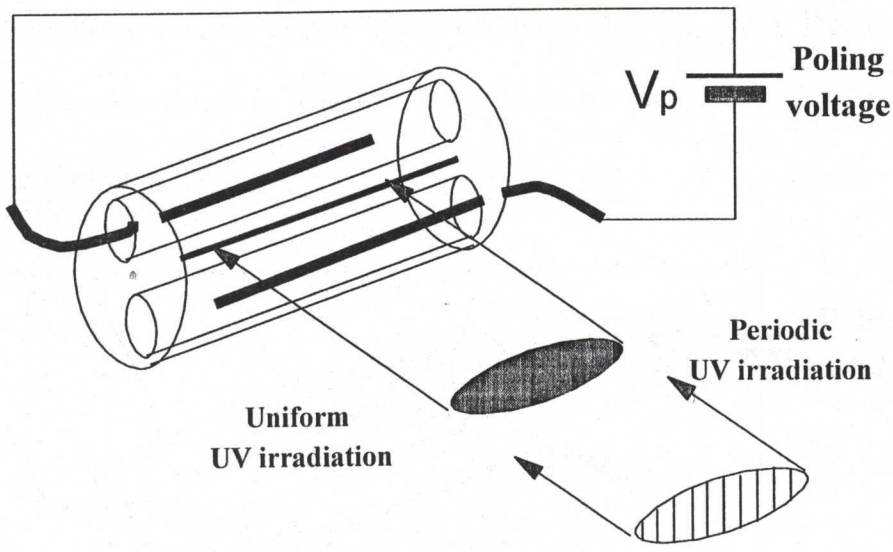

Fig. 1.2 UV poling setup (after Wong *et al.* [1.38]).

1.3.3 Thermal Poling

Thermal poling is shown in Fig. 1.3. Thermal poling of a twin-hole fibre device is carried out using the following procedure. Firstly, the fibre device under test is placed on a heater block at room temperature and the poling voltage is applied to the fibre device. Secondly, the heater is turned on. An elevated and stable temperature can be achieved within seconds. The temperature of the heater is controlled with an accuracy of ±1 °C. Next, at the end of a defined poling duration, the device is cooled down to room temperature within seconds while the poling voltage is still applied. Finally, when the device reaches room temperature, the poling voltage is switched off and the device is tested for its electro-optic coefficient using a Mach-Zehnder interferometer.

Thermal poling has been demonstrated to produce an appreciable magnitude of SON and LEO coefficients in silica glass and silica fibres [1.1, 1.2, 1.26]. Due to its high reproducibility, this thesis is therefore devoted to the detailed studies of thermal poling of silica fibres.

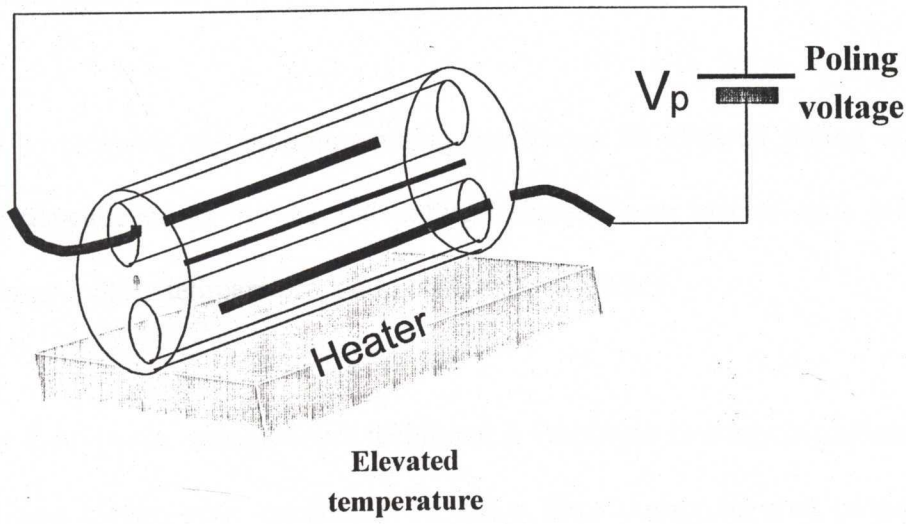

Fig. 1.3 Thermal poling setup (after Wong *et al.* [1.38]).

1.4 Organization of the Thesis

The main objective of the thesis is to investigate the mechanisms of the thermal poling effects in silica fibre for both scientific interest and commercial applications. With the understanding of the mechanisms, a large, stable and reliable linear electro-optic effect can then be induced into silica fibres for practical applications using the thermal poling technology.

Chapter 2 provides the technology background of the thermal poling experiments. It begins with the introduction of the twin-hole fibre devices. The cross sectional geometry and constituents of the fibres, and the structure and manufacture of the fibre devices are described in detail. The experimental setups for thermal poling of silica fibres are then introduced.

Chapter 3 investigates the optimum poling conditions for thermal poling of silica fibre. The dependence of the thermal poling induced linear electro-optic effect on poling voltage, poling temperature, and poling time is studied.

In Chapter 4, an *in situ* measurement technique is employed to study evolution of the induced linear electro-optic coefficient in silica fibre during thermal poling. The information about the evolution of the induced linear electro-optic coefficient is very helpful in understanding the poling mechanisms. The *in situ* method is also very useful and convenient for optimizing the thermal poling conditions, compared to the optimization procedures used in Chapter 3. In addition to the thermal poling conditions studied in Chapter 3, the poling history is revealed to have significant influence on the induced linear electro-optic effect in silica fibre.

Chapter 5 studies stability of the induced linear electro-optic effect in silica fibre. It is found that the decay behavior of the linear electro-optic coefficient is a stretched exponential process with distribution of relaxation times. This behavior is similar to the decay of Bragg gratings in silica fibre. However, the activation energy of the

induced linear electro-optic coefficient is smaller than that of Bragg gratings. The thermal poling induced linear electro-optic effect in silica fibre is not as stable as fibre Bragg gratings.

Chapter 6 is devoted to the investigation of the mechanisms of thermal poling of silica fibre. It is the first time that the frozen-in field in thermally poled fibre has been measured. This chapter describes a method to measure both the magnitude and the direction of the frozen-in field. The measurement technique is also suitable to measure the third order nonlinearity of the fibre core. Using this technique, it is observed for the first time that the third order nonlinearity of the fibre core has increased after thermal poling of the fibre. Furthermore, thermal poling of the fibre with different polarity of poling voltage gives very different poling dynamics. This significant difference in the *in situ* poling processes suggests that two processes take place during thermal poling: charge migration and charge ionization. The charge migration gives the shielding field, and the charge ionization leads to the ionization field. Both fields can be frozen-in at room temperature and can produce linear electro-optic effects in silica fibre. A series of experiments on negative thermal poling of silica fibre suggests movement of charge distributions in thermally poled fibre. The consequence of the movement of charge distributions is that the fibre core can "see" either the shielding field or the ionization field or both. The competition between the shielding field and the ionization field seen by the core is a linear process. It is interesting that the third order nonlinearity of the fibre core is fairly constant during this competition although it is still larger than that of an unpoled fibre. Based on the experimental evidence, the

mechanism of the thermal poling effects in silica fibre is due to the space charge distributions and the associated frozen-in fields in thermally poled fibre.

Chapter 7 demonstrates an application of the thermal poling effects in silica fibre ----- a simple intensity modulator using a poled in-fibre Bragg grating. A Bragg grating is first written into the silica fibre. The silica fibre is then thermally poled. The reflectance of the grating can be electrically tuned using the linear electro-optic effect induced into the silica fibre.

Finally, Chapter 8 summarizes the main results of the thesis.

1.5 References

[1.1] R. A. Myers, N. Mukherjee, and S. R. J. Brueck, "Large second-order nonlinearity in poled fused silica," Opt. Lett., vol. 16, pp. 1732-1734, 1991.

[1.2] P. G. Kazansky, P. St. J. Russell, and H. Takebe, "Glass fiber poling and applications," Journal of Lightwave Technology, vol. 15, pp. 1484-1493, 1997.

[1.3] T. Fujiwara, D. Wong, Y. Zhao, S. Fleming, S. Poole and M. Sceats, "Electro-optic modulation in germanosilicate fibre with UV-excited poling," Electron. Lett., vol. 31, pp. 573-574, 1995.

[1.4] T. Fujiwara, M. Takahashi, and A. Ikushima, "Second-harmonic generation in germanosilicate glass poled with ArF laser irradiation," Appl. Phys. Lett., vol. 71, pp. 1032-1034, 1997.

[1.5] S. Fleming, D. Wong, H.G. Inglis, W. Xu, T. Fujiwara and P. Hill, "Poled fibre devices for electro-optic modulation", Invited paper, Proceedings of SPIE, vol. 2893, pp. 450-460, 1996.

[1.6] U. Österberg and W. Margulis, "Dye laser pumped by Nd:YAG laser pulses frequency doubled in a glass optical fiber," Opt. Lett., vol. 11, pp. 516-518, 1986.

[1.7] R. H. Stolen and H. W. K. Tom, "Self-organized phase-matched harmonic generation in optical fibers," Opt. Lett., vol. 12, pp. 585-587, 1987.

[1.8] M.-V. Bergot, M. C. Farries, M. E. Fermann, L. Li, L. J. Poyntz-Wright, P. St. J. Russell, and A. Smithson, "Generation of permanent optically induced second-order nonlinearities in optical fibers by poling," Opt. Lett., vol. 13, pp. 592-594, 1988.

[1.9] R. Kashyap, "Phase-matched periodic electric-field-induced second-harmonic generation in optical fibers," J. Opt. Soc. Am. B, vol. 6, pp. 313-328, 1989.

[1.10] F. Ouellette, K. O. Hill, and D. C. Johnson, "Enhancement of second-harmonic generation in optical fibers by a hydrogen and heat treatment," Appl. Phys. Lett., vol. 54, pp. 1086-1088, 1989.

[1.11] A. Okada, K. Ishii, K. Mito, and K. Sasaki, "Phase-matched second-harmonic generation in novel corona poled glass waveguides," Appl. Phys. Lett., vol. 60, pp. 2853-2855, 1992.

[1.12] P. G. Kazansky, A. Kamal, and P. St. J. Russell, "High second-order nonlinearities induced in lead silicate glass by electron-beam irradiation," Opt. Lett., vol. 18, pp. 693-695, 1993.

[1.13] P. G. Kazansky, L. Dong and P. St. J. Russell, "Vacuum poling: an improved technique for effective poling of silica glass and germanosilicate optical fibres," Electron. Lett., vol. 30, pp. 1345-1347, 1994.

[1.14] T. Fujiwara, M. Takahashi, and A. Ikushima, "Large SHG in UV-poled silica glass," Digest of Conference of Bragg Gratings, Photosensitivity, and Poling in Glass Fibres and Waveguides: Applications and Fundamentals, BTuC1, pp. 290-292, Virginia, USA, 1997.

[1.15] D. M. Krol and J. R. Simpson, "Photoinduced second-harmonic generation in rare-earth-doped aluminosilicate optical fibers," Opt. Lett., vol. 16, pp. 1650-1652, 1991.

[1.16] H. Nasu, H. Okamoto, A. Mito, J. Matsuoka and K. Kamiya, "Influence of the OH content on second harmonic generation from electrically polarized SiO_2 glasses," Jpn. J. Appl. Phys., vol. 32, pp. L 406-L 407, 1993.

[1.17] K. Tanaka, K. Kashima, K. Hirao, N. Soga, A. Mito, and H. Nasu, "Second harmonic generation in poled tellurite glasses," Jpn. J. Appl. Phys., vol. 32, pp. L 843-L 845, 1993.

[1.18] K. Tanaka, K. Kashima, K. Hirao, N. Soga, S. Yamagata, A. Mito, and H. Nasu, "Highly efficient optical second harmonic generation in poled Ti-doped silica glasses," Jpn. J. Appl. Phys., vol. 34, pp. 175-176, 1995.

[1.19] S. K. Kurtz, J. Jerphagnon, and M. M. Choy, Landolt-Börnstein, Numerical Data and Functional Relationships in Science and Technology (Springer, New York, 1979), vol. 11, pp. 671.

[1.20] T. Hirama, H. Muto, O. Sugihara, and N. Okamoto, "Highly active second-order nonlinearity from Sol-Gel processed poled silica and germanosilicate thin film," Opt. Rev., vol. 3, pp. 17-18, 1996.

[1.21] F. C. Garcia, I. C. S. Carvalho, E. Hering, W. Margulis, and B. Lesche, "Inducing a large second-order nonlinearity in soft glasses by poling," Appl. Phys. Lett., vol. 72, pp. 3252-3254, 1998.

[1.22] L. Li and D. N. Payne, "Permanently-induced linear electro-optic effect in silica optical fibres," Digest of Conference of Integrated and guided wave optics, TuAA2-1, pp. 130-133, 1989.

[1.23] X. C. Long, R. A. Myers, and S. R. J. Brueck, "Measurement of the linear electro-optic coefficient in poled amorphous silica," Opt. Lett., vol. 19, pp. 1819-1821, 1994.

[1.24] X. C. Long, R. A. Myers, and S. R. J. Brueck, "Measurement of liner electro-optic effect in temperature/electrical-field poled optical fibres," Electron. Lett., vol. 30, pp. 2162-2163, 1994.

[1.25] P. G. Kazansky, P. St. J. Russell, L. Dong, and C. N. Pannell, "Pockels effect in thermally poled silica optical fibres," Electron. Lett., vol. 31, pp. 62-63, 1995.

[1.26] T. Fujiwara, D. Wong, and S. Fleming, "Large electrooptic modulation in a thermally poled germanosilicate fiber," IEEE Photon. Technol. Lett., vol. 7, pp. 1177-1179, 1995.

[1.27] X. C. Long and S. R. J. Brueck, "Large signal phase retardation with a poled electrooptic fiber," IEEE Photon. Technol. Lett., vol. 9, pp. 767-769, 1997.

[1.28] T. Fujiwara, D. Wong, Y. Zhao, S. Fleming, V. Grishina, and S. Poole, "UV-excited poling and electrically tunable Bragg gratings in a germanosilicate fiber," OFC'95 post-deadline paper PD6, San Diego, USA, 1995.

[1.29] A. C. Liu, M. J. F. Digonnet, and G. S. Kino, "Electro-optic phase modulation in a silica channel waveguide," Opt. Lett., vol. 19, pp. 466-468, 1994.

[1.30] M. Abe, T. Kitagawa, K, Hattori, A. Himeno, and Y. Ohmori, "Electro-optic switch constructed with a poled silica-based waveguide on a Si substrate," Electron. Lett., vol. 32, pp. 893-894, 1996.

[1.31] W. Margulis and F. Laurell, "Fabrication of waveguides in glasses by a poling procedure," Appl. Phys. Lett., vol. 71, pp. 2418-2420, 1997.

[1.32] P. G. Kazansky, V. Pruneri, and P. St. J. Russell, "Blue-light generation by quasi-phase-matched frequency doubling in thermally poled optical fibers," Opt. Lett., vol. 20, pp. 843-845, 1995.

[1.33] V. Pruneri and P. G. Kazansky, "Electric-field thermally poled optical fibers for quasi-phase-matched second-harmonic generation," IEEE Photon. Technol. Lett., vol. 9, pp. 185-187, 1997.

[1.34] V. Pruneri and P. G. Kazansky, "Frequency doubling of picosecond pulses in periodically poled D-shape silica fibre," Electron. Lett., vol. 33, pp. 318-319, 1997.

[1.35] P. G. Kazansky and V. Pruneri, "Electric-field poling of quasi-phase-matched optical fibers," J. Opt. Soc. Am. B, vol. 14, pp. 3170-3179, 1997.

[1.36] V. Pruneri, G. Bonfrate, P. G. Kazansky, C. Simonneau, P. Vidakovic, and J. A. Levenson, "Efficient frequency doubling of 1.5 μm femtosecond laser pulses in quasi-phase-matched optical fibers," Appl. Phys. Lett., vol. 72, pp. 1007-1009, 1998.

[1.37] H. Inglis, laboratory logbook, Optical Fibre Technology Centre, University of Sydney, Australia, 1996.

[1.38] D. Wong, S. Fleming, H.G. Inglis, and W. Xu, "Poled fibre devices", Invited paper, Conference Proceedings of LEOS'96, 9TH Annual Meeting, IEEE Lasers and Electro-Optics Society, Boston, WC1, P15, 1996.

Chapter 2 Technology Background

2.1 Introduction

The technology background of silica fibre poling is overviewed in this chapter. In Section 2.2, the structure, geometry and constituents of the twin-hole fibres used throughout this thesis are addressed in details. Section 2.3 provides detailed experimental setups to measure the phase change in the fibre devices due to an electro-optic effect. Equations for calculating an electro-optic coefficient are derived. In Section 2.4, the poling field in the fibre core is estimated both theoretically and experimentally.

2.2 Twin-hole Silica Fibres

Twin-hole silica fibre is very similar to a standard optical silica fibre. The difference is that the twin-hole fibre has two holes in the fibre cladding. The two holes are along either side of the fibre core, as shown in Fig. 2.1. There are many advantages in using twin-hole fibres for poling over other special fibres, such as D-shape fibre [2.1] and flat fibre [2.2]. Firstly, electrodes within the holes alongside the fibre core facilitate the application of high electrical field strengths. Secondly, such an arrangement of two electrodes and fibre core facilitates both heating and UV irradiation when an electrical field is applied to the two electrodes. Thirdly, the twin-hole fibres made it

possible to write Bragg fibre gratings and long period gratings into the core during poling. Finally, the provision of electrodes in proximity to the fibre core facilitates subsequent application of the poled fibre as an electro-optic device.

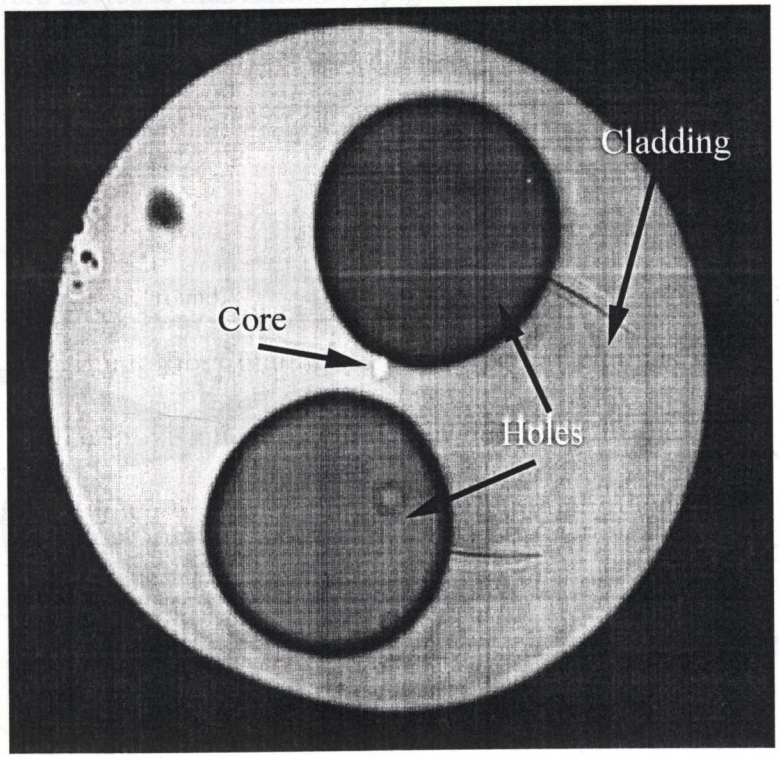

Fig. 2.1 A photo of end view of a twin-hole fibre

The twin-hole fibre device, as shown in Fig. 2.2, is made by means of the following steps. The silica preform is manufactured using the MCVD technique, and it is then ultrasonically milled with two holes on either side of the core along the preform. The twin-hole preform is drawn into the twin-hole fibre single moded at 633 nm, 1300 nm,

or 1550 nm, which depends on specific applications. Side slots are then polished along the sides of the twin-hole fibre to gain access to the holes. Fine metal wires are finally threaded into the holes in opposite directions through the two side polished slots to form electrodes, as illustrated by a photo in Fig. 2.3. Since the electrodes do not extend to the ends of the fibre, light can be coupled easily into and out of the fibre. The poled fibre device is thus inherently pigtailed.

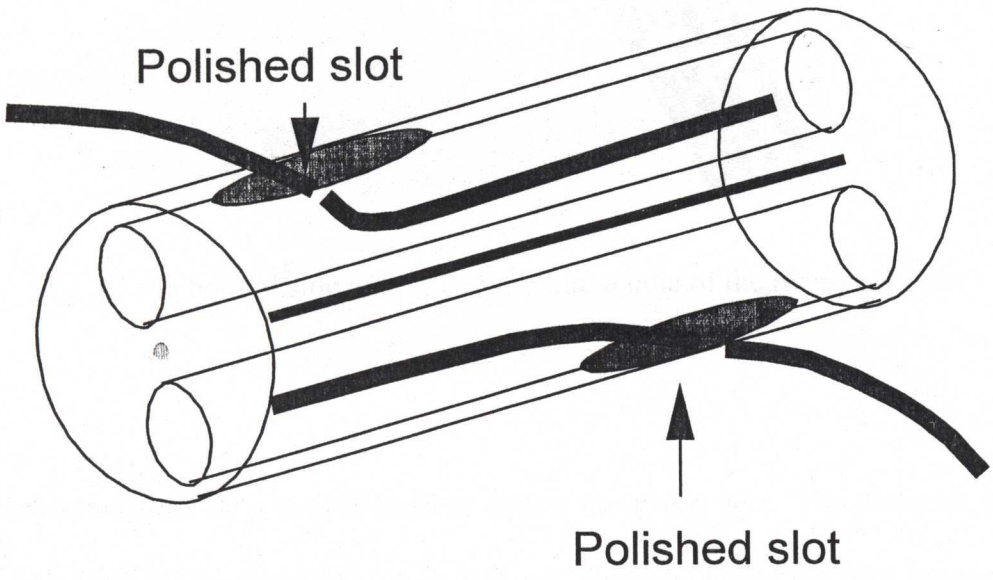

Fig. 2.2 A twin-hole fibre device (after Wong *et al.* [2.3])

W. Xu, "Thermally Poled Fibre Devices," Ph.D. Thesis, University of Sydney, Australia, March, 1999

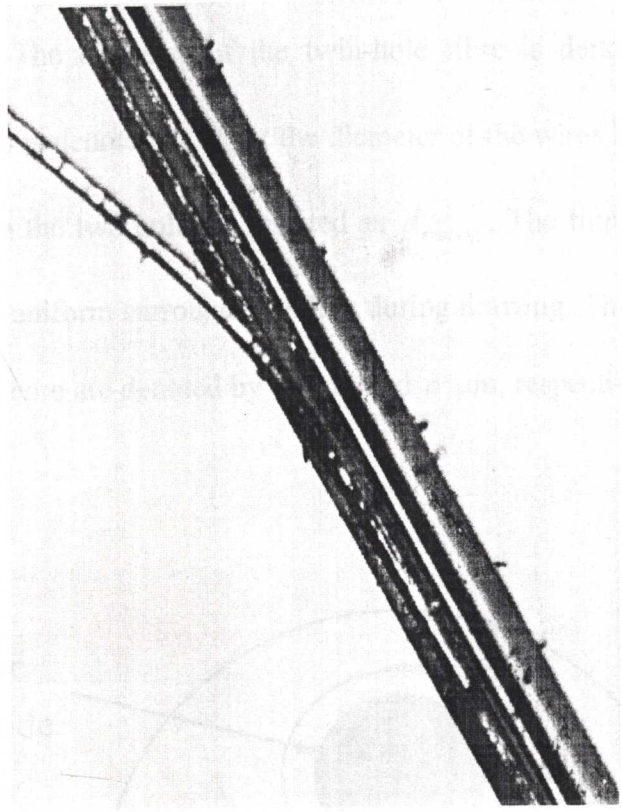

Fig. 2.3 A photo of side entry of a wire into a hole of the twin-hole fibre

Typical parameters of a twin-hole fibre device are given here. The diameter of the twin-hole fibre ranges from 200 μm to 300 μm. The diameter of the wire ranges from 25 μm to 50 μm. The wire may be gold, aluminum, or tungsten. The diameter of the holes ranges from 50 μm to 100 μm. The overlap between the two electrodes (the interaction length of the device) is from 30 mm to 70 mm. The two polished slots along the fibre have a separation from 50 mm to 100 mm.

W. Xu, "Thermally Poled Fibre Devices," Ph.D. Thesis, University of Sydney, Australia, March, 1999

An end view of a twin-hole fibre device with two electrodes threaded into the holes is shown in Fig. 2.4. The diameter of the twin-hole fibre is denoted as d_{fibre}; the diameter of the holes is denoted as d_{hole}; the diameter of the wires is denoted as d_{wire} the distance between the two holes is denoted as $d_{spacing}$. The fibre core is normally elliptical due to non-uniform surrounding stress during drawing. The major and minor axes of the elliptical core are denoted by m μm and n μm, respectively.

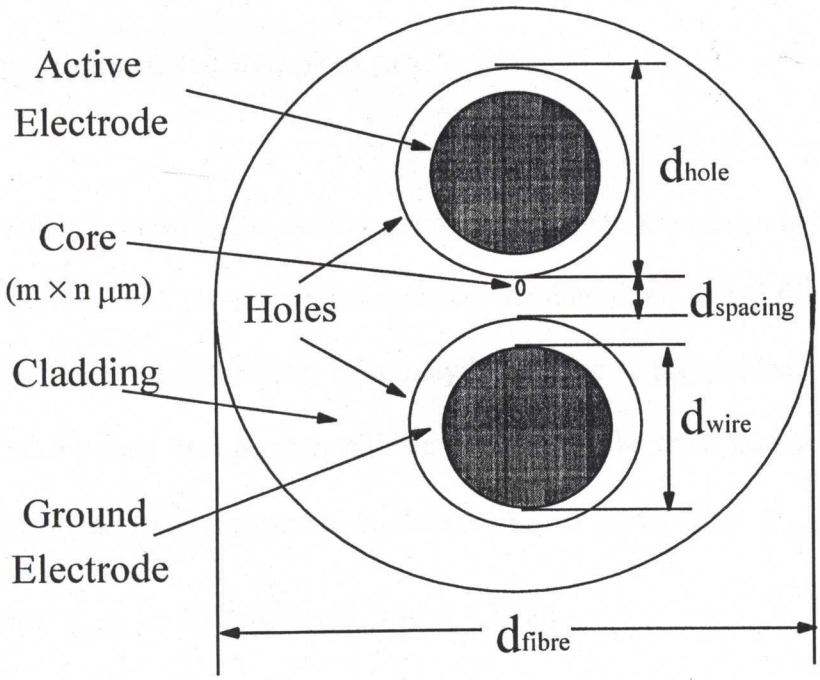

Fig. 2.4 Cross sectional geometry of a twin-hole fibre device

The core of the twin-hole fibre may be codoped with germanium, phosphorus, boron, aluminium, and other elements. There are mainly two types of twin-hole

germanosilicate fibres used in the experiments in this thesis: one is codoped with boron; the other codoped with aluminum.

The boron codoped germanosilicate fibre has 13.8 mole% boron and 14 mole% germanium in the core. The reason for using the boron-doped fibre is that boron-codoped germanosilicate fibre is known to exhibit higher photosensitivity than germanosilicate fibre [2.4]. Although its relation to poling is net yet clear, boron may offer some useful precursors for UV poling. The cross sectional geometry of the device made from the boron-doped fibre is given here: $d_{fibre} = 240$ μm, $d_{hole} = 90$ μm, $d_{spacing} = 16$ μm, $m = 6$ μm, $n = 3$ μm.

The aluminium co-doped germanosilicate has ~3.5 mole% aluminum and 14 mole% germanium in the core. The reason for studying the aluminum-doped fibre is that the aluminum-codoped germanosilicate fibre may have more stable residual electro-optic coefficient after poling than germanosilicate fibre [2.5]. The cross sectional geometry of the device made from the aluminum-doped fibre is given here: $d_{fibre} = 250$ μm, $d_{hole} = 80$ μm, $d_{spacing} = 16$ μm, $m = 6$ μm, $n = 3$ μm.

The core is deliberately positioned approximately 2μm from one hole and 9μm from the other hole for both the boron-codoped and the aluminum-codoped fibres.

W. Xu, "Thermally Poled Fibre Devices," Ph.D. Thesis, University of Sydney, Australia, March, 1999

Some numerical examples on the optical waveguiding properties of twin-hole fibres will be given in Appendix A.

2.3 Mach-Zehnder Interferometers

2.3.1 Mach-Zehnder Interferometer for *in situ* Poling

A free space MZI operating at 632.8 nm wavelength is used in the measurement of the time evolution of the induced electro-optic effect during and after poling, as shown in Fig. 2.5. Polarized light is used in the MZI. The twin-hole fibre is single-moded at the 633 nm wavelength and is placed at one arm with microscope objectives and micro-positioners. In the MZI setup, the induced electro-optic effect in each polarisation mode (TE and TM modes) can be measured. The TE mode is polarised in the direction of the two electrodes; while the TM mode is orthogonal to the direction of the electrodes, in the fibre cross section in Fig. 2.4.

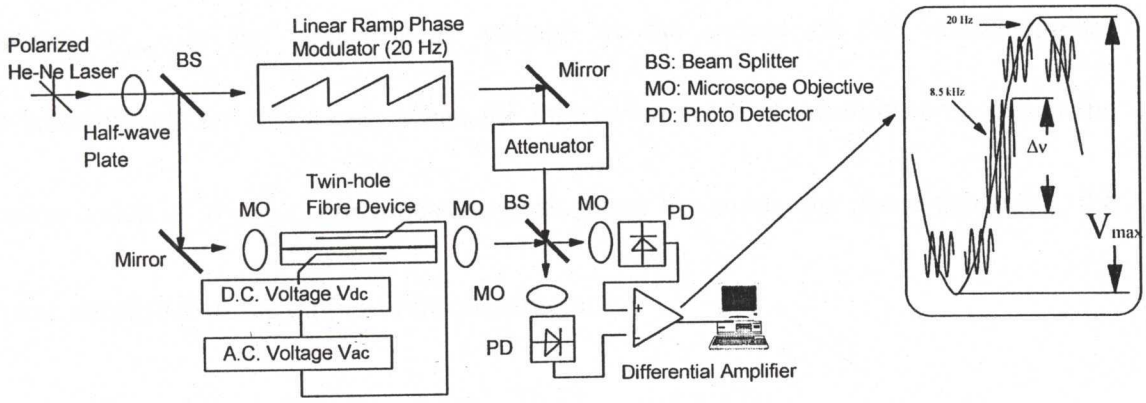

Fig. 2.5 MZI setup for *insitu* poling

A high voltage source provides the d.c. poling voltage, V_{dc}, from 2 kV to 5 kV. Another voltage supply provides sinusoidal a.c. testing voltage, V_{ac}, of an adjustable peak-to-peak voltage from 100 V to 900 V for measuring the electro-optic effect. The frequency of the test signal is set at 8.5 kHz, being higher than any mechanical resonance of the device induced by electro-static forces between the wires. A tuned circuit at this frequency is used to screen the d.c. poling high voltage supply from the a.c. testing voltage source. For *in situ* thermal poling experiments, the d.c. poling voltage supply is always superimposed with the a.c. testing voltage during a thermal poling cycle.

The output of the Mach-Zehnder interferometer may be expressed as a function of phase difference ϕ between the two arms using

$$V_o(\phi) = \frac{V_{\max}}{2}(1+\cos\phi), \tag{2.1}$$

where $V_{\max}$ is the peak-to-peak voltage at the output of the interferometer. Measurements are taken only when the interferometer is in quadrature i.e. when the mean value of $\phi = \frac{\pi}{2}$. For a peak-to-peak phase deviation $\Delta\phi$ about this point, the peak amplitude at the output of interferometer is

$$V_o\left(\phi - \frac{\Delta\phi}{2}\right) = \frac{V_{\max}}{2} + \frac{\Delta V}{2} = \frac{V_{\max}}{2}\left(1+\sin\left(\frac{\Delta\phi}{2}\right)\right). \tag{2. 2}$$

Rearranging Eq. 2.2, the phase deviation $\Delta\phi$ about this quadrature point can be calculated from the peak-to-peak amplitude of the measured signal ΔV using

$$\Delta\phi = 2\sin^{-1}\left(\frac{\Delta V}{V_{\max}}\right). \tag{2. 3}$$

A poled fibre has an electro-optic coefficient r. When V_{ac} is applied to the fibre, the change of the refractive index of the fibre core, δn_{co}, [2.6] is decided by

$$\delta n_{co} = \frac{1}{2} r n_{co}^3 \frac{V_{ac}}{d_{eff}}, \tag{2.4}$$

where d_{eff} is the effective distance between the two electrodes, n_{co} is the refractive index of the fibre core.

The phase deviation, $\Delta\phi$, caused by δn_{co}, is given by

$$\Delta\phi = \frac{2\pi L}{\lambda}\delta n_{co}, \tag{2. 5}$$

where λ = 632.8 nm is the free-space optical wavelength of the light, and L is the length of the overlap between the two electrodes. Combining Eqs. 2.4 and 2.5, the electro-optic coefficient, r, of the fibre device is then evaluated from the phase deviation in Eq. 2.3, using the equation

$$r = \frac{\lambda d_{eff}}{\pi V_{ac} L n_{co}^3}\Delta\phi. \tag{2. 6}$$

The second order nonlinearity $\chi^{(2)}$ can be approximately expressed in terms of the electro-optic coefficient, r, [2.7] by

$$\chi^{(2)} = \frac{n_{co}^4}{2} r . \tag{2. 7}$$

Substituting Eq. 2.6 into Eq. 2.7, the second order nonlinearity $\chi^{(2)}$ can further be calculated by

$$\chi^{(2)} = \frac{n_{co} \lambda d_{eff}}{2\pi V_{ac} L} \Delta\phi . \tag{2. 8}$$

2.3.2 Mach-Zehnder Interferometer for a Small Phase Change

Fig. 2.6 is another free-space MZI used to measure the LEO coefficient induced into the fibre device. The linear ramp phase modulator in the reference arm of the MZI provides the linear phase excursion at the MZI output appearing as a sinusoidal signal. A step d.c. test voltage source V_{test} is applied to the poled fibre device to probe its LEO coefficient by measuring the corresponding phase shift in the sinusoidal signal.

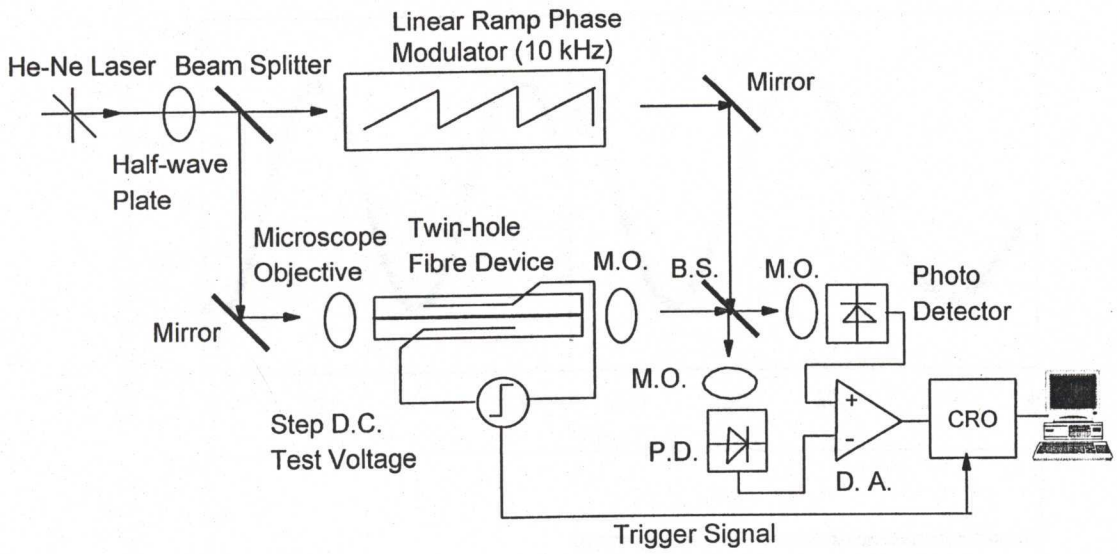

Fig. 2.6 MZI setup for measuring a small phase change. M.O. stands for Microscope Objective; B.S. stands for Beam Splitter; P.D. stands for Photo Detector; D. A. stands for Differential Amplifier.

Fig. 2.7 shows the output of the differential amplifier when V_{test} is applied to the poled fibre device. The corresponding phase change due to the LEO effect can be obtained from the phase difference of the sinusoidal waveforms before and after the test voltage is applied. The measurement of a phase change has a resolution better than ~0.1 radian. The electro-optic coefficient r and the second order nonlinearity $\chi^{(2)}$ of the fibre device can then be evaluated from the phase deviation using Eqs. 2.6 and 2.8, respectively.

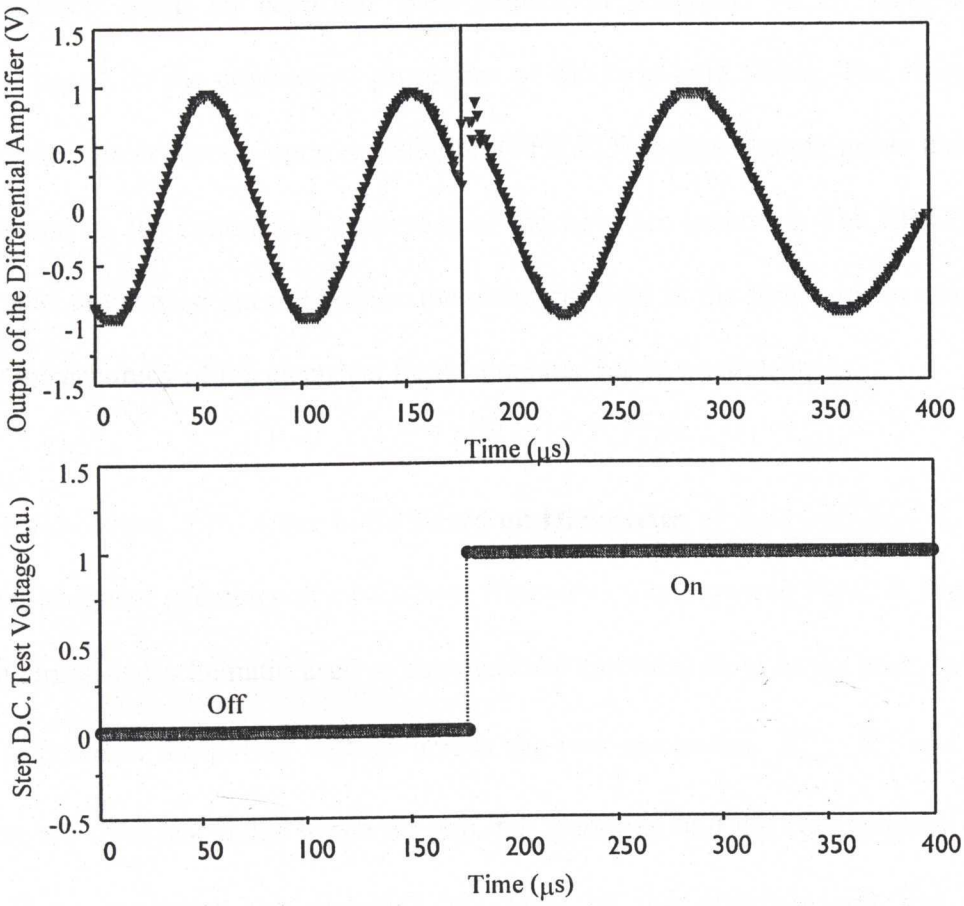

Fig. 2.7 Phase shift due to application of a step d.c. test voltage.

2.4 Estimation of the Electrical Field in the Core of the Twin-hole Fibres

Given the cross sectional geometry and NA of the fibre as well as the poling voltage, it is quite useful to know how large the poling field actually is in the fibre core. In this section, equations are derived to calculate the electrical field in the fibre core based on the dielectric properties of the twin-hole fibres. The electrical field in the fibre core is

also computed using an electrical field simulation program "ACE" from ABB Australia based on the conductive properties of the twin-hole fibres. The electrical field induced linear electro-optic modulation (EFILEOM) experiments prove that the results based on the conductive properties of the fibre are incorrect. The EFILEOM experiments are carried out to measure the electrical field in the fibre core in order to validate the accuracy of the electrical field calculated based on dielectrics.

2.4.1 Calculation of the Core Field Based on Dielectrics

The cross sectional geometry of a twin-hole fibre device is shown in Fig. 2.4. Fig. 2.8 shows a simplified schematic used to calculate the electrical field in the core. In Fig. 2.8, V represents the poling voltage across the two electrodes. $\vec{E}_{air}$, $\vec{E}_{cl}$ and $\vec{E}_{co}$ represent the electrical fields in the air gap, the cladding, and the core, respectively. ε_{cl} and ε_{co} represent the dielectric constants of the cladding and the core, respectively. ε_o, $\varepsilon_{cl}\varepsilon_o$ and $\varepsilon_{co}\varepsilon_o$ represent the electric permittivity of air, the cladding, and the core, respectively. σ_{air}, σ_{cl} and σ_{co} represent the electrical conductivity of air, the cladding, and the core, respectively. $d_{spacing}$ represents the distance between two holes. d_{air} represents the air gap between the electrode and the cladding. The major and minor axes of the elliptical core are m μm and n μm, respectively.

Because the elliptical core is very small compared with the entire fibre and the refractive index difference between the cladding and the core is much less than unity,

W. Xu, "Thermally Poled Fibre Devices," Ph.D. Thesis, University of Sydney, Australia, March, 1999

the core is considered as a small perturbation to the cladding. The electrical field in the cladding $\vec{E}_{cl}$ is firstly calculated using Gauss's law, and the electrical field in the core $\vec{E}_{co}$ is then derived based on the perturbation assumption.

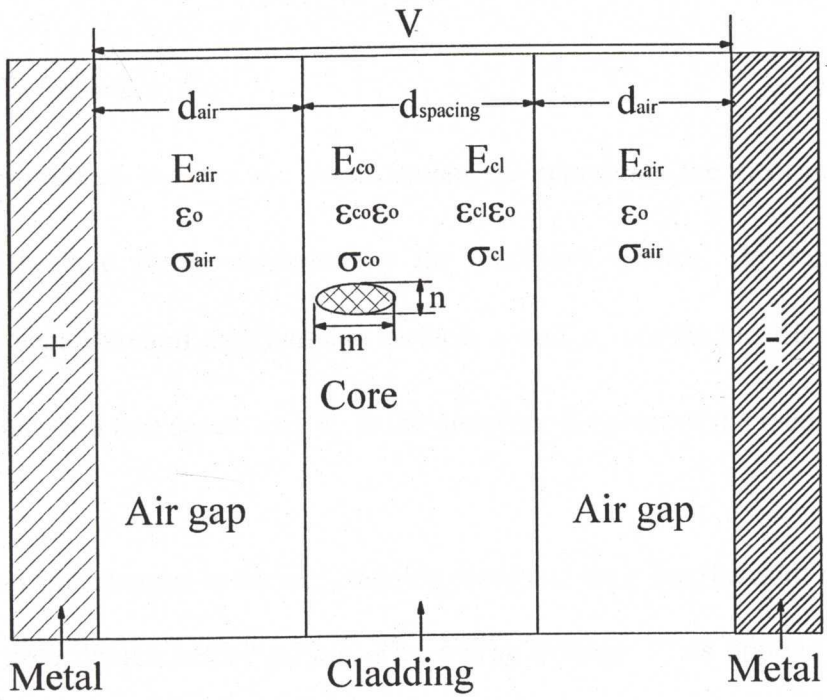

Fig. 2.8 Simplified cross sectional geometry of a twin-hole fibre device.

ε_{co} and ε_{cl} are related to the refractive indices of the core and the cladding by the equations

$$\varepsilon_{co} = n_{co}^2 \tag{2.9}$$

and

$$\varepsilon_{cl} = n_{cl}^2, \tag{2. 10}$$

where n_{co} and n_{cl} are the refractive indices of the core and the cladding, respectively.

The Gauss's law [2.8] is given by

$$\oint \vec{D} \bullet d\vec{A} = Q \tag{2. 11}$$

and

$$\vec{D} = \varepsilon \vec{E} = \varepsilon_r \varepsilon_o \vec{E}, \tag{2. 12}$$

where $\vec{D}$ represents the electric displacement, $\vec{E}$ represents the electrical field, Q represents the free charge enclosed by the Gaussian surface, $d\vec{A}$ represents the differential vector area of the Gaussian surface, ε and ε_o are the electric permittivity of the medium and free space, and ε_r is the dielectric constant of the medium.

There are no free charges in the air, cladding, core and their interfaces of an as-drawn twin-hole fibre device before poling. The poling voltage V is applied to the two electrodes of the fibre. Applying Gauss's law to the twin-hole fibre, the electric displacements in the air gap and the cladding are related by the equation

$$\vec{D}_{air} = \vec{D}_{cl}, \tag{2. 13}$$

where $\vec{D}_{air}$ and $\vec{D}_{cl}$ represent the electric displacements in the air gap and the cladding, respectively. Substituting Eq. 2.12 into Eq. 2.13, the electrical fields in the air gap and the cladding are related by the equation

$$\varepsilon_o \vec{E}_{air} = \varepsilon_{cl} \varepsilon_o \vec{E}_{cl}, \tag{2. 14}$$

where $\vec{E}_{air}$ and $\vec{E}_{cl}$ represent the electrical fields in the air gap and the cladding respectively. Substituting Eq. 2.10 into Eq. 2.14 gives

$$\vec{E}_{air} = n_{cl}^2 \vec{E}_{cl}. \tag{2. 15}$$

The relation of the potential difference V_{ab} of a path from point a to point b and the electrical field $\vec{E}$ along the path are expressed [2.9] by the equation

$$V_{ab} = \int_a^b \vec{E} \bullet d\vec{l}. \tag{2. 16}$$

Applying Eq. 2.16 to the twin-hole fibre with the poling voltage V on, the relation among V, E_{air} and E_{cl} are given by

$$2d_{air}E_{air} + E_{cl}d_{spacing} = V. \tag{2. 17}$$

Combining Eq. 2.15 and Eq. 2.17, the electrical field in the cladding, E_{cl}, can be calculated by the equation

$$E_{cl} = \frac{V}{2n_{cl}^2 d_{air} + d_{spacing}}. \tag{2. 18}$$

The core is embedded in the cladding and the electrical field in the core is given [2.10] by the equation

$$E_{co} = E_{cl} \frac{m+n}{m + \frac{n_{co}^2}{n_{cl}^2} n}. \tag{2. 19}$$

Because of $n_{co} \approx n_{cl}$, Eq. 2.19 reduces to $E_{co} \approx E_{cl}$. The electrical field in the core approximately equals that in the cladding. From Eq. 2.18, E_{co} is given by the equation

$$E_{co} = \frac{V}{2n_{co}^2 d_{air} + d_{spacing}}. \quad (2.20)$$

Alternatively, E_{co} can be expressed as

$$E_{co} = \frac{V}{d_{eff}}, \quad (2.21)$$

where the effective distance between the two electrodes, d_{eff}, can be obtained from

$$d_{eff} = 2n_{co}^2 d_{air} + d_{spacing}. \quad (2.22)$$

Using Eq. 2.20, the electrical field in the core of two actual devices will be calculated in order to compare the results with the values experimentally measured.

The air gap d_{air} along the fibre device is uncertain, as each electrode is randomly located in the hole. Supposed that each electrode is statistically situated in the middle of the hole in the twin-hole fibre, as shown in Fig. 2.9. d_{air} is then calculated by

$$d_{air} = \frac{1}{2}(d_{hole} - d_{wire}), \quad (2.23)$$

where d_{wire} is the diameter of the electrode.

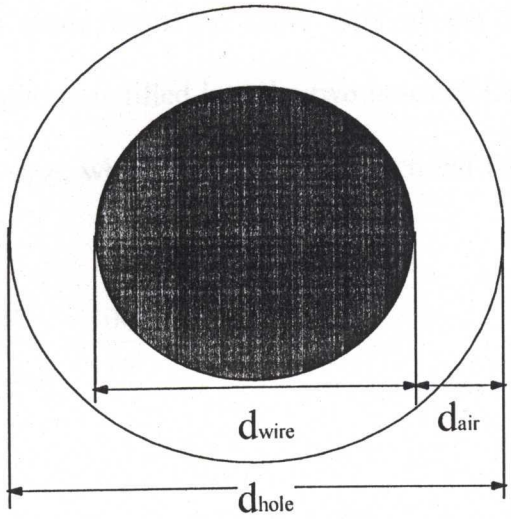

Fig. 2.9 An electrode in the twin-hole fibre hole.

A twin-hole fibre device is denoted as D1. Its cross sectional geometry is depicted in Fig. 2.4. D1 has the following parameters: the refractive indices of the cladding and the core are 1.459 and 1.46; the hole diameter d_{hole} is 80 μm; the electrode diameter d_{wire} is 50 μm; the distance $d_{spacing}$ between the two holes is 16 μm. Using Eq. 2.23, the air gap of the device D1 is calculated as $d_{air} = 15$ μm.

The poling voltage V is 1 kV and is applied to D1 and the electrical field in the core of D1 is calculated as

$$E_{co} = \frac{1000}{2 \times 1.46^2 \times 15 + 16} = 12.5 \text{ V/μm.} \qquad (2.24)$$

Another device D2 is made from the same type of the fibre as D1. However, conductive chemical solution is filled into the two holes of D2 and thus there are not air gaps in D2. In this case, when $V = 1$ kV, the electrical field in the core of D2 is calculated as

$$E_{co} = \frac{V}{d_{spacing}} = \frac{1000}{16} = 62.5 \text{ V/μm.} \quad (2.25)$$

2.4.2 Computation of the Field in Twin-hole Fibres Based on Conductivity

The twin-hole fibre devices used for ACE computational simulation have the following parameters: $d_{wire} = 50$ μm, $d_{hole} = 90$ μm, $d_{spacing} = 20$ μm, and the core is a 6×3 μm ellipse. Table 2.1 shows the data of the electrical conductivity of the air, the cladding and the core used in the computational simulation [2.11].

Table 2.1 Electrical conductivity of the air, the cladding and the core

Materials	Electrical Conductivity at 25 °C ($\Omega^{-1}m^{-1}$)	Electrical Conductivity at 250 °C ($\Omega^{-1}m^{-1}$)
Air	Not Available	1.0×10^{-12}
Silica (Cladding)	2.0×10^{-21}	4.0×10^{-10}
Ge-doped silica (Core)	1.0×10^{-18}	1.0×10^{-8}

A d.c. voltage of 4 kV is applied to the twin-hole fibre at 250 °C and the electrical field distributions in the fibre are shown for three electrode configurations in Fig.

2.10. For the three electrode configurations, there is an electrical field of about 50 V/μm in the core only when the two electrodes touch inner edge of the two holes. There is almost no electrical field in the core when there are air gaps for the other two configurations.

The results computed by the ACE program based on the conductive properties of the twin-hole fibres are inconsistent with both the calculated results based on the dielectric properties of the fibres and the EFILEOM experiments [2.12]. According to the program, there is almost no electrical field in the core when there are air gaps in the twin-hole fibre devices. However, when the d.c. voltage of 4 kV is applied to a fibre device with air gaps between the electrodes and the cladding, there is a strong electrical field in the fibre core, which can induce the electro-optic modulation as shown in Ref. 2.12.

Hence, the computation of the electrical field in the fibre core based on conductivity is incorrect. The calculation of the electrical field in the fibre core should be based on the dielectric properties of the twin-hole fibre. In the next subsection, the accuracy of the calculated results based on dielectrics will be validated using the EFILEOM experiments.

W. Xu, "Thermally Poled Fibre Devices," Ph.D. Thesis, University of Sydney, Australia, March, 1999

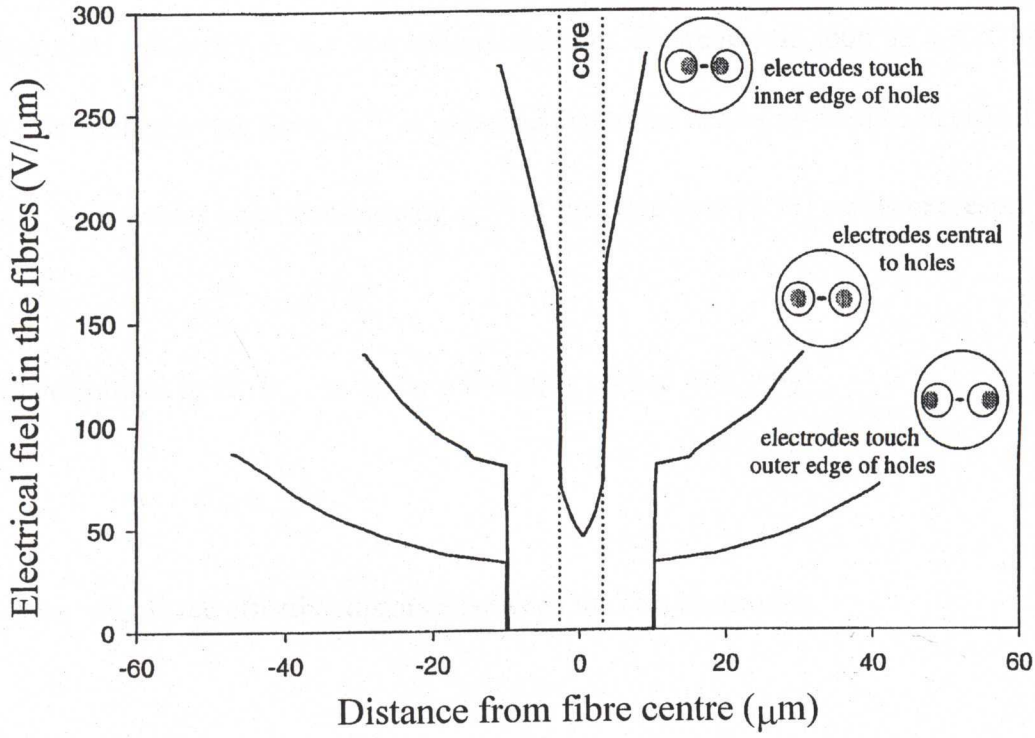

Fig. 2.10 Electrical field distribution in the twin-hole fibres

2.4.3 Validity of Electrical Field Calculations Using EFILEOM

The measurement of the electrical field in the core of twin-hole fibres is based on the MZI experimental setup for *in situ* poling measurements, as described in Section 2.3. If the third order nonlinearity $\chi^{(3)}$ of the fibre core is already known, the d.c. electrical field, E'_{co}, in the fibre core can be obtained from the electro-optic modulation measurement of an electrical field induced $\chi^{(2)}$.

There is no intrinsic second order nonlinearity $\chi^{(2)}$ for a silica fibre due to the inversion symmetry of the amorphous medium. However, as soon as a d.c. voltage V_{dc} is applied to the fibre, $\chi^{(2)}$ is obtained due to the action of the d.c. electrical field, E'_{co}, on the third order nonlinearity $\chi^{(3)}$ of the fibre core [2.13] and is expressed as

$$\chi^{(2)} = 3\chi^{(3)} E'_{co}. \tag{2. 26}$$

The electrical field, E'_{co}, in the core is simply related to V_{dc} by

$$E'_{co} = \frac{V_{dc}}{d'_{eff}}, \tag{2. 27}$$

where d'_{eff} is the effective distance between the two electrodes.

If a small amount of a.c. testing voltage V_{ac} is applied to the fibre device together with V_{dc}, an electro-optic modulation can then be obtained in the MZI setup. Based on Eqs. 2.8, 2.26 and 2.27, d'_{eff} can be calculated from

$$d'_{eff} = \sqrt{\frac{6\pi L V_{ac} V_{dc} \chi^{(3)}}{n_{co} \lambda \Delta\phi}}. \tag{2. 28}$$

Finally, the electrical field E'_{co} in the core can be obtained from d'_{eff} using Eq. 2.27.

For the device D1 in Subsection 2.4.1 with the overlap length $L = 0.07$ m, the phase change $\Delta\phi$ is measured as 0.0449 radian when the d.c. voltage V_{dc} of 1 kV and the a.c. testing voltage V_{ac} of 250 V are applied onto D1. Assuming $\chi^{(3)}$ of the core is

known as 1.8×10^{-22} $(m/V)^2$ [2.14] and using Eq. 2.28, the effective distance between the two electrodes is calculated as

$$d'_{eff} = \sqrt{\frac{6\pi \times 250 \times 0.07 \times 1000 \times 1.8 \times 10^{-22}}{1.46 \times 6.328 \times 10^{-7} \times 0.0449}} = 3.78 \times 10^{-5}\, m = 37.8 \mu m . \quad (2.29)$$

So the d.c. electrical field E'_{co} in the core due to $V_{dc} = 1$ kV is

$$E'_{co} = \frac{1000}{37.8} = 26.5 \text{ V/μm.} \quad (2.30)$$

The comparison between the theoretical value $E_{co} = 12.5$ V/μm in Eq. 2.24 and the measured value $E'_{co} = 26.5$ V/μm shows that there is ~53% error between them. The reason is that the distance between the two wires is randomly located in the holes along the device. The air gap between the wire and the cladding is not the assumed statistical distance of $\frac{1}{2} \times (d_{hole} - d_{wire})$.

For the device D2 with the overlap length $L = 0.1$ m, the phase change $\Delta\phi$ is measured as 0.3712 radian when the d.c. voltage V_{ac} of 1 kV and the a.c. testing voltage V_{ac} of 250 V are applied onto D2. Using Eq. 2.28, the effective distance between the two electrodes is calculated as

$$d'_{eff} = \sqrt{\frac{6\pi \times 250 \times 0.1 \times 1000 \times 1.8 \times 10^{-22}}{1.46 \times 6.328 \times 10^{-7} \times 0.3712}} = 1.57 \times 10^{-5}\, m = 15.7 \mu m . \quad (2.31)$$

So the d.c. electrical field, E'_{co}, in the core due to $V_{dc} = 1$ kV is

$$E'_{co} = \frac{1000}{15.7} = 63.7 \text{ V/μm.} \quad (2.32)$$

The comparison between the theoretical value $E_{co} = 62.5$ V/μm in Eq. 2.25 and the measured value $E'_{co} = 63.7$ V/μm shows that there is only 2% error between them. The reason for this agreement is that there are not air gaps in the two holes and the distance between the two wires is exactly the spacing between the two holes.

Therefore, the derived equations for calculating the electrical field in the fibre core are accurate for the fibre device without the air gaps between the wires and the cladding. However, if there are air gaps in the device, and the wires are randomly placed in the two holes, there is a large error between the calculated electrical field and the measured electrical field.

2.5 Conclusion

The twin-hole fibre devices and the MZI experimental setups used in this thesis have been described in detail in Section 2.2 and Section 2.3, respectively.

Section 2.4 is focused on estimation of the electrical field in the core of the twin-hole fibres. Calculations of the electrical fields should be based on the dielectric properties of the twin-hole fibre instead of the conductivity properties of the fibre. The random distribution of the wires in the holes results into a large error between the calculated electrical field and the measured electrical field. However, if the distance between the two wires is exactly the same as the hole spacing, the calculated results are consistent with the measured results.

2.6 References

[2.1] P. G. Kazansky, L. Dong and P. St. .J. Russell, "Vacuum poling: an improved technique for effective thermal poling of silica glass and germanosilicate optical fibres", Electronics Letters, Vol.30, No.16, pp.1345-1347, 1994.

[2.2] X. C. Long, R. A. Myers and S. R. J. Brueck, "A poled electrooptic fiber", IEEE Photonics Technology Letters, Vol.8, No.2, pp.227-229, 1996.

[2.3] D. Wong, S. Fleming, H.G. Inglis, and W. Xu, "Poled fibre devices", Invited paper, Conference Proceedings of LEOS'96, 9TH Annual Meeting, IEEE Lasers and Electro-Optics Society, Boston, WC1, P15, 1996.

[2.4] D. L. Williams, B. J. Ainslie, J. R. Armitage, R. Kashyap, and R. Campbell, "Enhanced UV photosensitivity in boron codoped germanosilicate fibres," Electron. Lett., vol. 29, pp. 45-47, 1993.

[2.5] D. Wong, W. Xu, R. Hall, and M. Janos, "Thermal poling of aluminium co-doped germano- silicate fibres," Proceedings of the 23rd Australian Conference of Optical Fibre Technology, pp.197-200, Melbourne, Australia, July 1998.

[2.6] B. E. A. Saleh and M. C. Teich, Fundamentals of Photonics, Chap. 18, pp. 698-712, John Wiley & Sons, Inc., 1991.

[2.7] B. E. A. Saleh and M. C. Teich, Fundamentals of Photonics, Chap. 19, pp. 740-746, John Wiley & Sons, Inc., 1991.

[2.8] F. W. Sears, M. W. Zemansky, and H. D. Young, University Physics (7th Edition), Addison-Wesley Publishing Company, 1987, Chapter 25, pp. 546-574.

[2.9] F. W. Sears, M. W. Zemansky, and H. D. Young, University Physics (7th Edition), Addison-Wesley Publishing Company, 1987, Chapter 26, pp. 575-603.

[2.10] M. Fogiel, THE ELECTROMAGNETICS PROBLEM SOLVER, Research and Education Association, New York, 1983.

[2.11] R. Bailey, Preform and Fibre Manufacture Data Sheet, Optical Fibre Technology Centre, University of Sydney, Australia, 1997.

[2.12] W. Xu, D. Wong, S. Fleming, M. Janos, and K. M. Lo, "Direct measurement of frozen-in field in thermally poled fibres," Proceedings of the 23rd Australian Conference of Optical Fibre Technology (ACOFT'98), pp. 201-204, Melbourne, Australia, July 1998.

[2.13] P.G. Kazansky and P. St. J. Russell, "Thermally poled glass: frozen-in electric field or oriented dipoles?" Optics Communications, vol. 110, pp. 611-614, 1994.

[2.14] R. Adair, L. L. Chase, and S. A. Payne, "Nonlinear refractive-index measurements of glasses using three-wave frequency mixing," J. Opt. Soc. Am. B, vol. 4, pp. 875-881, 1987.

Chapter 3 Optimisation of Poling Conditions for Thermal Poling

3.1 Introduction

In order to maximize the induced LEO effect for practical device applications and understand the mechanism of thermal poling, it is necessary to investigate the influence of poling conditions on the induced LEO coefficient. A few research groups have reported the dependence of the induced linear electro-optic effect in silica fibres on the poling conditions [3.1-3.4]. Myers *et al.* found that there is a poling temperature window with the range from ~200 °C to ~350 °C for bulk silica and from ~50 °C to ~250 °C for thin silica film [3.2]. Takebe *et al.* studied the effects of poling time and applied voltage on second-harmonic generation in thermally poled fused silica glass [3.3]. They found that the SHG signal was proportional to the square of the poling voltage, and the speed of the poling process increased with the poling voltage. The effect of poling time and poling voltage on the induced LEO coefficient have also been reported by Long *et al.* on germanosilicate fibre [3.4]. Arentoft *et al.* reported that the optimum poling temperature for UV-written silica-based waveguides ranges from ~400 °C to ~450 °C [3.5], which is ~150 °C higher than reported for silica fibers [3.1].

This chapter demonstrates the dependence of the induced LEO effect in boron-codoped germanosilicate fibre on poling voltage, poling temperature and poling time using the Mach-Zehnder interferometer for measuring a small phase change, which is described in Section 2.3 of Chapter 2. The twin-hole fibre devices used for this chapter are made from the boron-codoped germanosilicate fibre, which were introduced in detail about glass constituents and fibre geometry in Section 2.2 of Chapter 2. A fibre device made from as-drawn fibre was used for each thermal poling experiment under specific poling conditions. The optimum thermal poling conditions for the boron-codoped germanosilicate fibre are obtained from such a systematic study.

3.2 Dependence of Electro-optic Effect on Poling Voltage

The measurements of dependence of the induced LEO coefficient on the poling voltage reveal that the value of the LEO coefficient has a ~2.7 power law dependence on the poling voltage, i.e. $r \propto V_{poling}^{2.7}$, as shown in Fig. 3.1. Based on the relationship between r and $\chi^{(2)}$ for silica ($\chi^{(2)} \approx 2r$), the induced SON in the poled fibre device also has a ~2.7 power law dependence on the poling voltage, $\chi^{(2)} \propto V_{poling}^{2.7}$. Considering the model of the frozen-in electrical field formation in the depletion region near to the anode [3.6], the higher the poling voltage that is applied, the stronger the frozen-in electrical field that is formed, and so the larger the LEO coefficient that is induced. However, the measured dependence of the LEO coefficient on the poling voltage disagrees with two previous measurements [3.3, 3.7]. H. Takebe

et al. studied the dependence of the induced SON $\chi^{(2)}$ on the poling voltage and found that the SHG signal $P_{2\omega} \propto V_{poling}^2$ [3.3]. Because of $P_{2\omega} \propto (\chi^{(2)})^2$ [3.3], they obtained that $\chi^{(2)} \propto V_{poling}$. Myers *et al.* found out that $P_{2\omega}$ on the thermally poled bulk silica increased as a ~3.5 power law with the poling voltage V_{poling}, i.e. $P_{2\omega} \propto V_{poling}^{3.5}$ [3.7]. Hence their result reveals that the induced SON $\chi^{(2)} \propto V_{poling}^{1.7}$. Therefore, further experiments and better understanding of thermal poling mechanism could clarify the disparity among these results about the power law relation between the induced $\chi^{(2)}$ and the poling voltage V_{poling}.

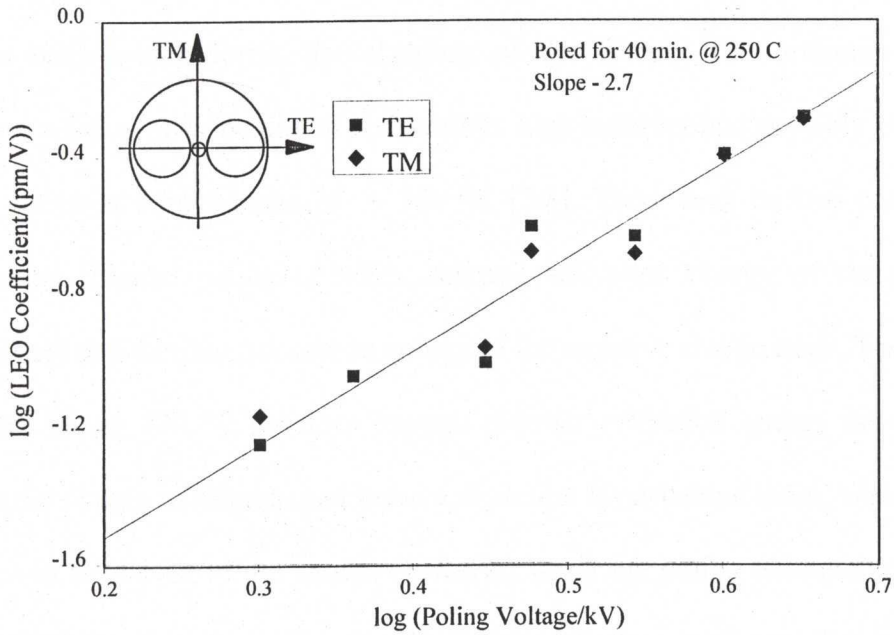

Fig. 3.1 Dependence of the LEO coefficient on poling voltage. ■ and ◆ refer to the experimental data; solid line stands for the experimental data fit.

3.3 Dependence of Electro-optic Effect on Temperature

Fig. 3.2 shows that there is an optimum poling temperature window for boron-codoped germanosilicate fibre. For a given poling duration (40 min.), very little LEO effect was induced below 220 °C. Increasing the poling temperature above 220 °C increases the LEO effect until a temperature around 300 °C is reached, after which the LEO effect is poorly induced into the fibre. For the present fibre, dielectric breakdown took place at poling temperatures above 350 °C with a poling voltage of 3.0 kV, and no thermal poling at temperatures above 350 °C was successful. Therefore, the optimum poling temperature for boron-codoped germanosilicate fibre is from ~ 250 °C to ~ 300 °C. Small traces of Na^+ (~ 0.18 ppm) have been found in the MCVD silica deposition tube, which forms the cladding of the fibre. The optimum poling temperature window may be due to Na^+ with its high mobility and possibly H^+ being the most active at temperatures of ~ 300 °C [3.8]. There may be two competing factors during thermal poling of silica: thermal activation energy of the positive charge carriers and thermal fluctuation energy of the negative charge traps. The poling temperature above 220 °C provides enough thermal activation energy so that the charge carriers begin to migrate and leave a depletion layer behind them, which leads to a frozen-in field near to the anode. However, when the poling temperature is too high (>300 °C), it offers thermal energy higher than the thermal fluctuation energy of the charge traps, which constitute the depletion region. So the charge traps cannot keep their extra electrons, and the frozen-in field becomes weaker until it becomes zero. Dielectric breakdown taking place at temperatures above 350 °C may be facilitated by these free charges.

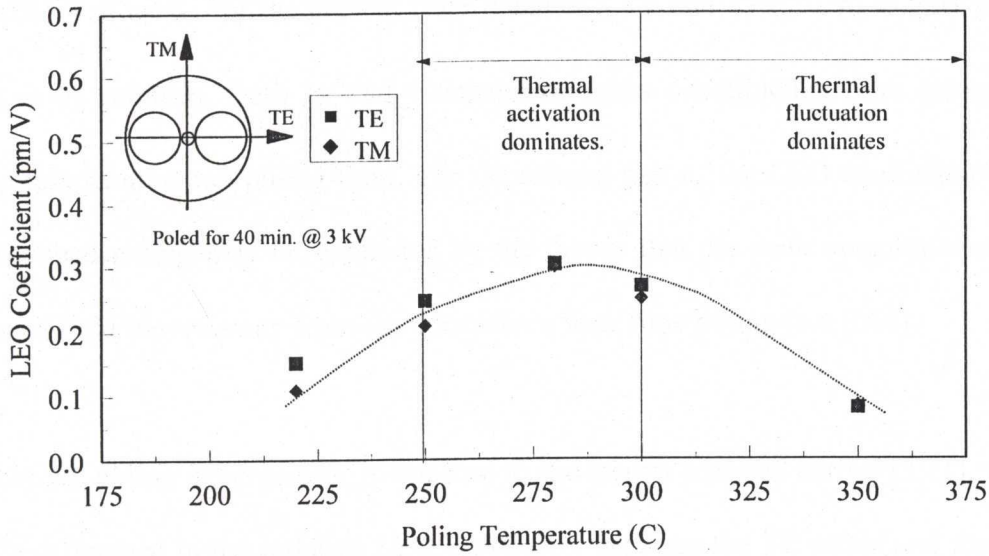

Fig. 3.2 Dependence of the LEO coefficient on poling temperature. ■ and ◆ refer to the experimental data; dotted line stands for the trend according to the experimental data.

3.4 Dependence of Electro-optic Effect on Poling Time

The dependence of the LEO coefficient on the poling time is shown in Fig. 3.3. The LEO coefficient increases with the poling time initially before saturating around 80-120 minutes, and then it decreases after ~120 minutes, which is consistent with the *in situ* thermal poling measurements [3.9]. The increasing part of the LEO coefficients is fitted by a single exponential equation

$$r(t) = r_0\left(1 - e^{-t/\tau}\right), \tag{3.1}$$

W. Xu, "Thermally Poled Fibre Devices," Ph.D. Thesis, University of Sydney, Australia, March, 1999

where r_0 is the saturated LEO coefficient and τ is the time constant of the single exponential process. For the present fibre poled at 3 kV and 250 °C, r_0 is 0.51 pm/V and τ is 68 minutes. Both r_0 and τ depend on glass constituents, fibre geometry, poling temperature and poling field. The decreasing part of the LEO coefficients due to prolonged poling may be explained by the theory that the peak magnitude of the frozen-in field moves away from the core after a long time poling [3.4, 3.10].

In all of the poling experiments, in contrast to the results reported earlier [3.11], there is little difference in the induced LEO coefficient between the TE mode and the TM mode. This may be because the present twin-hole fibre has a rounder core and a lower NA than that used before. Hence it has a lesser contribution from both the stress and geometric birefringence.

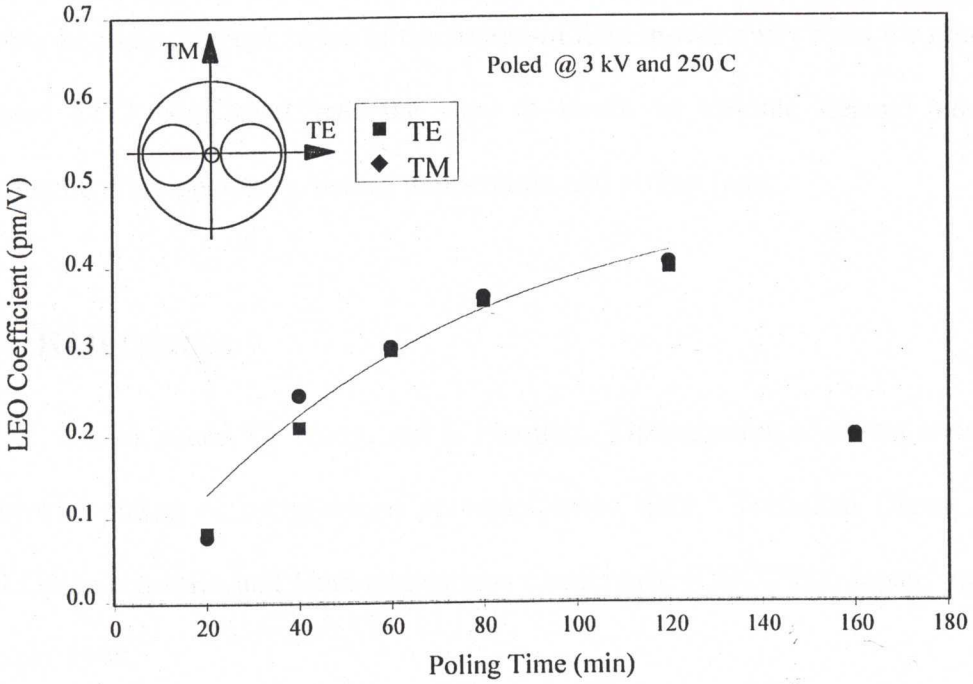

Fig. 3.3 Dependence of the LEO coefficient on poling time. ■ and ◆ refer to the experimental data; solid line stands for the single exponential fit.

3.5 Conclusion

It was demonstrated that the LEO coefficient induced into boron-codoped germano-silicate fibre by thermal poling increases as a ~2.7 power law with the poling voltage. The optimum poling temperature window was found to be between ~250 °C and ~300 °C for the fibre studied, which possibly results from competition between thermal activation energy of positive charge carriers and thermal fluctuation energy of negative charge traps. The induced LEO coefficient initially increases as a single

exponential process with the poling time until saturation, and then it decreases probably because the peak value of the frozen-in field moves away from the core. The saturated LEO coefficient and the time it needs to saturate depend on glass constituents, fibre geometry, poling temperature and poling field.

3.6 References

[3.1] W. Xu, M. Janos, D. Wong, and S. Fleming, "Optimisation of poling conditions for thermal poling of boron-doped germanosilicate fibre," Technical Digest of the Third Optoelectronics and Communications Conference (OECC'98), Japan, pp. 516-517, July 1998.

[3.2] R. A. Myers, S. R. J. Brueck, and R. P. Tumminelli, "Stable Second-Order Nonlinearity in SiO_2-Based Waveguides on Si Using Temperature/Electric-Field Poling," Proceedings of SPIE, vol. 2289, pp. 158-166, 1994.

[3.3] H. Takebe, P. G. Kazansky, P. St. J. Russell and K. Morinaga, "Effect of poling conditions on second-harmonic generation in fused silica," Opt. Lett., vol. 21, pp. 468-470, 1996.

[3.4] X. C. Long, R.A. Myers and S. R. J. Brueck, "A poled electrooptic fiber", IEEE Photon. Tech. Lett., vol.8, pp. 227-229, 1996.

[3.5] J. Arentoft, M. Kristensen, J. Hübner, W. Xu, and M. Bazylenko, "Poling of UV-written wave-guides," Technical Digest of OFC/IOOC'99 (Wednesday, February 24), WM19, pp. 250-252, San Diego, USA, 1999.

[3.6] W. Xu, D. Wong, S. Fleming, M. Janos, and K. M. Lo, "Direct measurement of frozen-in field in thermally poled fibres," Proceedings of the 23rd Australian

Conference of Optical Fibre Technology (ACOFT'98), pp. 201-204, Melbourne, Australia, July 1998.

[3.7] R. A. Myers, N. Mukherjee, and S. R. J. Brueck, "Large second-order nonlinearity in poled fused silica," Opt. Lett., vol. 16, pp. 1732-1734, 1991.

[3.8] N. Mukherjee, R. A. Myers, and S. R. J. Brueck, "Dynamics of second-harmonic generation in fused silica," J. Opt. Soc. Am. B, vol. 11, pp. 665-669, 1994.

[3.9] D. Wong, W. Xu, M. Janos, J. Chow, R. Hall, and S. Fleming, "Time Evolution of Electro-optic Effect in Fibre During Thermal Poling," Jpn. J. Appl. Phys., vol. 37, Suppl. 37-1, pp. 68-70, 1998.

[3.10] W. Xu, D. Wong, and S. Fleming, "Evolution of the linear electro-optic coefficient and the third order nonlinearity in prolonged negative thermal poling," submitted to Electronics Letters.

[3.11] T. Fujiwara, D. Wong, and S. Fleming, "Large Electrooptic Modulation in a Thermally-Poled Germanosilicate Fiber," IEEE Photon. Tech. Lett., vol. 7, pp. 1177-1179, 1995.

Chapter 4 Evolution of Electro-optic Effect in Silica Fibres During Thermal Poling

4.1 Introduction

Chapter 3 reports the dependence of the induced linear electro-optic effect in silica fibres on the poling conditions. In those studies, an individual fibre device is poled under a given poling condition firstly, and the induced linear electro-optic effect is then measured. This method of optimization of poling conditions is tedious since many fibre devices need to be poled and subsequently characterized. Furthermore, the results obtained may not apply to other fibres of different glass constituents since the poling conditions also depend on material properties. It is therefore advantageous to employ a method to optimize the poling condition for any fibre device while it is being poled. The method of *in situ* fibre poling allows the electro-optic effect to be probed while the device is being poled. On line adjustment of various poling parameters such as poling voltage, poling temperature, etc., forms a feedback loop in optimizing the poling conditions. The *in situ* technique is an easier way to optimize the poling conditions.

In order to understand the thermal poling mechanism in silica glass, it is clear that experimental data about the dynamics of the poling process is needed. The *in situ* poling and characterization provide the time evolution of the induced electro-optic

effect. As will be shown later in the following sections, the measurement of the time evolution of the induced electro-optic effect offers a range of new insights into the poling of glass. These results are important for modeling of thermal poling of silicate glass.

There are only a few reported studies of dynamic behavior of thermal poling of silica. Mukherjee *et al.* reported the temporal dynamics of the induced second-order nonlinearity in thermal poling of fused silica [4.1]. They introduced a model based on simple ionic charge transport in combination with bond orientation. Statman et al. studied the dynamics of the electric-field-induced second-harmonic generation and proposed that an electrical field against the poling field is established during poling [4.2].

This chapter reports on the time evolution of the induced electro-optic effect in germanosilicate fibres during thermal poling. Section 4.2 reports the measurements of the time evolution of the electro-optic effect in the boron-codoped germanosilicate fibre during thermal poling. Section 4.3 presents the effect of thermal history and poling conditions on thermal poling of the aluminium co-doped germanosilicate fibre.

4.2 Evolution of Electro-optic effect in Thermal Poling

In this section, the twin-hole fibre devices studied are made from the boron-codoped germanosilicate fibre, which has been introduced in detail in Chapter 2. The *in situ* technique described in Chapter 2 was used in the measurements of the time evolution

W. Xu, "Thermally Poled Fibre Devices," Ph.D. Thesis, University of Sydney, Australia, March, 1999

of the induced electro-optic effect. A device was poled at 250 °C with a positive poling voltage of 4kV. A 200 V a.c. testing voltage, V_{ac}, running at 8.5kHz, was superimposed on the d.c. poling voltage in order to monitor the induced LEO coefficient.

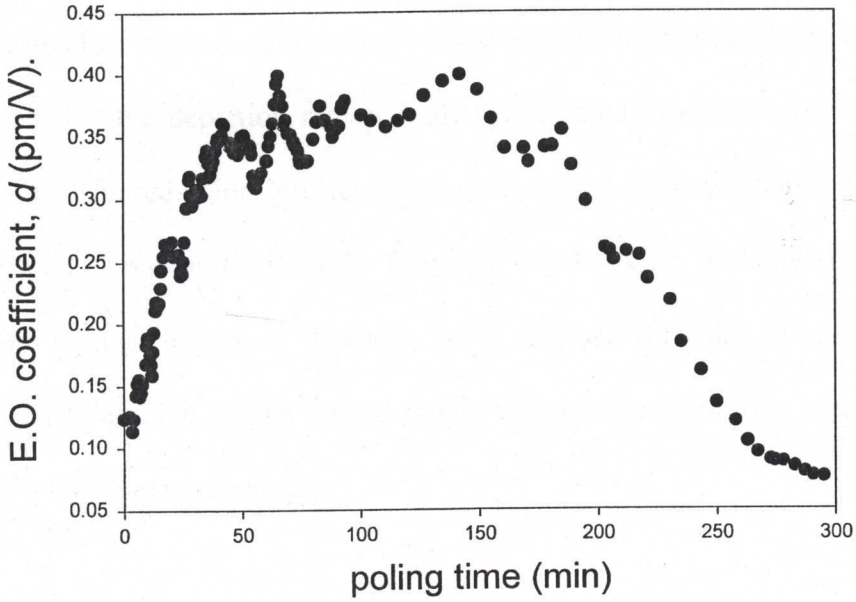

Fig. 4.1 Evolution of the electro-optic coefficient under constant poling conditions.

The *in situ* measurement for the electro-optic effect is shown in Fig. 4.1. As can be seen in the early stage of poling at room temperature, the fibre device becomes electro-optic when a high d.c. electrical field is applied. This is because the d.c. electrical field acts on the third order nonlinearity $\chi^{(3)}$ of the silica fibre [4.2]. Upon

W. Xu, "Thermally Poled Fibre Devices," Ph.D. Thesis, University of Sydney, Australia, March, 1999

application of the d.c. poling voltage, the induced electro-optic effect grows quickly in the first few minutes followed by a period of slower growth which saturates after approximately 60 minutes. After a poling duration of approximately 150 minutes the induced electro-optic effect is observed to decrease, diminishing to almost zero after approximately 300 minutes.

This "depoling effect" (reduction of the electro-optic effect for prolonged thermal poling in silica fibre) is similar to those previously observed by Long *et al.* [4.3]. It is believed that the depletion region leads to the induced electro-optic effect in silica [4.4, 4.5]. The reduction in electro-optic effect with extended poling time is because the depletion region shifts away from the anode to the cathode during prolonged thermal poling [4.6, 4.7]. Because of a decreased spatial overlap between the nonlinearity and the guided optical mode, the electro-optic effect seen by the guided mode in the fibre core reduces.

Fig. 4.2 shows the results, for two other devices, of different poling procedures. In both cases, a heater preheated to 260 °C was used. The solid dots correspond to one device, which has the poling voltage applied seconds before it is placed onto the heater. The solid triangles correspond to the other device, which has the poling voltage applied seconds after it was placed onto the preheated heater. It can be seen that the latter takes longer time to reach a corresponding minimum half wave voltage, which is slightly more than twice that obtained by the former procedure. The fibre device, which has been annealed at the poling temperature for several minutes before

poling commences, shows a greatly reduced electro-optic effect. Due to the movement of the depletion region, the effect of prolonged thermal poling (increase of the half wave voltage or reduction of the electro-optic coefficient) can be clearly seen for both devices.

The higher half wave voltage in this poled fibre than that obtained earlier [4.8, 4.9, 4.10] is thought to be due to two reasons. One is that the lower NA germanosilicate fibres have lower defect populations; the other is that the preform fabrication process did not efficiently incorporate a significant number of oxygen-deficient bonds in the preform core.

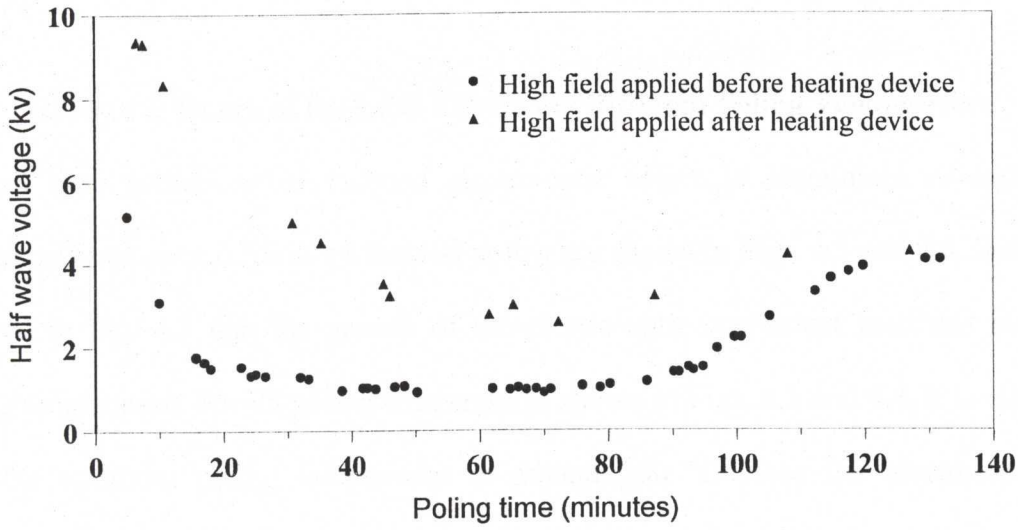

Fig. 4.2 Time evolution of half wave voltage of devices with different poling procedures

If the poling voltage is switched off while the device temperature is still high, the induced electro-optic effect will disappear. Erased devices can be re-poled easily to recover the induced electro-optic effect in a manner similar to that observed by Myers *et. al.* [4.5]. If the poling voltage is switched off after the device reaches room temperature, the induced electro-optic effect remains. This has been verified by characterizing the poled device without the presence of the d.c. high voltage.

4.3 Effect of Poling History on Electro-optic Effect in Thermally Poled Al-codoped Germanosilicate Fibres

The results to be discussed in this section used the twin-hole fibre devices with an aluminum-codoped germanosilicate core, which has been described in Chapter 2.

4.3.1 Growth & Decay of the LEO Effects for Different Poling Temperature

Typical time evolutions of induced electro-optic effect in aluminium co-doped germanosilicate optical fibres by thermal poling are shown in Figs. 4.3 and 4.4. It can be seen in Fig. 4.3 that the growth of the electro-optic coefficient increases with poling temperature. For all poling temperatures shown in Figs. 4.3 and 4.4, it is clear that the optimum poling temperature is around 250 ^{o}C since the electro-optic coefficient has both the highest growth rate and value. At temperatures below the optimum poling temperature, the poling efficiency drops.

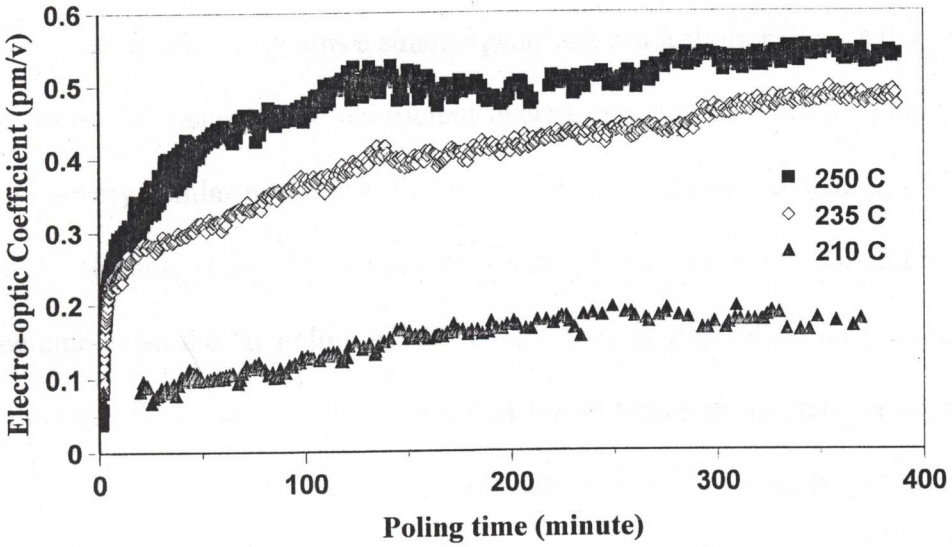

Fig. 4.3 Growth of electro-optic effect for poling temperatures between 210 °C and 250 °C.

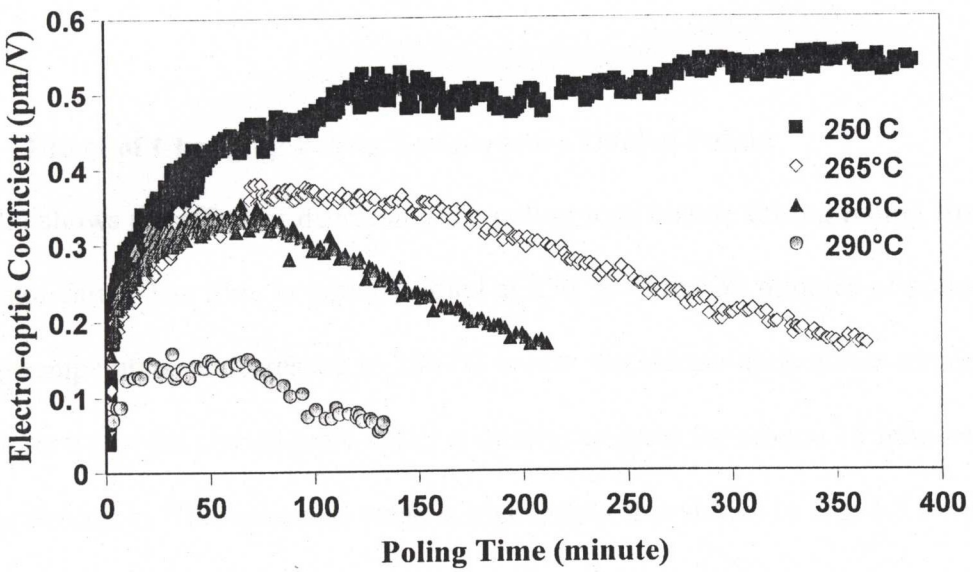

Fig. 4.4 Growth and Decay of electro-optic effect for poling temperatures between 250 °C and 290 °C.

W. Xu, "Thermally Poled Fibre Devices," Ph.D. Thesis, University of Sydney, Australia, March, 1999

For poling temperatures exceeding the optimum value, as shown in Fig. 4.4, the electro-optic coefficient attains a smaller peak value at a shorter time. After reaching a peak value, the electro-optic coefficient decreases with poling time. This "depoling effect" is very similar to those in the thermally poled boron-codoped germanosilicate fibre in Section 4.2. The peaks occurred at shorter time for higher poling temperatures. So the "depoling effect" could strongly depend on temperature. Note that the rate of "depoling" is fairly constant for all higher poling temperatures shown. It must be pointed out that at temperatures above 295 °C, arcing becomes a problem and no unambiguous results can be obtained. Nonetheless, the optimum poling temperature for this aluminium co-doped germanosilicate fibre is clearly around 250 °C and the corresponding maximum achievable electro-optic coefficient is ~0.55 pm/V.

4.3.2 Effect of Changing Poling Temperature During Poling

Fig. 4.5 shows the effect of decreasing the poling temperature during poling from the optimum value. The fibre is initially poled at 250 °C. After 30 minutes of poling, the poling temperature is decreased to 235 °C before the electro-optic effect saturates. It can be seen that the electro-optic effect continues to grow for around 15 minutes until it saturates again. This saturated value is higher than that shown in Fig. 4.3 for a fibre poled at 235 °C with no thermal poling history. The poling temperature is then further decreased to 210 °C after another 15 minutes. The electro-optic effect clearly drops but has a value higher than that shown in Fig. 4.3 for a fibre poled at 210 °C with no thermal poling history. It seems that the initial optimum poling provides a good

thermal poling history or seeding for subsequent thermal poling. The maximum achievable electro-optic coefficient is not substantially different from that obtained from optimum poling.

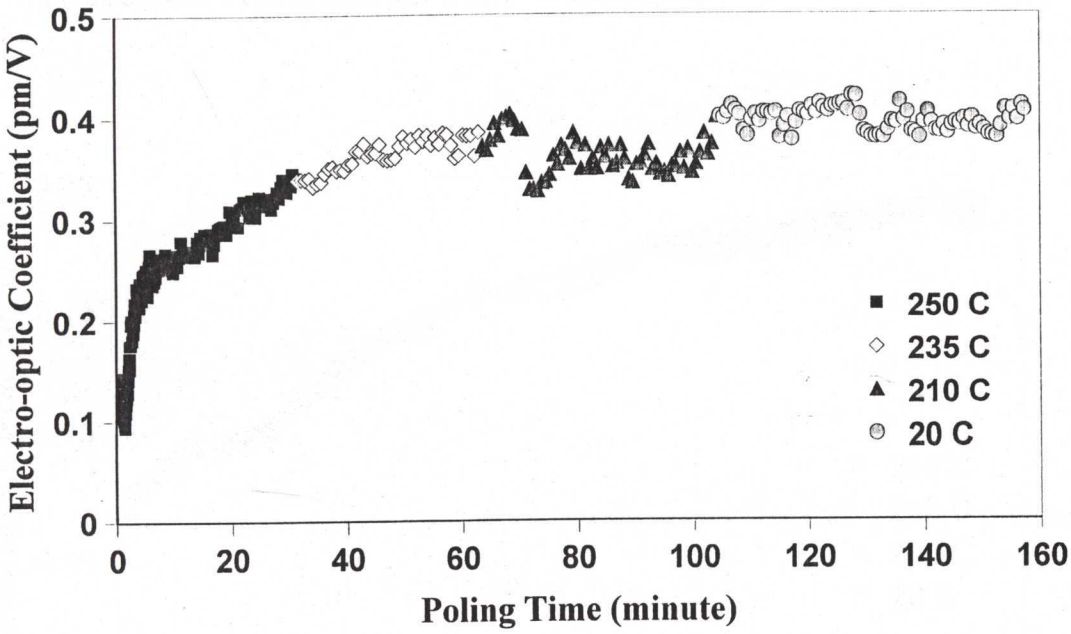

Fig. 4.5. Effect of decreasing poling temperature during poling

Fig.4.6 shows the effect of increasing the poling temperature during poling from below the optimum value. In this case, the fibre is initially poled at 210 °C. Both the growth rate of the electro-optic effect and its value are similar to that shown in Fig. 4.3. After 30 minutes of poling, however, the poling temperature is increased to 235 °C. It can be seen that both the growth rate of the electro-optic effect and its value are increased. At the end of a further 3 hours of poling, the growth rate drops to zero and the electro-optic effect saturates. As soon as the poling temperature is further

increased to 250 °C, the growth rate increases again but lesser than that at the previous poling temperature. The value of the electro-optic coefficients obtained, in the second and third poling temperature, are around 60 % less than that obtained from optimum poling. It seems that the initial non-optimum poling reduces the poling potential of the fibre for subsequent, even though optimum, thermal poling.

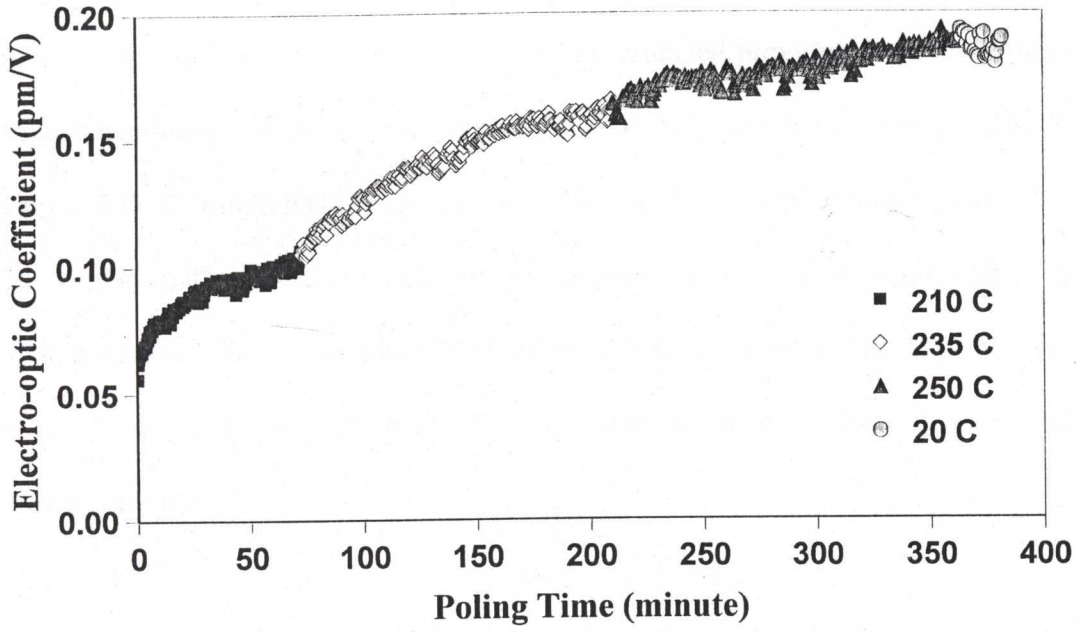

Fig. 4.6 Effect of increasing poling temperature during poling

Fig. 4.6 indicates that pre-poling at temperatures below the optimum value results in lower achievable electro-optic coefficient when compared with pre-poling at the optimum value as shown in Fig. 4.5. When looking at these results from a totally different angle, it can be interpreted that a higher rate of change of poling temperature during initial poling can achieve a higher electro-optic coefficient. This statement is

W. Xu, "Thermally Poled Fibre Devices," Ph.D. Thesis, University of Sydney, Australia, March, 1999

true as long as arcing does not occur. Arcing simply destroys the core and/or the fibre, which makes the measurement impossible due to high attenuation and/or absence of optical signal.

For a given poling voltage, the chance of arcing is higher for higher poling temperature, which is around 290 °C, for the fibre studied. Fig. 4.7 shows the results where the poling temperature is increased from 210 °C to 325 °C in steps of 30 minutes. Arcing does not occur at 295 °C, as experienced previously, possibly due to the slow ramping up of the poling temperature. The defects, which are responsible for arcing at 295 °C, might have been "annealed" by the slow ramping of temperature. As a consequence, the defects, which are responsible for the electro-optic effect, are finally consumed due to the absence of arcing at higher temperatures. It can be seen that the peak achievable electro-optic coefficient is close to that obtained from optimum poling.

Note also that at 295 °C, without arcing, the effect of "depoling" begins to creep in. It must be pointed out that the "depoling rate" appears different from the non-prepoled fibres shown in Fig. 4.4. When the poling temperature is further increased to 325 °C, however, arcing did take place and the fibre was destroyed. This could imply that the "depoling" effect might be associated with the arcing mechanism, which causes the ultimate dielectric breakdown.

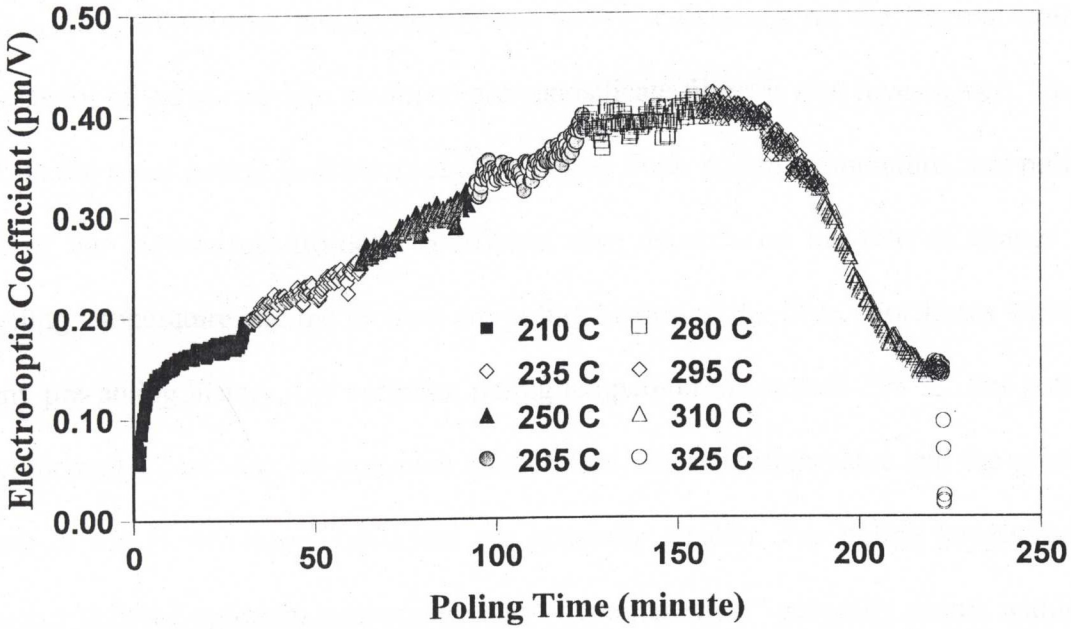

Fig. 4.7 Due possibly to the increased dielectric breakdown threshold through "annealed" poling, higher poling temperature was allowable

4.4 Conclusion

The time evolution of the induced electro-optic effect in the boron-codoped germanosilicate fibre during poling is studied employing *in situ* measurements. The result reveals the "depoling effect" in prolonged thermal poling. Exceeding the optimal poling duration results in reduction of the poling induced electro-optic effect. This may be due to the decreasing overlap between the optical core mode and the nonlinear depletion region. Application of a d.c. high voltage to a fibre device before poling makes the fibre device exhibit an electro-optic effect. A fibre device, which has been annealed at the poling temperature for several minutes before poling begins, shows a much smaller electro-optic effect than one without annealing before poling.

The effect of thermal poling history and poling conditions on the thermal poling behavior of the aluminium co-doped germanosilicate fibres is also investigated. Apart from the usual poling parameters such as poling field, poling temperature, and poling time, the induced electro-optic coefficient also depends on the rate of change of poling temperature and the thermal pre-poling history of the fibre. For fibres without any pre-poling history, the optimum poling temperature is around 250 ^{o}C. For poling temperatures less than the optimum temperature, the saturation value and the growth rate of the electro-optic coefficient are generally smaller. For poling temperatures higher than the optimum temperature, the " depoling effect" generally occurs within a shorter time. It is found that this "depoling effect" may be directly related to the mechanism of dielectric breakdown in glass. Generally, a higher rate of change of poling temperature during initial poling results in a higher electro-optic coefficient.

4.5 References

[4.1] N. Mukherjee, R.A. Myers and S.R.J. Brueck, "Dynamics of second-harmonic generation in fused silica", *J. Opt. Soc. Am. B.*, vol. 11, pp. 665-669, 1994.

[4.2] D. Statman and J. A. Georges III, "Charge dynamics and poling in glass waveguides," J. Appl. Phys., vol. 80, pp. 654-661, 1996.

[4.3] X. C. Long, R.A. Myers and S. R. J. Brueck, "A poled electrooptic fiber", IEEE Photon. Tech. Lett., vol.8, pp. 227-229, 1996.

[4.4] P. G. Kazansky and P. St. J. Russell, "Thermally poled glass: frozen-in electric field or oriented dipoles?" Opt. Comm., vol. 110, pp. 611-614, 1994.

[4.5] R. A. Myers, N. Mukherjee, and S. R. J. Brueck, "Large second-order nonlinearity in poled fused silica," Opt. Lett., vol. 16, pp. 1732-1734, 1991.

[4.6] T. G. Alley and S. R. J. Brueck, "Visualization of the nonlinear optical space-charge region of bulk thermally poled fused-silica glass," Opt. Lett., vol. 23, pp. 1170-1172, 1998.

[4.7] W. Xu, D. Wong, and S. Fleming, "Evolution of the linear electro-optic coefficient and the third order nonlinearity in prolonged negative thermal poling," submitted to Electronics Letters.

[4.8] T. Fujiwara, D. Wong, and S. Fleming, "Large Electrooptic Modulation in a Thermally-Poled Germanosilicate Fiber," IEEE Photon. Tech. Lett., vol. 7, pp. 1177-1179, 1995.

[4.9] T. Fujiwara, D. Wong, Y. Zhao, S. Fleming, S. Poole and M. Sceats, "Comparison of linear electro-optic coefficient induced by UV-excited and thermal poling in a germanosilicate fibre", Tech. Dig. CLEO/Pacific Rim'95, vol. FE5, pp. 177, 1995.

[4.10] T. Fujiwara, D. Wong, Y. Zhao, S. Fleming, S. Poole and M. Sceats, "Electro-optic modulation in germanosilicate fibre with UV-excited poling", Electron. Lett., vol. 7, pp. 573-575, 1995.

Chapter 5 Stability of Electro-optic Effect in Thermally Poled Fibres

5.1 Introduction

The optimum thermal poling conditions have been investigated in Chapter 3. The *in situ* poling technique has been used in order to optimize the linear electro-optic effect during thermal poling in Chapter 4. In this chapter, the stability of the electro-optic effect induced into the boron-codoped germanosilicate fibre devices is studied using the *in situ* technique to measure the decay of the electro-optic effect in the thermally poled fibre devices at elevated temperature. The lifetime of the induced electro-optic effect at room temperature is predicted using Arrhenius analysis. The fibre geometry and the glass constituents of the boron-codoped germanosilicate fibre used in this chapter have been described in Section 2.2 of Chapter 2. The MZI experimental setup used in this Chapter has also been introduced in Section 2.3 of Chapter 2.

Previous reports of the decay lifetime for thermally poled devices at room temperature vary widely between tens of days [Ref. 5.1 extrapolated to 298K] and hundreds of years [5.2]. Such large variation may be attributed to the many factors involved in generating the electro-optic effect such as dopant concentration, poling conditions and device geometry, all of which have confused attempts to understand the underlying mechanism. In contrast to previously reported measurements [5.1, 5.2, 5.3], the decay

behavior in this thermally poled fibre did not exhibit a single exponential dependence, but was best fitted with a distribution of relaxation times. This observation is consistent with other reports of relaxation in germanosilicate glass such as decay behaviour of UV-induced defects in GeO_2-SiO_2 glass [5.4] and thermal annealing of fibre Bragg gratings [5.5, 5.6]. The gratings are formed by UV-induced change in refractive index. The index changes may be visualized as an effect of trapped defect sites with a distribution of activation energies [5.7].

5.2 Decay of the LEO Effect in Thermally Poled Fibres

Three twin-hole fibre devices were manufactured from the same boron codoped germanosilicate fibre and poled at 523 K using a d.c. poling voltage of +4 kV. After a poling duration of 60 min., the temperature of the heating element was reduced and the d.c. poling field turned off. Fig. 5.1 shows the natural log of the measured decay of the electro-optic coefficient $r(t)$ at three temperatures of 343 K, 383 K and 443 K, normalized to its value at time $t = 0$ measured just after the poling field was turned off.

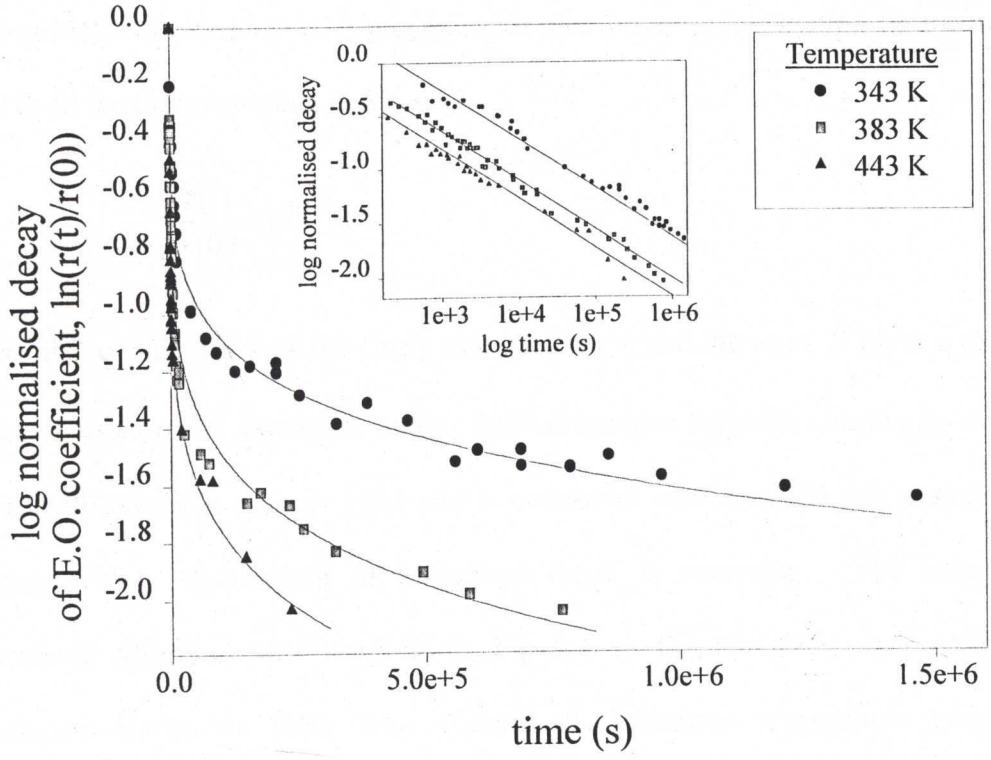

Fig. 5.1 Log of the normalized decay of the electro-optic effect in thermally poled fibre. The insert shows the data plotted on a log-log scale. Also shown are stretched exponential curves fitted using the parameters given in Table 5.1.

Previously reported measurements of the decay of a second harmonic generation signal at elevated temperature in both thermally poling [5.2] and UV-excited poling [5.3] have been fitted with a single exponential to characterize the decay of the electro-optic effect. The decay data plotted in Fig. 5.1, however, clearly does not exhibit this behavior. When plotted on a log-log scale (see insert to Fig. 5.1) the

measured decay follows an almost linear dependence, suggesting that a stretched exponential, characteristic of a process with distribution of relaxation times, may be used to fit the measured data [5.8],

$$\frac{r(t)}{r(0)} = e^{-(kt)^{\beta}} . \tag{5.1}$$

In the above equation k is the decay rate coefficient and the term β gives a measure of the distribution of relaxation times. Such dispersive behavior commonly exists in disordered materials such as glass and is consistent with a model that assumes one process with a distribution of relaxation times is occurring. The Marquardt-Levenberg algorithm was used to fit Eq. 5.1 to the measured data giving the parameters shown in Table 5.1. Across the measured temperature range, the distribution of relaxation times β remained approximately constant which is consistent with other reports of relaxation in strong glass formers such as silica [5.9, 5.10]. In Ref. 5.4, the values of β for the decay behavior of UV-induced defects in GeO_2-SiO_2 glass are approximately 0.1~0.2, and β has been found to increase with increasing the annealing temperature. On the other hand, β in the UV-poled GeO_2-SiO_2 glass is equal to almost exactly unity for the whole temperature range of experiments, which is equivalent to the single exponential decay [5.3].

Temperature K.	decay rate coefficient k (s^{-1})	dispersion parameter β
343	9.22×10^{-7}	0.15
383	2.78×10^{-6}	0.16
443	8.05×10^{-6}	0.15

Table 5.1 Values of the decay rate coefficient k and dispersion parameter β for the three measured temperatures.

5.3 Arrhenius Analysis

As shown in Fig. 5.2, the decay rate coefficient k was observed to follow a log dependence with inverse temperature. This behavior has previously been observed by other authors [5.2, 5.3] and may be represented by the well known Arrhenius equation,

$$\ln(k) = \ln(A) - {}^{E_A}\!/_{RT}\,. \tag{5.2}$$

In the above equation A is the pre-exponential or frequency factor, E_A the activation energy, $R = 8.31$ J/mol.K is the molar gas constant and T the absolute temperature. The factor A is a measure of the frequency of attempts the system makes to relax, and

$e^{E_A/RT}$ is a measure of the probability of an attempt being successful. Extrapolating the measured data in Fig. 5.2, the rate coefficient at 298 K may be estimated as $k = 2.55 \times 10^{-7}$ s^{-1}. This implies an average for the distribution of decay times at room temperature of approximately 45 days. This value is on the low end of other reported values for the lifetime of the SON and the electro-optic coefficient in the poled silica glass which are typically in the range of hundreds of days [5.1, 5.3].

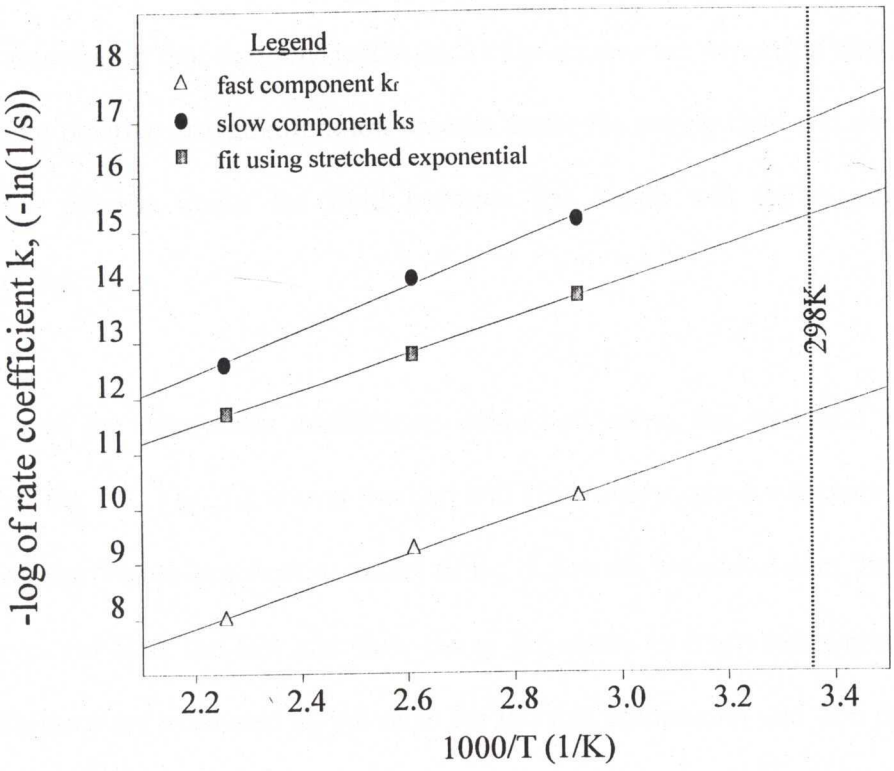

Fig. 5.2 Arrhenius plots of the decay rate coefficients measured at elevated temperatures.

An alternative model, which has been used for analyzing the decay behavior, is to fit the measured data with two exponential functions [5.11]:

$$r(t) = A_f e^{-k_f t} + A_s e^{-k_s t} \tag{5.3}$$

In the above equation A_f and A_s are the initial values of the fast and slow components of the decay respectively ($r(0) = A_f + A_s$), and k_f, k_s are the corresponding decay rate coefficients. Eq. 5.3 is consistent with a model for the linear electro-optic effect induced in thermally poled silica fibres [5.12]. The model is based on the assumption that two physically distinct processes are occurring during thermal poling, the positive charge migration process under the poling field and the molecular ionization process under the field between the anode and the negative charge depletion region.

Along with the decay rate coefficients calculated using the stretched exponential model of Eq. 5.1, Fig. 5.2 shows the fast and slow decay rate coefficients calculated by fitting the double exponential model of Eq. 5.3 to the measured data. Extrapolating the curves for both the fast and slow decay processes to room temperature (298 K) their lifetimes are estimated as 1.6 days for the fast component and 266 days for the slow component. The value for the slow component is consistent with other reported values for the decay rate coefficient [5.3].

The experimental uncertainty in determining the decay rate coefficients plotted in Fig. 5.2 does not substantiate distinguishing between the values of the slopes of these three graphs. To within experimental error, the slopes of the three Arrhenius plots shown in

Fig. 5.2 are approximately the same and give an activation energy E_A for the stability of the electro-optic effect in the range of 25-28 kJ/mol (0.28-0.31 eV). This range of values is smaller than the value of 0.4 eV reported by both Mukherjee for thermally poled bulk fused silica [5.1] and Fujiwara for UV poled bulk germanosilicate glass preform slabs [5.3]. This value was correlated with the decay rate for GeE' color centres by Fujiwara [5.3]. The absence of boron, the different poling geometry and mechanisms involved, however, makes these results difficult to compare.

5.4 Conclusion

Using the *in situ* technique to measure the induced electro-optic effect at elevated temperature, the decay characteristics of thermally poled twin hole B/Ge co-doped fibre devices have been studied. In contrast with previous reports which model the decay characteristic of similar devices using a single exponential, the measured decay in this fibre type was best fitted using a stretched exponential. Such behavior, characteristic of a distribution of relaxation times, is consistent with other thermal relaxation processes observed in germanosilicate glass such as the thermal annealing characteristics of fibre Bragg gratings and decay behaviour of UV-induced defects in GeO_2-SiO_2 glass. The rate coefficients of the decay process measured at different temperatures were found to follow the well known Arrhenius relation. Using this equation to extrapolate the data to room temperature, an average decay rate for the process was estimated to be approximately 45 days. Alternately, using the double exponential model and ignoring the early part of the data that decays quickly, a more

stable component of the process may be extracted with a lifetime of approximately 260 days.

5.5 References

[5.1] N. Mukherjee, R.A. Myers and S.R.J. Brueck, "Dynamics of second-harmonic generation in fused silica," J. Opt. Soc. Am. B., vol. 11, pp. 665-669, 1994.

[5.2] O. Sugihara, T. Hirama, H. Fujimura and N. Okamoto, "Second-order nonlinear optical properties from poled silicate channel waveguide," Optical Review, vol. 3, pp. 150-152, 1996.

[5.3] T. Fujiwara, M. Takahashi and A. J. Ikushima, "Decay behaviour of second-order nonlinearity in GeO_2-SiO_2 glass poled with UV-irradiation," Electron. Lett., vol. 33, pp. 980-982, 1997.

[5.4] M. Ohama, T. Fujiwara and A. J. Ikushima, "Decay behavior of UV-induced defects in Ge-doped SiO_2 glass," Proceeding of ECOC'98, September 20-24, Madrid, Spain, pp. 141-142, 1998.

[5.5] K.E. Chisholm, K. Sugden and I. Bennion, "Effects of thermal annealing on Bragg fibre gratings in Boron/Germanium co-doped fibre," J. Phys. D., Appl. Phys., vol. 31, pp. 61-64, 1998.

[5.6] H. Inglis, "Photo-induced effects in optical fibres," PhD dissertation, University of Sydney, 1996.

[5.7] S. kannan, J. Z. Y. Guo and P. J. Lemaire, "Thermal stability analysis of UV-induced fiber Bragg gratings," IEEE J. Lightwave Technol., vol. 15, pp. 1478-1483, 1997.

[5.8] R.G. Palmer, D.L. Stein, E. Abrahams and P.W. Anderson, "Models of hierarchically constrained dynamics for glassy relaxation," Phys. Rev. Lett., vol. 53, pp. 958-961, 1984.

[5.9] R. Bohmer and C.A. Angell, "Correlations of the nonexponentially and state dependence of mechanical relaxations with bond connectivity in Ge-As-Se supercooled liquids," Phys. Rev. B, vol. 45, pp. 10091-10094, 1992.

[5.10] C.A. Angell, "Formation of glasses from liquids and biopolymers," Science, vol. 267, pp. 1924-1935, 1995.

[5.11] H. Imai, S. Horinouchi, Y. Uchida, H. Yamasaki, K. Fukao, G. Zhang, T. Kinoshita, K. Mito, H. Hirashima and K. Sasaki, "Time-dependant decay of quadratic non-linearity in corona-poled silicate glass films," J. Non-Cryst. Sol., vol. 196, pp. 63-66, 1996.

[5.12] D. Wong, W. Xu, J. Arentoft, and S. Fleming, "Positive and negative thermal poling of germanosilicate fibres," Technical Digest of OFC/IOOC'99 (Thursday, February 25), ThG4, pp. 90-92, San Diego, USA, 1999.

Chapter 6 Mechanism of Thermal Poling of Silica Fibres

6.1 Introduction

Thermal poling has been demonstrated to produce a large LEO coefficient, r, and second order nonlinearity, $\chi^{(2)}$, in silica glass [6.1]. But the mechanisms of the thermal poling effects are still unclear. There are basically three thermal poling mechanisms, which have been proposed. One is space charge migration and ionization leading to a high frozen-in field in the anodic region of the thermally poled silica glass. The action of the frozen-in field on the intrinsic third order nonlinearity $\chi^{(3)}$ of silica gives $\chi^{(2)}$ [6.2, 6.3]. Another possible mechanism is dipole/bond orientation under the poling field. The oriented dipoles/bonds break the symmetrical structure of silica glass and result in $\chi^{(2)}$ [6.4]. The last is the combination of both the frozen-in field mechanism and the dipole/bond orientation mechanism [6.5, 6.6]. Although various mechanisms have been suggested, no concrete conclusion could be made.

To understand the mechanism of this thermal poling effect, different experiments have been carried out. Kazansky *et al.* offered experimental evidence that a frozen-in space charge field near the anodic surface was responsible for the appearance of the quadratic nonlinearities in thermally poled glass having Na^+ concentration of 2 ppm

and OH concentration of 200 ppm [6.7]. Wada *et al.* showed that Na^+ plays a key role in thermal poling of bulk fused silica [6.8]. Alley *et al.* observed that a second, longer time scale, charge transport took place in thermal poling of bulk silica samples [6.9]. They proposed that the precursor in space-charge formation is hydrogenated ions from water already in the glass. The hydrogenated ions such as H_3O^+ were responsible for charge transportation as well as dipole charge distribution.

There are a few experimental revelations of the charge distributions in thermally poled silica glasses. Kazansky *et al.* obtained alternating charge distributions in thermally poled silica glasses using a laser induced pressure pulse technique [6.10]. Margulis *et al.* employed an interferometric etching technique to measure HF etch rates of poled and unpoled glasses [6.11]. They found a negatively charged region that was 5.5 μm deep and a positively charged region that was 34 μm deep from the anode in a 1 mm thick silica sample that was poled at 3 kV and 280 °C for 225 minutes. Margulis *et al.* also found that a highly positively charged thin layer of glass (< 100 nm) was formed between the anode and the negatively charged region in some poled samples. More recently, T. G. Alley *et al.* reported a study of HF etching transverse to the poling direction to reveal a cross section of the nonlinear region of thermally poled glass [6.12]. They observed that a peaked ridge below the anode surface moved deeper into the glass logarithmically with poling time.

This chapter aims to clarify the mechanisms of thermal poling of silica fibre. The fibre used in all the experiments in this chapter is the aluminum co-doped germanosilicate

twin-hole fibre, which is described in detail in Chapter 2. The fibre material contained 0.18 ppm (in weight) Na^+, which was determined by Instrumental Neutron Activation Analysis (INAA). This analysis technique has approximately +/- 10% accuracy and a detection limit of 0.05 ppm (in weight) for Na^+. It is known that Na^+ can play an important role in thermal poling [6.2, 6.6]. The experimental setup used is the Mach-Zehnder interferometer for *in situ* poling measurements as described in Chapter 2.

In Section 6.2, an innovative method is introduced to measure the frozen-in fields in thermally poled fibre devices. In Section 6.3, the same measurement technique is employed to measure $\chi^{(3)}$ of the fibre core. It is found that $\chi^{(3)}$ of the fibre core increases by a factor of ~2 after thermal poling. In Section 6.4, the processes of thermal poling of silica fibre are proposed based on positive and negative thermal poling. Section 6.5 demonstrates movement of charge distributions in thermally poled silica fibre. Section 6.6 studies evolution of the LEO coefficient and $\chi^{(3)}$ during prolonged negative thermal poling.

6.2 Measurement of the Frozen-in Fields in Thermally Poled Silica Fibres

A twin-hole fibre device was poled at +3.5 kV d.c. voltage and at 250 °C for ~ 1 hour. To investigate this frozen-in field in the poled fibre device, a small a.c. testing voltage, V_{ac}, was superimposed onto the external d.c. voltage, V_{dc}, in the MZI setup.

It can be seen in Fig. 6.1 (a) that the measured total second order nonlinearity, $\chi^{(2)}_{total}$, has a linear dependence on V_{dc}. The experimental data is fitted using

$$\chi^{(2)}_{total} = 3\chi^{(3)}_{poled} E_{dc} + \chi^{(2)}_{residual}, \tag{6.1}$$

where $\chi^{(3)}_{poled}$ is the third-order nonlinearity of the poled fibre device, and $\chi^{(2)}_{residual}$ is the thermal poling induced residual SON. Fig. 6. 1 (a) shows that $\chi^{(2)}_{total}$ became zero when -3.7 kV V_{dc} was applied to the poled fibre. This means $\chi^{(2)}_{residual}$ was canceled out by the external d.c. electrical field induced second order nonlinearity $\chi^{(2)}_{dc}$. $\chi^{(2)}_{dc}$ [6.2] is expressed by

$$\chi^{(2)}_{dc} = 3\chi^{(3)}_{poled} E_{dc}. \tag{6.2}$$

It is supposed that $\chi^{(2)}_{residual}$ is due to the frozen-in field

$$\chi^{(2)}_{residual} = 3\chi^{(3)}_{poled} E_{frozen}. \tag{6.3}$$

Combining Eqs. 6.1 and 6.3, $\chi^{(2)}_{total}$ of the thermally poled fibre can be expressed as

$$\chi^{(2)}_{total} = 3\chi^{(3)}_{poled} \left(E_{dc} + E_{frozen}\right). \tag{6.4}$$

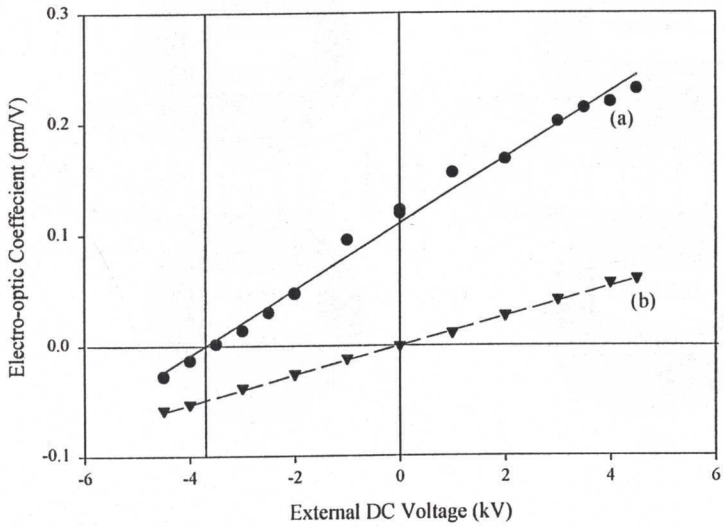

Fig. 6.1 (a) External electrical field induced $\chi^{(2)}_{total}$ after poling (solid line);

(b) External electrical field induced $\chi^{(2)}_{total}$ before poling (dash line).

Based on Eq. 6.4, when the frozen-in field is balanced by V_{dc}, the $\chi^{(2)}_{total}$ becomes zero. So both the magnitude and direction of the frozen-in field in thermally poled fibre can be obtained. The magnitude of the frozen-in field in this fibre device was estimated as 200 V/μm. The direction of the frozen-in field is opposite to the direction of the external electrical field caused by V_{dc}. Fig. 6.2 shows the frozen-in field induced in the fibre device by thermal poling. The formation of the frozen-in field will be further investigated in Section 6.4.

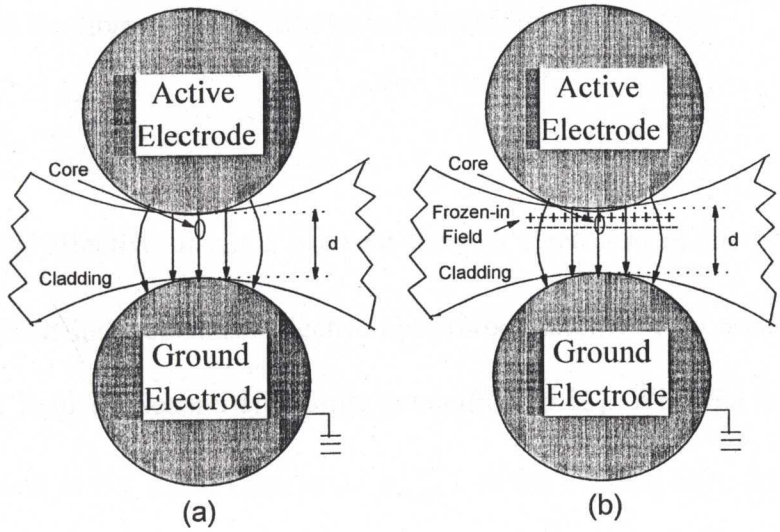

Fig. 6.2 Field distribution for an external positive voltage applied to (a) an unpoled fibre device and (b) a poled fibre device with a frozen-in field.

6.3 Measurement of $\chi^{(3)}$ of Silica Fibres

In the above experiment, an a.c. testing voltage V_{ac} was superimposed onto the d.c. voltage V_{dc}. For an unpoled fibre, the electro-optic modulation can still be obtained when V_{dc} is applied to the fibre [6.2] because V_{dc} can cause the second-order nonlinearity

$$\chi_{dc}^{(2)} = 3\chi_{unpoled}^{(3)} E_{dc}, \tag{6.5}$$

where $\chi^{(3)}_{unpoled}$ is the third-order nonlinearity of the unpoled fibre and E_{dc} is the electrical field in the fibre core. E_{dc} can be calculated from V_{dc} using

$$E_{dc} = \frac{V_{dc}}{d_{eff}}, \tag{6.6}$$

where d_{eff} is the effective distance between the two electrodes of the fibre device. The electrical field induced linear electric-optic modulation is also well known as Electrical Field Induced Second Harmonic generation [6.13]. With the help of Eqs. 6.5 and 6.6 as well as Eq. 2.8 in Chapter 2, $\chi^{(3)}_{unpoled}$ of the unpoled fibre device can be expressed by

$$\chi^{(3)}_{unpoled} = \frac{n_{co}\lambda d^2_{eff}}{6\pi L V_{ac} V_{dc}}\Delta\phi, \tag{6.7}$$

where $\Delta\phi$ is the phase change corresponding to V_{ac}. As each quantity on the right side of Eq. 6.7 is measurable, the value of $\chi^{(3)}_{unpoled}$ can be calculated. Fig. 6.1 (b) shows the measured $\chi^{(2)}_{dc}$ of the unpoled fibre device as a function of the external d.c. voltage, V_{dc}. It follows from Eq. 6.5 that $\chi^{(3)}_{unpoled}$ can be estimated from the slope of the plot. For the twin-hole fibre device, conductive chemical solution was filled into the two holes in order to get rid of air gaps between the electrodes and the cladding. $\chi^{(3)}_{unpoled}$ of the core of twin-hole fibre is estimated to be 1.5~1.86 $\times$ 10^{-22} $(m/V)^2$, which is in the same range as $\chi^{(3)}$ for bulk silica glass of 1.8 $\times$ 10^{-22} $(m/V)^2$ [6.14].

Fig. 6.1 shows that the slope of the external d.c. electrical field induced LEO modulation in the thermally poled fibre is larger than that of the external d.c. electrical field induced LEO modulation in the unpoled fibre. According to Eqs. 6.1 and 6.5, the slopes are proportional to the third order nonlinearity of the fibre core. This means that the third-order nonlinearity of the poled fibre, $\chi^{(3)}_{poled}$, becomes larger than the third-order nonlinearity of the unpoled fibre, $\chi^{(3)}_{unpoled}$. The ratio of $\chi^{(3)}_{poled}$ to $\chi^{(3)}_{unpoled}$ in Fig. 6.1 is ~2. It follows that a change in material property might have occurred and hence the value of the third order nonlinearity has changed. In the case of thermal poling, this could be associated with the migration of charges in the glass lattice as well as the re-distribution of residual frozen-in thermal stress. In either case, both the material property and the internal field can be changed. It would be interesting to investigate the relaxation time of these changes.

6.4 Positive and Negative Thermal Poling

Two identical fibre devices made from the aluminum co-doped germanosilicate fibre were used in the thermal poling experiments. The positive thermal poling means that the positive poling voltage is applied to the electrode in the hole to which the core is closer. The negative thermal poling means that the negative poling voltage is applied to the electrode in the hole to which the core is closer.

One fibre device was positively poled at +3.5 kV and at 250 °C for ~ 1 hour and the result of the *in situ* measurement is shown in Fig. 6.3. A LEO signal was observed at

room temperature as soon as the poling voltage was applied to the device. It is due to the action of the d.c. poling field on the intrinsic $\chi^{(3)}$ of the glass [6.2]. The LEO signal decreased in the initial 1 to 2 minutes of positive thermal poling until reaching a minimum. After the initial decrease of LEO signal, it started increasing until it saturated. When switching off the d.c. poling voltage at room temperature after poling, the LEO signal dropped due to the applied d.c. poling field no longer acting on the $\chi^{(3)}$. The LEO effect obtained from poling is the residual LEO coefficient. The proposed charge distributions for positive thermal poling are shown in Fig. 6.4.

The other device was negatively poled at -3.5 kV and at 250 °C for ~ 1 hour. Fig. 6.5 shows the results of the *in situ* measurement. A LEO signal was observed again as soon as the d.c. poling voltage was applied to the device. Almost identical to the positive thermal poling, the LEO signal decreased to zero (a minimum) during the initial few minutes of negative thermal poling. However, very different from the positive thermal poling, it then remained zero during the rest of the poling process. On switching off the poling voltage at room temperature after poling, the LEO signal became non-zero. The proposed charge distributions for negative thermal poling are shown in Fig. 6.6.

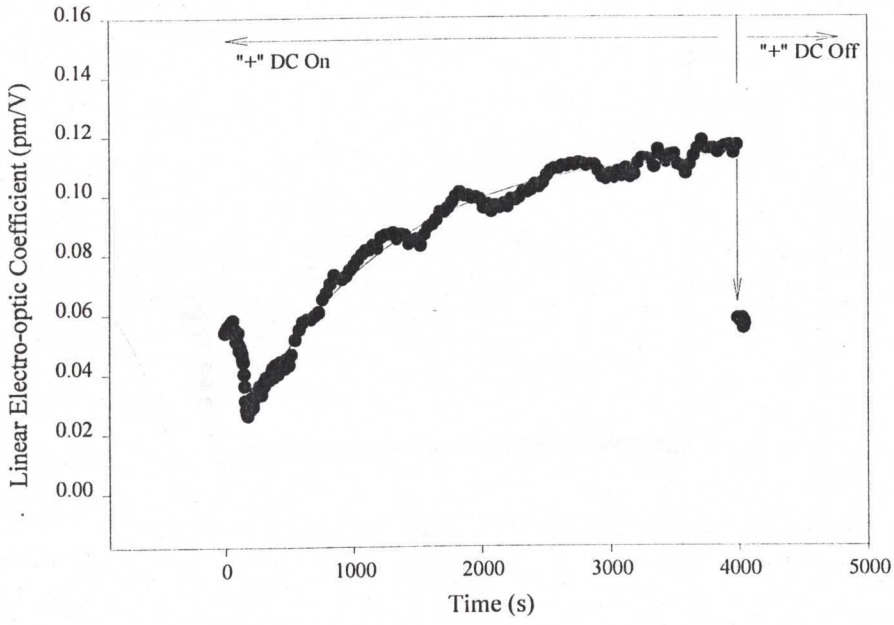

Fig. 6.3 Positive thermal poling @+3.5 kV and 250 °C for ~1 hour (•, experimental data; solid line, theoretical curve).

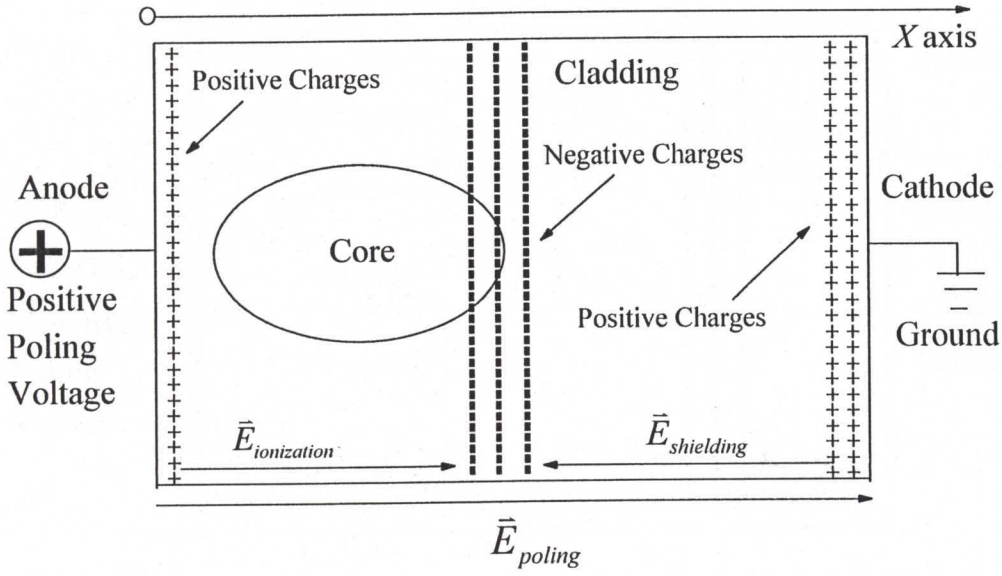

Fig. 6.4 Proposed charge distributions for positive thermal poling.

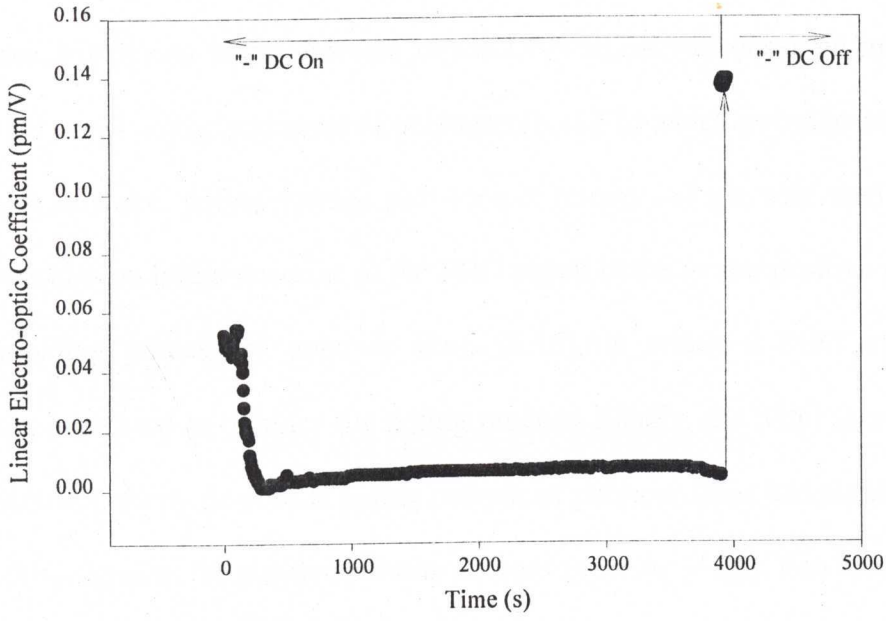

Fig. 6.5 Negative thermal poling @-3.5 kV and 250 °C for ~1 hour (•, experimental data).

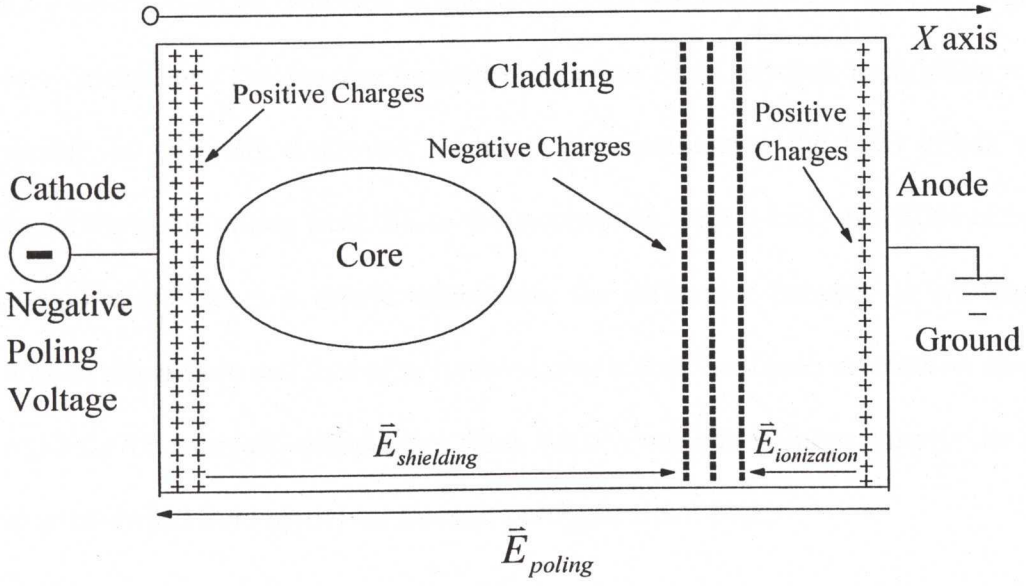

Fig. 6.6 Proposed charge distributions for negative thermal poling.

Compared to silica fibre, polymer materials have very different *in situ* thermal poling processes. Firstly, no initial decrease of the LEO signal was observed in the *in situ* positive thermal poling processes of polymers [6.15], in which a similar measurement technique of a d.c. poling voltage plus an a.c. testing voltage was used. Secondly, there was also no initial decrease of the SHG signal in the *in situ* positive polarity dc-corona poling process of polymer films [6.16], in which a SHG measurement technique was used to monitor the poling process. Finally, the SHG signal in the *in situ* negative polarity dc-corona poling process of polymer films had similar behavior to the SHG signal in the positive polarity dc-corona poling [6.16]. The *in situ* signal in the negative polarity dc-corona poling did not have any reduction and did not become zero throughout the rest of the poling process, and this behavior is very different from the process of negative thermal poling of silica fibre. A LEO signal increasing from the start of the poling until reaching a saturation level, as observed during poling of the polymers, is to be expected if the mechanism responsible for the LEO signal is dipole orientation. The average random orientation of the dipoles, prohibiting a LEO response, is gradually destroyed as the dipoles, possessing the LEO effect, orient themselves to the poling field. Since the mechanism for the LEO and SON effects in these poled polymers is dipole orientation, the difference between *in situ* thermal poling of silica fibre and that of polymer suggests that the dipole orientation model is unsuitable for thermally poled silica fibre. Rather, our observations support the space charge electrical field model for thermal poling of silica fibre.

The observations on dynamics of positive and negative thermal poling can be explained with the model of charge migration and ionization [6.2] as described in the following. When the fibre devices were heated to a temperature of ≥ 200 °C, positive ions (Na^+ was suggested [6.2, 6.6]) in the glass network became mobile and migrated to the cathode under the poling field regardless of which electrode is used as the cathode. The migrating positive charges established a shielding field opposite to the poling field. So the total electrical field seen by the core decreased as indicated by initially decreasing LEO signals during positive and negative thermal poling. The positive charges stopped migrating when the shielding field balanced the poling field. As shown in Figs. 6.3. and 6.5, the charge migration appears to be a linear process and can be fitted by

$$r(t) = r_o\left(1 - \frac{t}{\tau_1}\right), \tag{6.8}$$

where r_0 is the initial LEO coefficient due to the action of the d.c. poling field on $\chi^{(3)}$, $r(t)$ is the total LEO coefficient during poling, and τ_1 is the time constant which is the time taken for the shielding field to build up. It took ~90 seconds for the shielding field to fully build up in both cases. τ_1 is a function of glass constituents, poling temperature, poling field and distance between the two holes.

When the shielding field had built up within the initial 90 seconds of poling, the region near to the anode was depleted of positive ions. This resulted in negative charges being embedded in the glass matrix in the anodic region. Due to the short distance between the anode and the negatively charged depletion region, there was a

very strong electrical field in this region. It is theorized that ionization took place in the high field of the anodic region, and electrons moved into the anode. The ionization process created a positively charged layer between the anode and the negatively charged region. An ionization field thus existed between the ionized positive charge region and the negative charge depletion region. As shown in Fig. 6.3, the build up of the ionization field appears to be a single exponential process and can be fitted by

$$r(t) = r_o + r_1\left(1 - e^{-t/\tau_2}\right), \tag{9}$$

where r_0 is the initial LEO coefficient of the increasing part in positive thermal poling, r_1 is the saturated LEO coefficient, τ_2 is the time constant of the single exponential process and is ~20 minutes for this device. Like τ_1, τ_2 is also a function of glass constituents, poling temperature and poling field. A single exponential fit means that the ionization process may be the dominant process after the shielding field has built up.

The residual LEO effect due to positive thermal poling results from the frozen-in ionization field, which has the same direction as the poling field. It can be seen that the LEO coefficient dropped to a smaller residual LEO value as soon as the d.c. poling voltage was turned off at room temperature. In contrast, the residual LEO effect due to negative thermal poling results from the frozen-in shielding field, which has opposite direction to the poling field. This can be seen from the increased LEO value when the d.c. poling voltage was turned off at room temperature. The LEO coefficient resulting from negative thermal poling is larger than that from positive thermal poling for the type of fibre used.

The above results support the space charge electrical field model and exclude the dipole/bond orientation model for the induced electro-optic effect in silica fibre. It is found that, in general, thermal poling of silica fibres consists of two processes: an initial process of building up a shielding field and a subsequent process of establishing an ionization field. Both the shielding field and the ionization field can be frozen-in at room temperature and be used to achieve residual LEO effects. The larger LEO effect obtained from negative thermal poling shows that negative thermal poling is more efficient than positive thermal poling for the present fibre.

6.5 Charge Dynamics and Distributions in Thermally Poled Silica Fibres

In the above section, it is proposed that, in addition to the external poling field, $\vec{E}_{poling}$, there are two electrical fields during thermal poling of silica fibre: the shielding field, $\vec{E}_{shielding}$, and the ionization field, $\vec{E}_{ionization}$. The former is due to migration of positive charges from the anode to the cathode, and exists between the migrated positive charge region and the negative charge depletion region. The latter is due to ionization between the negative charge depletion region and the anode, and exists between the ionized positive charge region and the negative charge depletion region. $\vec{E}_{poling}$ and $\vec{E}_{ionization}$ are in the same direction. But $\vec{E}_{shielding}$ is opposite to $\vec{E}_{poling}$ and $\vec{E}_{ionization}$. Both $\vec{E}_{shielding}$ and $\vec{E}_{ionization}$ are frozen-in at room temperature and lead to LEO effects in silica fibre. This section describes movement of these

charged regions and competition of their associated electrical fields during negative thermal poling of the aluminum co-doped germanosilicate fibre.

Three identical fibre devices were used in the *in situ* negative thermal poling experiments. One device denoted Device A was negatively poled at -3.5 kV and at 250 °C for ~ 1 hour. Another device denoted Device B was negatively poled at -3.5 kV and at 280 °C for ~ 3 hours. At the end of poling of Devices A and B, the heater was taken away from the fibre devices with the d.c. poling voltage on. The thermal poling induced residual LEO coefficients, $r_{residual}$, of the devices were then measured with the d.c. poling voltage turned off at room temperature. The last device denoted Device C has been continuously poled at -3.5 kV and at 280 °C for ~ 5 hours until arcing, which consequently destroyed the device.

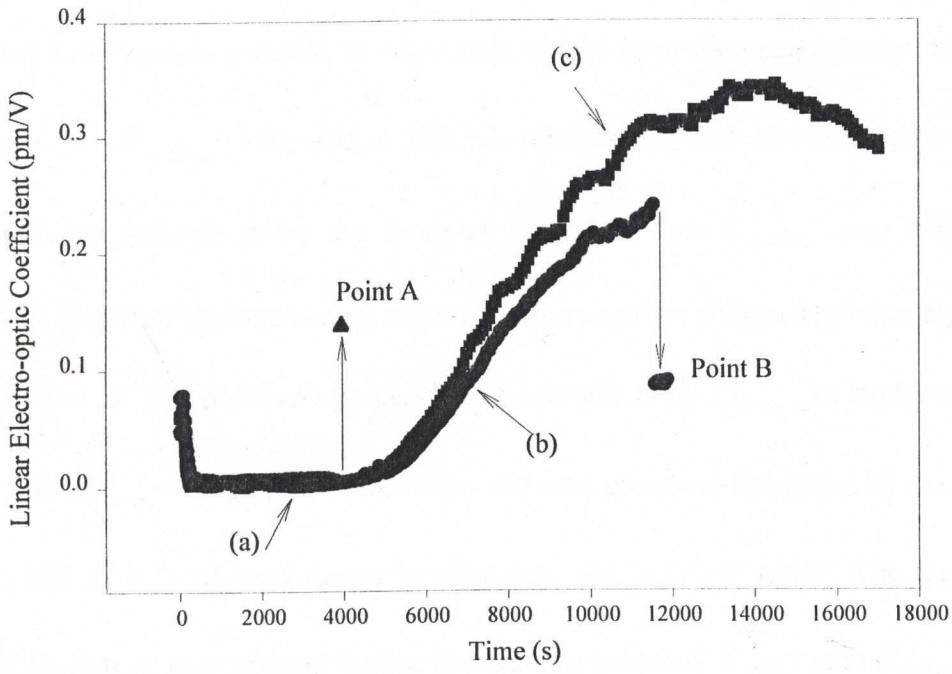

Fig. 6.7 (a) The in situ poling of Device A is represented by triangles. The poling of Device A was stopped at Point A.

(b) The in situ poling of Device B is represented by circles. The poling of Device B was stopped at Point B.

(c) The in situ poling of Device C is represented by squares.

The time evolution of the total LEO coefficient, r_{total} (the sum of the external poling field induced LEO coefficient and $r_{residual}$), in negative thermal poling of Devices A, B and C are shown in Fig. 6.7 (a), (b) and (c), respectively. It is clearly shown that all these curves demonstrate similar features. At the beginning of poling, the initial LEO coefficient of each device is due solely to the action of $\vec{E}_{poling}$ on the intrinsic third

order nonlinearity $\chi^{(3)}$ of the glass fibre. Within 1 to 2 minutes of thermal poling, r_{total} of each device was reduced to zero. This results from the establishment of the shielding field, $\vec{E}_{shielding}$. At above 200 °C, positive charges became active and migrated to the cathode under the force of $\vec{E}_{poling}$ so that $\vec{E}_{shielding}$ was built up between the migrated positive charge region and the negative charge depletion region. The migration of the positive charges has continued until $\vec{E}_{poling}$ is balanced by $\vec{E}_{shielding}$, i.e. $\vec{E}_{poling} = -\vec{E}_{shielding}$. At this time, the total electrical field seen by the core was zero and so r_{total} of each device became zero, i.e. $r_{total} = 0$ pm/V. The thermal poling of Device A was stopped during the balance between $\vec{E}_{poling}$ and $\vec{E}_{shielding}$. It can be clearly seen in Fig. 6.7 (a) that $r_{residual}$ of the device is non-zero, as indicated at Point A in Fig. 6.7, when $\vec{E}_{poling}$ was removed at room temperature. This LEO value at Point A is the thermal poling induced residual LEO coefficient, $r_{residual}$. It results from the frozen-in shielding field $\vec{E}_{shielding}$ and is due to the action of $\vec{E}_{shielding}$ on the intrinsic $\chi^{(3)}$ of the glass fibre, i.e. $r_{residual} \propto 3\chi^{(3)}\vec{E}_{shielding}$. The charge distributions at Point A in the thermally poled fibre are shown in Fig. 6.6. Note that ionization near to the anode is also shown and this is discussed later in this section.

On the other hand, thermal poling of Devices B and C was continued. An interesting feature of their thermal poling is shown in Fig. 6.7 (b) and (c), and r_{total} of each device began to increase from zero after ~80 minutes thermal poling. This suggests that the

balance between $\vec{E}_{poling}$ and $\vec{E}_{shielding}$ was broken. Section 6.4 pointed out that ionization would take place between the negative charge depletion region and the anode after positive charges migrated to the cathode. The ionization process led to a positive charge region being formed between the negative charge depletion region and the anode. The ionization field, $\vec{E}_{ionization}$, between the ionized positive charge region and the negative charge depletion region is in the same direction as $\vec{E}_{poling}$. The ionization process has been continuing during $r_{total} = 0$ pm/V. This caused the negative charge depletion region and the ionized positive charge region to move further and further from the anode towards the cathode. When these regions overlapped with the core, the balance between $\vec{E}_{poling}$ and $\vec{E}_{shielding}$ was then broken by $\vec{E}_{ionization}$. The total LEO coefficient of the devices became non-zero, i.e. $r_{total} \neq 0$ pm/V. With the ionization process continuing, the core was overlapped better and better with the negative charge depletion region and the ionized positive charge region. Consequently r_{total} increased after passing through zero. The thermal poling of Device B was stopped before its r_{total} saturated. Similar to the positive thermal poling case in Section 6.4, r_{total} of the device dropped down to Point B in Fig. 6.7 when $\vec{E}_{poling}$ was removed at room temperature. The value at Point B is the residual LEO coefficient, $r_{residual}$. It is due mainly to the frozen-in ionization field, $\vec{E}_{ionization}$. The charge distributions at Point B in the thermally poled fibre are illustrated in Fig. 6.8.

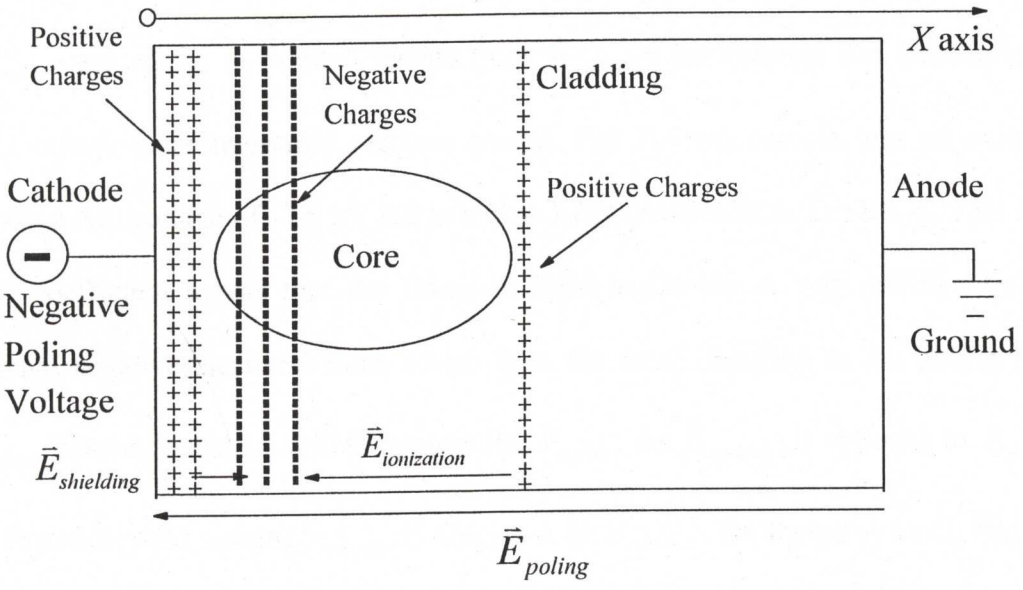

Fig. 6.8 Proposed charge distributions at Point B for Device B.

The features of the prolonged negative thermal poling of Device C are very similar to those reported in Chapter 4 and Refs. 6.17 and 6.18. As for Device C, r_{total} increases until it reaches a peak value. Afterward, r_{total} began to decrease. r_{total} reached the maximum value probably because the core mode was optimally overlapped with the negative charge depletion region and the ionized positive charge region. r_{total} began decreasing probably because the two regions moved away from the core mode. No residual LEO coefficient of the device was measured because of arcing in the fibre, which destroyed the device. It is interesting that arcing tends to take place after r_{total} reaches its maximum value, and is presumably linked with the near complete penetration of the ionization region in the device.

To examine both the residual LEO coefficient, $r_{residual}$, at Point A results from $\vec{E}_{shielding}$ and $r_{residual}$ at Point B results from $\vec{E}_{ionization}$, the external d.c. field induced LEO effects were measured at these points. Fig. 6.9 (a) reveals that an external negative d.c. voltage of -3.5 kV led to a zero LEO coefficient in Device A. This zero LEO coefficient means that the frozen-in field in Device A was nullified by the external negative electrical field, which is in the same direction as the poling field $\vec{E}_{poling}$. So the frozen-in field is opposite to $\vec{E}_{poling}$. As $\vec{E}_{shielding}$ is opposite to $\vec{E}_{poling}$, the frozen-in field causing $r_{residual}$ in Device A is $\vec{E}_{shielding}$. On the other hand, Fig. 6.9 (b) shows that an external positive d.c. voltage of +2.5 kV resulted in a zero LEO coefficient in Device B. It means that the frozen-in field in Device B was balanced by the external positive electrical field, which is opposite to $\vec{E}_{poling}$. So the frozen-in field is in the same direction as $\vec{E}_{poling}$. Since $\vec{E}_{ionization}$ has the same direction as $\vec{E}_{poling}$, the frozen-in field causing $r_{residual}$ in Device B is mainly $\vec{E}_{ionization}$. Note that the slope of the solid curves in Figs. 6.9 (a) and (b) after poling is ~2 times larger than that of the dashed curves before poling. As analyzed in Section 6.3, the slope of these curves is proportional to the third order nonlinearity, $\chi^{(3)}$, of the fibre core. So the $\chi^{(3)}$ of the fibre core of both Devices A and B is increased by a factor of ~2 after thermal poling.

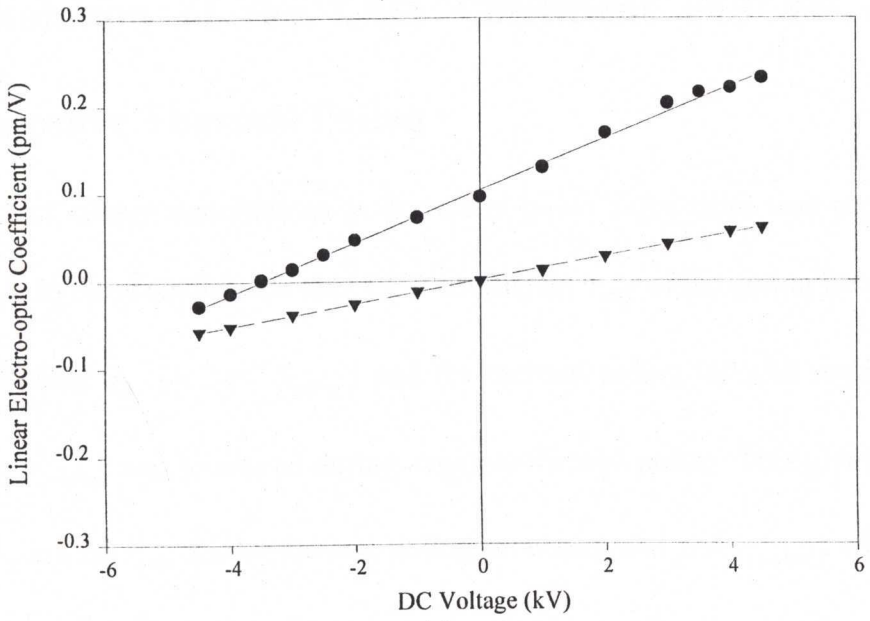

(a)

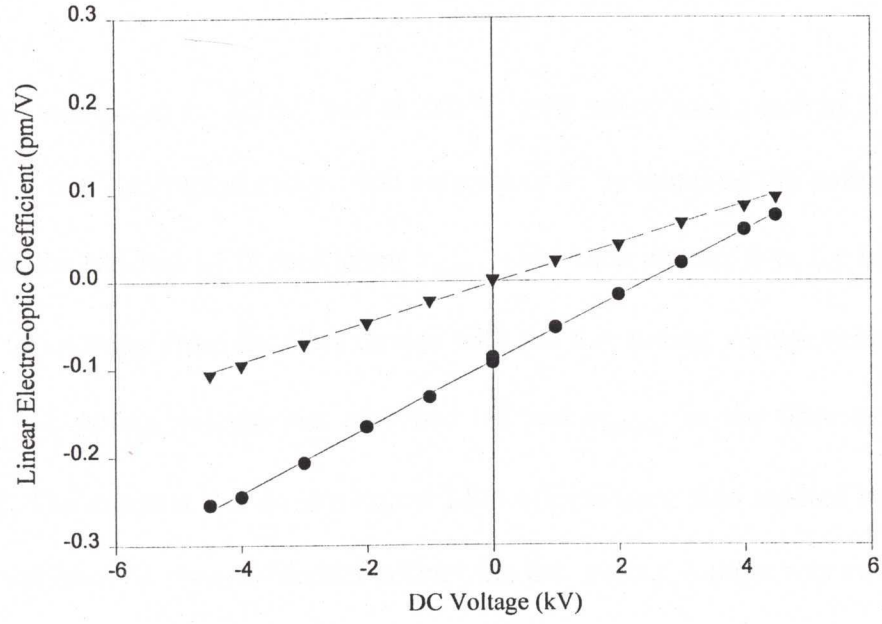

(b)

Fig. 6.9 (a) The external d.c. field induced LEO effects in Device A;

(b) The external d.c. field induced LEO effects in Device B.

6.6 Evolution of the LEO Coefficient and $\chi^{(3)}$ during Negative Thermal Poling

Movement of charge distributions in thermally poled silica fibre was proposed in Section 6.5. In those studies, the total LEO coefficient r_{total} of the poling field induced LEO coefficient r_{dc} ($\propto 3\chi^{(3)}\vec{E}_{poling}$) and the thermal poling induced residual LEO coefficient $r_{residual}$ was measured during negative thermal poling. This gives only the time evolution of r_{total} in the thermal poling processes and not $r_{residual}$, which is of great interest. In this section, both dynamic evolutions of $r_{residual}$ and r_{total} during prolonged negative thermal poling were studied.

One device was poled at -3.5 kV and at 280 °C until arcing took place in the device. However, it was interrupted every 1000 seconds or so by stopping the poling process to measure the residual LEO coefficient $r_{residual}$. For each interruption, the heater was instantly taken away from the fibre device with the d.c. poling voltage remained on. Then the d.c. poling voltage was switched off and $r_{residual}$ in the fibre device was measured. The external d.c. field induced LEO effects were also studied at some of the interruptions. To resume thermal poling, the d.c. poling voltage was switched on again and the heater was re-attached to the device. The heater's temperature was maintained at 280 °C during the entire poling experiment using a temperature controller.

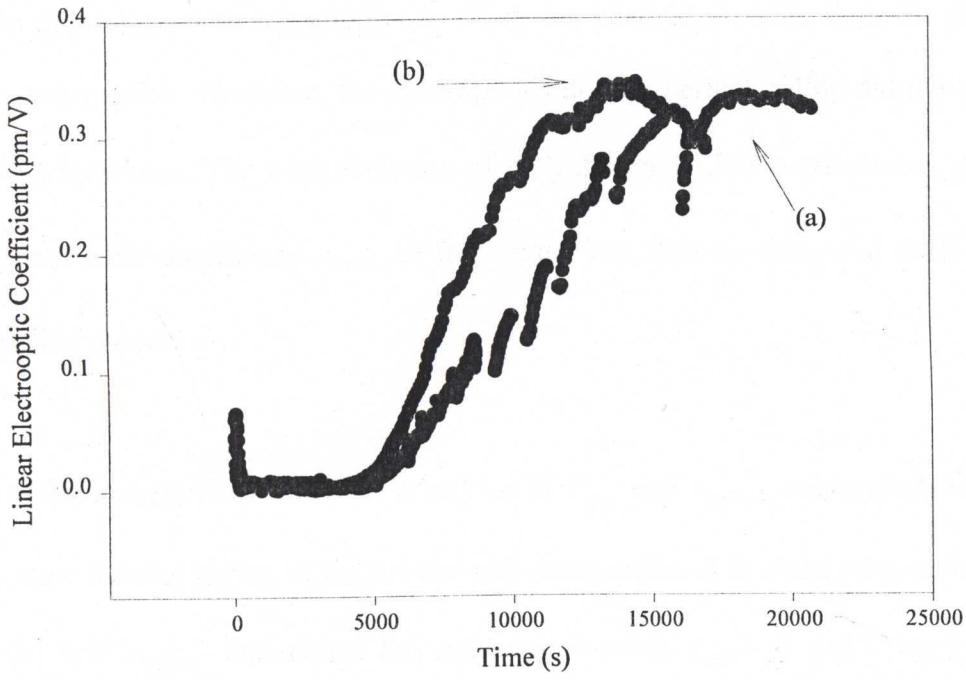

Fig. 6.10 (a) One device was poled at -3.5 kV and 280 °C with disturbance;

(b) Device C was poled at -3.5 kV and 280 °C without disturbance.

The *in situ* poling response of the device is shown in Fig. 6.10 (a), and the *in situ* poling responses of Device C in Section 6.5 is also shown in Fig. 6. 10 (b). In general, the poling response with interruption exhibits similar features as that of Device C, which was not interrupted during poling. Firstly, r_{total} of both devices decreased to zero after 1 to 2 minutes of thermal poling. Secondly, r_{total} of both devices was zero for ~ 80 minute of poling. Thirdly, their LEO coefficients r_{total} began to increase from zero after ~80 minutes until r_{total} reached the same maximum value. Next, further poling reduced r_{total}. Finally, arcing took place in both devices after r_{total}

reached the maximum. The only difference between them is that it took a little longer time for the device with interruption to reach the peak LEO value than the device without interruption. Therefore, the interruptions during thermal poling did not affect the poling behaviors. The time evolution of both the total LEO coefficient r_{total} and the residual LEO coefficient $r_{residual}$ of the device can then be measured during the entire poling process.

Fig. 6.11 (a) and (b) show the time evolution of r_{total} and $r_{residual}$ respectively during the negative thermal poling of the device with interruption. It is clearly shown in Fig. 6.11 (b) that $r_{residual}$ maintained the same value when $r_{total} = 0$ pm/V up to ~80 minutes poling time. This indicates that the total electrical field seen by the core was zero and $\vec{E}_{poling}$ is nullified by $\vec{E}_{shielding}$, i.e. $\vec{E}_{poling} = -\vec{E}_{shielding}$. The residual LEO coefficient, $r_{residual}$, was therefore due to $\vec{E}_{shielding}$, i.e. $r_{residual} \propto 3\chi^{(3)}\vec{E}_{shielding}$. After ~80 minute poling, as shown in Fig. 6.11, $r_{residual}$ decreased from the maximum value to zero and then became negative while r_{total} increased from zero. This feature is due to movement of the ionization field, $\vec{E}_{ionization}$, into the core. The reduction in $r_{residual}$ was caused by $\vec{E}_{ionization}$, which weakened $\vec{E}_{shielding}$. Thus, r_{total} became non-zero as $\vec{E}_{ionization}$ broke the electrical field balance condition between $\vec{E}_{poling}$ and $\vec{E}_{shielding}$. With $\vec{E}_{ionization}$ shifting into the core further and further, $r_{residual}$ decreased to zero and became negative while r_{total} kept on increasing until saturation. When $\vec{E}_{ionization}$ was balanced by $\vec{E}_{shielding}$ as seen by the core, $r_{residual} = 0$ pm/V. When $\vec{E}_{ionization}$ was seen

more than $\vec{E}_{shielding}$ by the core, $r_{residual}$ became negative. An interesting feature in Fig. 6.11 (b) is that $r_{residual}$ decreased linearly as a function of time. This means the competition between $\vec{E}_{ionization}$ and $\vec{E}_{shielding}$ is a linear process.

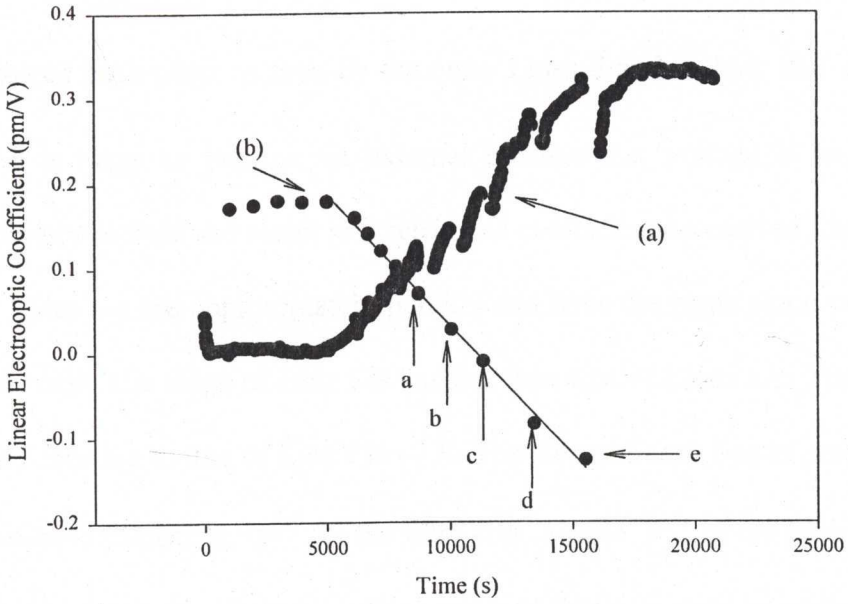

Fig. 6.11 (a) Time evolution of r_{total} of the device poled at-3.5 kV and 280 °C;

(b) Time evolution of $r_{residual}$ the device poled at-3.5 kV and 280 °C. The solid line is the fit to the decreasing part of $r_{residual}$.

The external d.c. field induced LEO effects at Points a-e of Fig. 6.11 (b) were studied and shown in Fig. 6.12. The lines labeled from a to e in Fig. 6.12 refer to Points a-e in Fig. 6.11 (b), respectively. The external d.c. field induced LEO effect before poling is

also shown in Fig. 6.12 and is denoted as Line f. It can be clearly seen from Lines a and b that $r_{residual}$ at Points a and b is positive because an external negative d.c. voltage is needed to balance the frozen-in field and result in a zero LEO coefficient on each of Lines a and b. Line c shows that $r_{residual} = 0$ pm/V at Point c and no external d.c. voltage is needed to balance the frozen-in field. This means that $\vec{E}_{ionization}$ and $\vec{E}_{shielding}$ balanced each other as seen by the core. Lines d and e show that $r_{residual}$ at Points d to e is negative because an external positive d.c. voltage is required to balance the frozen-in field and result in a zero LEO coefficient on each of Lines d and e. Note that Lines a-e are approximately parallel and have the same slope within the experimental error. The slope of Line f is smaller than that of Lines a-e. The ratio of the slopes of Lines a-e to that of Line f is ~1.8. The slope of each line is proportional to the third order nonlinearity, $\chi^{(3)}$, of the fibre core. Hence $\chi^{(3)}$ of the fibre core has been increased by ~1.8 after thermal poling, and it is fairly constant regardless of the sign and value of $r_{residual}$ in the region measured.

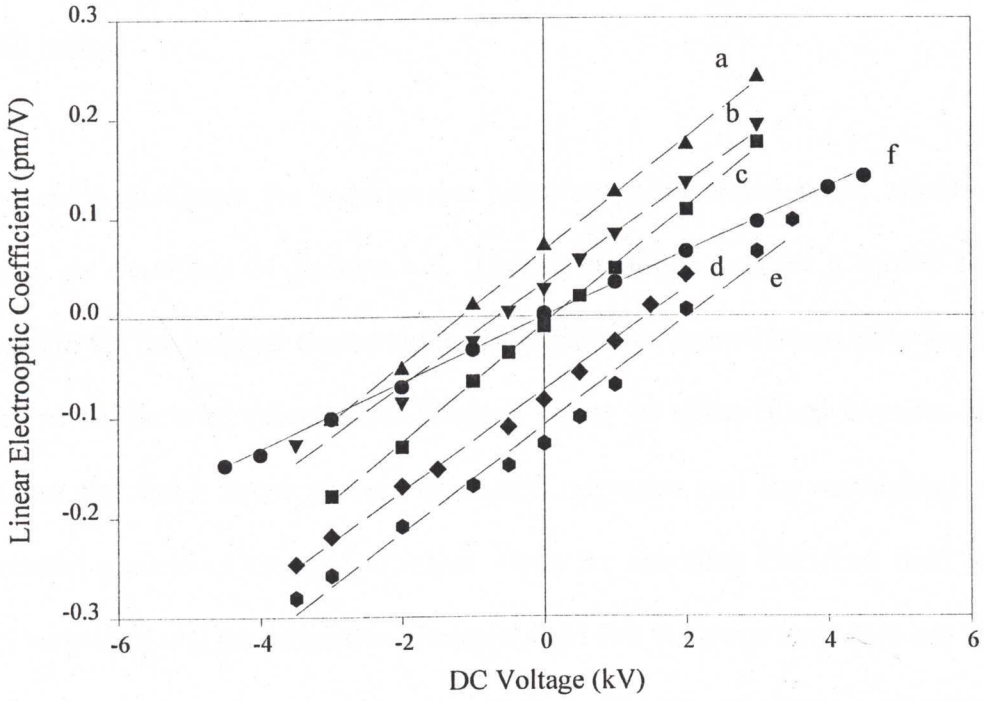

Fig. 6.12 The external d.c. field induced LEO effects at Points a-e of Fig. 6.11 (b) are shown by Lines a-e, respectively. The external d.c. field induced LEO effect before poling is shown by Line f.

6.7 Conclusion

In Section 6.2, the frozen-in field in thermally poled fibre is experimentally verified to exist. It is the first report of a method to measure both the magnitude and the direction of the frozen-in field in thermally poled silica fibre. Section 6.3 shows that the value of $\chi^{(3)}$ of silica fibre can be obtained using the same measurement technique. The technique is suitable for measuring the third-order nonlinearity of isotropic optical

materials. It is found that $\chi^{(3)}$ of the fibre core has increased by a factor of ~ 2 after thermal poling.

The dynamic processes for positive and negative poling voltages are significantly different, as described in Section 6.4. The observations support a model for the mechanism for the induced electro-optic effect based on space charge electrical fields instead of dipole/bond orientation. Thermal poling of silica fibres consists of two processes: the faster linear process of charge migration and the subsequent single exponential process of charge ionization. Both the shielding electrical field due to charge migration and the ionization electrical field due to charge ionization are able to be frozen-in at room temperature and lead to the residual linear electro-optic effect.

Section 6.5 describes a series of negative thermal poling experiments of germanosilicate fibre. These experiments suggest the dynamic movement of charge distributions in thermally poled silica fibre. It is also found that $\chi^{(3)}$ of the fibre core is around 1.8 times of that before poling, regardless of the sign and value of $r_{residual}$.

In Section 6.6, both the residual LEO coefficients, $r_{residual}$, and the total LEO coefficients, r_{total}, were measured during a prolonged *in situ* negative thermal poling of germanosilicate fibre. When $r_{total} = 0$ pm/V, $r_{residual}$ maintained the same value, which is proportional to $3\chi^{(3)}\vec{E}_{shielding}$. When r_{total} increased from zero, $r_{residual}$ depends on the degree of the competition between $\vec{E}_{shielding}$ and $\vec{E}_{ionization}$. The time

evolution of $r_{residual}$ shows that the competition of the shielding field and the ionization field is a linear process. During the thermal poling, the third order nonlinearity of the poled fibre is fairly constant, which is still larger than that of the fibre before poling by a factor of ~1.8.

The present results support the theory that thermal poling of silica fibre is due to the space charge effects and the frozen-in fields in thermally poled silica fibre. The results also indicate that $\chi^{(3)}$ of silica fibre has been increased by thermal poling.

6.8 References

[6.1] P. G. Kazansky, P. St. J. Russell, and H. Takebe, "Glass fiber poling and applications," Journal of Lightwave Technology, vol. 15, pp. 1484-1493, 1997.

[6.2] P. G. Kazansky and P. St. J. Russell, "Thermally poled glass: frozen-in electric field or oriented dipoles?" Opt. Comm., vol. 110, pp. 611-614, 1994.

[6.3] W. Xu, D. Wong, S. Fleming, M. Janos, and K. M. Lo, "Direct measurement of frozen-in field in thermally poled fibres," Proceedings of the 23rd Australian Conference of Optical Fibre Technology (ACOFT'98), pp. 201-204, Melbourne Australia, July 1998.

[6.4] A. L. Calvez, E. Freysz, A. Ducasse, "Experimental study of the origin of the second-order nonlinearities induced in thermally poled fused glasses," Opt. Lett., vol. 22, pp. 1547-1549, 1997.

[6.5] R. A. Myers, N. Mukherjee, and S. R. J. Brueck, "Large second-order nonlinearity in poled fused silica," Opt. Lett., vol. 16, pp. 1732-1734, 1991.

[6.6] N. Mukherjee, R. A. Myers, and S. R. J. Brueck, "Dynamics of second-harmonic generation in fused silica," J. Opt. Soc. Am. B, vol. 11, pp. 665-669, 1994.

[6.7] P.G. Kazansky and P. St. J. Russell, "Thermally poled glass: frozen-in electric field or oriented dipoles ?", Optics Communications, Vol.110, pp.611-614, 1994.

[6.8] N. Wada, K. Morinaga, H. Takebe, V. Pruneri and P. Kazansky, "Effect of minority species on thermal poling of fused silica glasses", Proceedings of Bragg gratings - Photosensitivity and poling in Glass Fibres and Waveguides: Applications and Fundamentals, paper BTuC3-1, pp.296-298, Virginia, October, 1997.

[6.9] T. G. Alley, S.R. Brueck and R.A. Myers, "An ion exchange model for extended-duration thermal poling of bulk fused silica", Proceedings of Bragg gratings - Photosensitivity and poling in Glass Fibres and Waveguides: Applications and Fundamentals, paper BTuC2-1, pp.296-298, Virginia, October, 1997.

[6.10] P. G. Kazansky, R. A. Smith, P. St. J. Russell, G. M. Yang, and G. M. Sessler, "Thermally poled silica glass: Laser-induced pressure pulse probe of charge-distribution," Appl. Phys. Lett., vol. 68, pp. 269-271, 1996.

[6.11] W. Margulis and F. Laurell, "Interferometric study of poled glass under etching," Opt. Lett., vol. 21, pp. 1786-1788, 1996.

[6.12] T. G. Alley and S. R. J. Brueck, "Visualization of the nonlinear optical space-charge region of bulk thermally poled fused-silica glass," Opt. Lett., vol. 23, pp. 1170-1172, 1998.

[6.13] D. Statman and J. A. Georges III, "Charge dynamics and poling in glass waveguides," J. Appl. Phys., vol. 80, pp. 654-661, 1996.

[6.14] R. Adair, L. L. Chase, and S. A. Payne, "Nonlinear refractive-index measurements of glasses using three-wave frequency mixing," J. Opt. Soc. Am. B **4**, 875 (1987).

[6.15] S. Aramaki, Y. Okamoto, and T. Murayama, "Cross-Linked Poled Polymer: Poling and Thermal Stability," Jpn. J. Appl. Phys., vol. 33, pp. 5759-5765, 1994.

[6.16] H. L. Hampsch and J. M. Torkelson, "Second harmonic generation in corona poled, doped polymer films as a function of corona processing," J. Appl. Phys., vol. 67, pp. 1037-1041, 1990.

[6.17] X. C. Long, R.A. Myers and S. R. J. Brueck, "A poled electrooptic fiber", IEEE Photon. Tech. Lett., vol.8, pp. 227-229, 1996.

[6.18] H. Takebe, P.G. Kazansky, P. St. J. Russell and K. Morinaga, "Effect of poling conditions on second-harmonic generation in fused silica", Optics Letters, Vol.21, No.7, pp.468-470, 1996.

Chapter 7 Electro-optic Modulation of Bragg Grating in Thermally Poled Fibres

7.1 Introduction

Fibre Bragg gratings are widely used as key components for dense wavelength-division-multiplexing (DWDM) networks and systems [7.1, 7.2]. Tunable Bragg gratings are very promising for the rapidly growing DWDM systems. For example, Iocco *et al.* realized a fast tunable optical filter based on fibre Bragg grating compression [7.3]. A setting time of <2 ms over a 15 nm tuning range has been achieved. Feng *et al.* demonstrated a tunable nonlinearly-chirped fiber Bragg grating and used it as a dispersion compensator with a voltage-controlled dispersion [7.4]. With ~ 1 kV applied, the reflected grating spectrum is shifted by ~1.5 nm, and wavelength shift with voltage is linear. The dispersion varies nonlinearly and smoothly from 300 – 1000 ps/nm.

Tuning of fibre Bragg gratings is normally base on the sensitivity of the grating wavelength to thermal and strain changes [7.5, 7.6]. However, the tuning speed based on these methods is limited to a few mini-seconds [7.3, 7.4]. The facility of using such a fibre device is normally complicated in order to tune the Bragg grating. For instance, in Ref. 7.3, a piezoelectric actuator was driven by an HV amplifier (100 W) to compress the fibre longitudinally. Metallic ferrules held the fibre in place and

guided it. The ferrules were fixed on a mechanical system, which permitted transmission of the compressive strain from the piezoelectric actuator to the fibre. The Bragg grating had to be exactly positioned within the compressed zone of 8 mm in order to stress it homogeneously.

Therefore, it will be ideal if the silica fibre has a linear electro-optic coefficient and the fibre Bragg grating can then be tuned based on the linear electro-optic effect. Fujiwara, *et al.* first demonstrated an electrically tunable Bragg grating based on the linear electro-optic effect [7.7, 7.8]. Using a phase mask, a Bragg grating at ~1530 nm was written to the fibre whilst a high voltage was applied to the fibre. After UV periodic poling of the fibre device, the Bragg grating could be tuned ~0.01 nm for 1 V/μm. The corresponding intensity modulation was 10 dB for 300 V applied voltage.

In this chapter, a different approach to achieving an electrically tunable fibre Bragg grating was introduced. The Bragg grating was firstly written into a twin-hole fibre device. The device was then thermally poled so as to achieve a linear electro-optic effect. This results in an electrically tunable fibre Bragg grating. In Section 7.2, basic theory about the electrically tunable Bragg grating is introduced. Section 7.3 describes the fabrication of the tunable Bragg grating and the experimental setup of electrically tuning the Bragg grating. In Section 7.4, the grating is electrically tuned during and after thermal poling. A wavelength-specific intensity modulator is then achieved by varying the reflection of the Bragg grating. Its performance is addressed in this chapter.

W. Xu, "Thermally Poled Fibre Devices," Ph.D. Thesis, University of Sydney, Australia, March, 1999

7.2 Theory of Electrically Tunable Bragg Grating

The Bragg wavelength λ_B of an in-fibre grating can be expressed by the equation

$$\lambda_B = 2\bar{n}\Lambda, \tag{7.1}$$

where $\bar{n}$ is the effective refractive index of the guided mode and Λ is the period of the Bragg grating [7.1].

A poled fibre has an electro-optic coefficient r. When a voltage V is applied to the fibre, the change of the refractive index $\delta\bar{n}$ [7.9] is described by

$$\delta\bar{n} = \frac{1}{2} r\bar{n}^3 \frac{V}{d_{eff}}, \tag{7.2}$$

where d_{eff} is the effective distance between two electrodes.

The corresponding change in the Bragg wavelength $\delta\lambda_B$ can be obtained from

$$\frac{\delta\lambda_B}{\lambda_B} = \frac{\delta\bar{n}}{\bar{n}}. \tag{7.3}$$

Substituting Eq. 7.2 into Eq. 7.3, $\delta\lambda_B$ is given by

$$\delta\lambda_B = \frac{1}{2}\lambda_B r\bar{n}^2 \frac{V}{d_{eff}}. \tag{7.4}$$

Suppose that the electro-optic coefficient r of the fibre is 1.0 pm/V and the average refractive index $\bar{n}$ of the core is 1.46. When a voltage of $V = 1000$ V is applied to a fibre with an effective distance between the two electrodes, $d_{eff} = 10$ μm, the change

in Bragg wavelength, $\delta\lambda_B$, is 0.165 nm for a grating with Bragg wavelength $\lambda_B = 1550$ nm using Eq. 7.4.

7.3 Experiment

A 2 cm long fibre Bragg grating at ~1538 nm was generated by exposing a boron-codoped germanosilicate twin-hole fibre device to a 193 nm pulsed Excimer laser through a phase mask. The fluence per pulse was 80 mJ/cm^2 and the total irradiation dose was 1.2 kJ/ cm^2. After the UV exposure, the Bragg grating was thermally poled at +3 kV and 250 °C for ~ 1 hour in order to induce the linear electro-optic effect into the fibre.

Fig. 7.1 shows the experimental setup for electro-optic modulation of the fibre Bragg grating during and after thermal poling. A tunable laser source around 1550 nm wavelength with 0.001 nm resolution was used in the experiment. The laser beam was launched into the fibre device by butt coupling and was picked up from the device using a lens. Thus the light was collimated and directed into the photo detector. The detector was connected to a digital oscilloscope and a computer, and so the data was captured and stored in the computer.

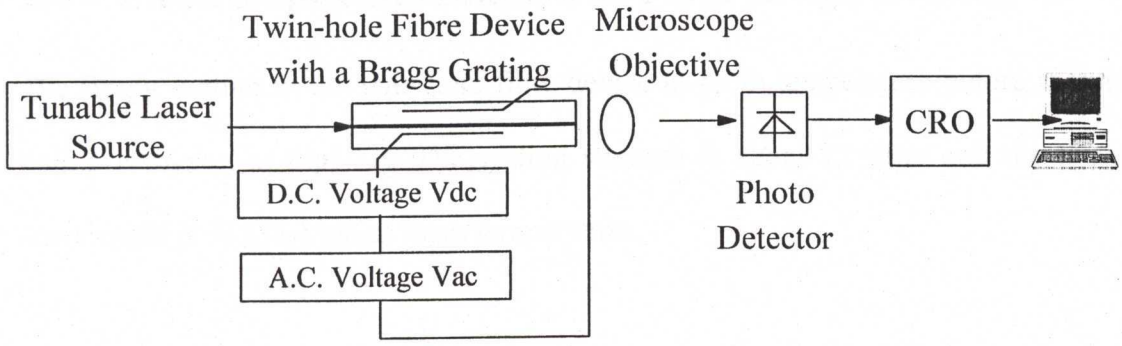

Fig. 7.1 Experimental setup for electro-optic modulation of a fibre Bragg grating

An a.c. testing voltage, V_{ac}, with 8.5 kHz was superimposed onto the d.c. poling voltage, V_{dc}. The sum of them was then applied to the device. During thermal poling of the Bragg grating, there were two linear electro-optic effects in the fibre. One was due to the action of the d.c. poling field on the intrinsic third order nonlinearity of the silica fibre [7.10]. The other was the thermal poling induced linear electro-optic effect. When V_{ac} was applied to the grating, the grating spectrum was tuned according to Eq. 7.4. The reflectance of the grating at a specific wavelength was then changed with V_{ac}. If a laser beam at that wavelength was used, a wavelength-specific intensity modulator could be realized.

The superimposition of V_{ac} onto V_{dc} makes it possible to electrically tune the Bragg grating during thermal poling. The growth of the linear electro-optic effect in the fibre can thus be monitored during poling.

7.4 Electro-optic Modulation of Fibre Bragg Grating

The Bragg grating in the twin-hole fibre device at room temperature before thermal poling is shown in Fig. 7.2. The grating strength is about 12 dBm and the Bragg wavelength is ~1538.1 nm at room temperature.

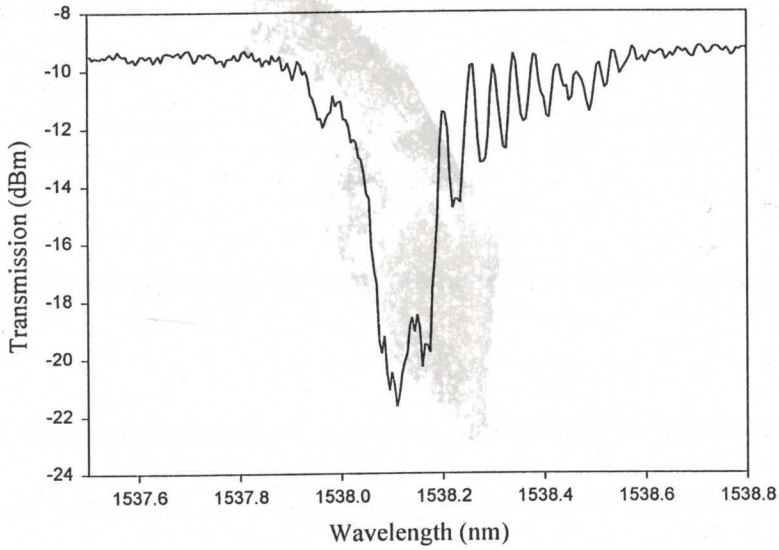

Fig. 7. 2 Bragg grating in the twin-hole fibre at room temperature before poling

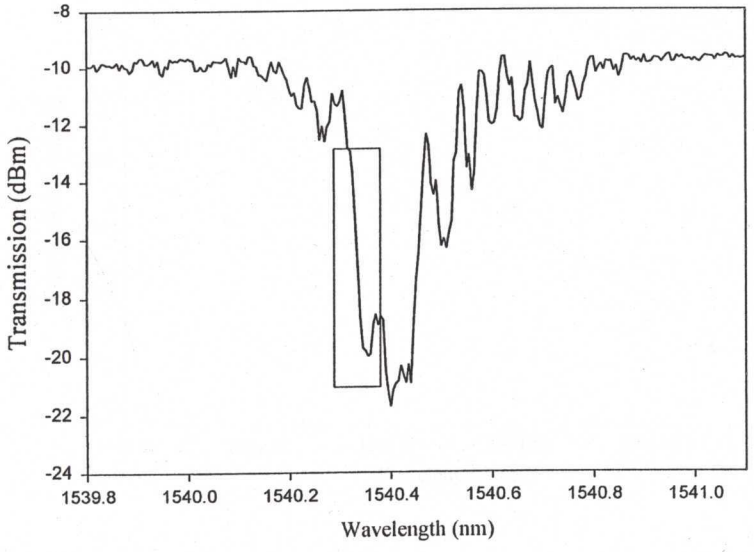

Fig. 7. 3 Bragg grating in the twin-hole fibre at 250 °C during poling

Because the Bragg wavelength of a grating shifts by 0.01 nm due to a change in temperature of 1 degree [7.2, 7.5], the Bragg wavelength of the twin-hole fibre grating was changed to ~1540.4 nm at 250 °C as shown in Fig. 7.3. An a.c. testing voltage, $V_{ac} = 950$ V (peak-to-peak amplitude) at 8.5 kHz was superimposed onto the d.c. poling voltage V_{dc}. The spectrum of the grating was then varied with V_{ac} due to the linear electro-optic effects in the fibre. The tunable laser source was positioned at the wavelength of 1540.32 nm such that it falls on the edge of the grating spectrum at 250°C as indicated in Figs. 7.3 and 7.4. When the grating spectrum was shifted by V_{ac}, the reflectance of the grating at 1540.32 nm was changed correspondingly. So the output power from the fibre device was modulated by the a.c. testing signal, as shown in Fig. 7.5.

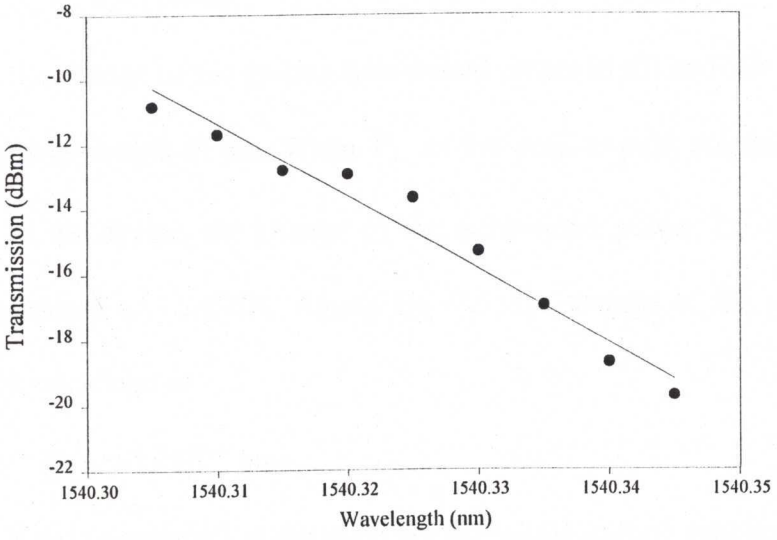

Fig. 7. 4 The spectrum of the grating in the rectangular section of Fig. 7.3

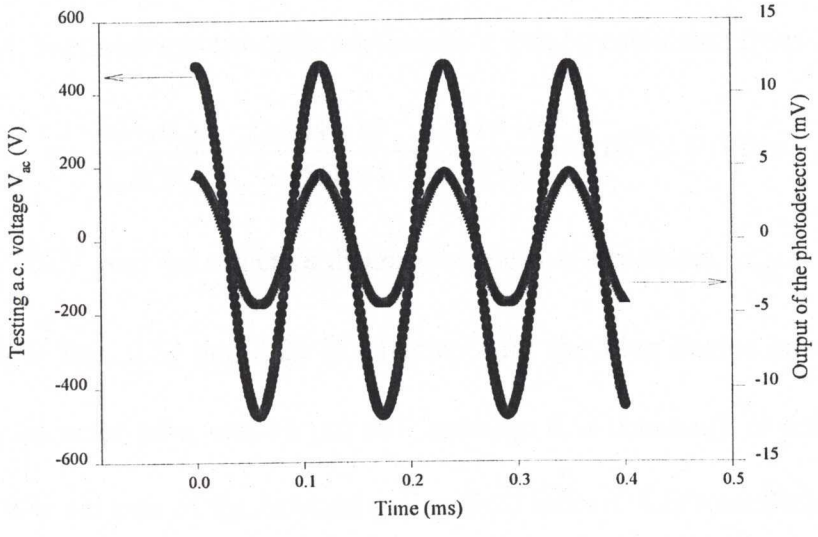

Fig. 7. 5 Electro-optic modulation of a Bragg grating. Solid circles are for the testing input signal V_{ac} and solid triangles are for the output signal from the photodetector.

The slope of the grating spectrum around 1540.32 nm in Fig. 7.4 is -224.5, i.e.

$$\delta w = -224.5\delta\lambda, \tag{7.5}$$

where δw is the change of the grating transmitted power in dB and $\delta\lambda$ is the change of the grating wavelength in nm. When V_{ac} of the peak-to-peak amplitude of 950 V was applied to the device, the change of the transmitted power, i.e. the extinction ratio, was measured as ~2.1 dB. Using Eq. 7.5, the change of the wavelength at 1540.32 nm is calculated as

$$\delta\lambda = 9.4\times10^{-3} \text{ nm}. \tag{7.6}$$

The change of the wavelength is the same for the whole grating spectrum, and hence the change of the wavelength at the Bragg wavelength equals that at 1540.32 nm, i.e.

$$\delta\lambda_B = \delta\lambda = 9.4\times10^{-3} \text{ nm}. \tag{7.7}$$

Using Eq. 7.4, the linear electro-optic coefficient r can be calculated from $\delta\lambda_B$ as

$$r = \frac{2\delta\lambda_B d_{eff}}{\lambda_B \bar{n}^2 V_{ac}} = \frac{2\times9.4\times10^{-3}\times101\times10^{-6}}{1550\times1.46^2\times950}\times10^{12} = 0.6 \text{ pm/V}, \tag{7.8}$$

where $V_{ac} = 950$ V and the effective distance of the two electrodes, $d_{eff} = 101$ μm, is calculated from Eqs. 2.22 and 2.23 in Chapter 2 for the fibre device having 90 μm hole, 50 μm diameter wire, and 16 μm hole spacing. It is necessary to point out that $r = 0.6$ pm/V is the sum of the external poling field induced LEO coefficient and the thermal poling induced residual LEO coefficient.

After thermal poling for ~1 hour, the fibre device was allowed to cool down to room temperature with the d.c. poling voltage remained on. When the device reached room

temperature, the d.c. poling voltage was switched off and the spectrum of the grating after poling was measured again as shown in Fig. 7.6. The Bragg wavelength of the grating became ~1538.5 nm at room temperature and it is slightly different from the Bragg wavelength of the grating before poling. The wavelength of the laser light was locked at 1538.40 nm, which is at the edge of transmission dip of the grating. The a.c. testing voltage V_{ac} of the peak-to-peak amplitude of 950 V was applied to the device to modulate the grating again. The change of the transmitted power, i.e. the extinction ratio, was measured as ~0.7 dB. Using Eqs 7.4 and 7.5, the residual linear electro-optic coefficient of the device (with the d.c. poling voltage off) was calculated as $r = 0.2$ pm/V.

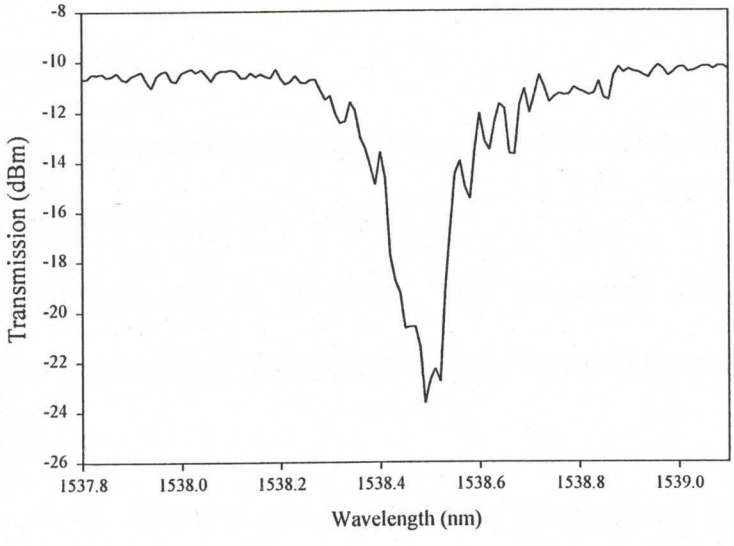

Fig. 7. 6 Bragg grating in the twin-hole fibre at room temperature after poling.

7.5 Conclusion

In addition to UV periodic poling, a new method – thermal poling of Bragg gratings—was demonstrated to realize electrically tunable Bragg gratings. A single fibre intensity modulator was demonstrated using the electrical tuning of the grating although the modulation efficiency needs to be improved.

Modulation of a Bragg grating during thermal poling can be employed to monitor the time evolution of the linear electro-optic effect in thermal poling. In addition to the MZI technique described in Chapter 2, this could be another way to make *in situ* measurements in thermal poling. Moreover, based on the external d.c. field induced LEO effect, the grating can also be tuned.

7.6 References

[7.1] R. Kashyap, "Photosensitive Optical Fibres: Devices and Applications," Optical Fiber Technology, vol. 1, pp. 17-34, 1994.

[7.2] R. J. Campbell and R. Kashyap, "The properties and applications of photosensitive germanosilicate fibre," International Journal of Optoelectronics, vol. 9, pp. 33-57, 1994.

[7.3] A. Iocco, H. G. Limberger, and R. P. Salathé, "Bragg grating fast tunable filter," Electron. Lett., vol. 33, pp. 2147-2148, 1997.

[7.4] K.-M. Feng, V. Grubsky, D. S. Starodubov, J.-X. Cai, A. E. Willner, and J. Feinberg, "Tunable nonlinearly-chirped fiber Bragg grating for use as a dispersion

compensator with a voltage-controlled dispersion," OFC'98, TuM3, pp. 72-74, San Jose, USA, 1998.

[7.5] C. Meltz, "Overview of fibre grating-based sensors," Proceedings of SPIE, vol. 2838, pp. 1-21, 1996.

[7.6] G. A. Ball and W. W. Morey, "Compression-tuned single-frequency Bragg grating fibre laser," Opt. Lett., vol. 19, pp. 1979-1981, 1994.

[7.7] T. Fujiwara, D. Wong, Y. Zhao, S. Fleming, V. Grishina, and S. Poole, "UV-excited poling and electrically tunable Bragg gratings in a germanosilicate fiber," OFC'95 post-deadline paper PD6, San Diego, USA, 1995.

[7.8] S. Fleming, D. Wong, H.G. Inglis, W. Xu, T. Fujiwara and P. Hill, "Poled fibre devices for electro-optic modulation", Invited paper, Proceedings of SPIE, vol. 2893, pp. 450-460, 1996.

[7.9] B. E. A. Saleh and M. C. Teich, Fundamentals of Photonics, Chap. 18, pp. 698-712, John Wiley & Sons, Inc., 1991.

[7.10] D. Wong, W. Xu, J. Arentoft, and S. Fleming, "Positive and negative thermal poling of germanosilicate fibres," Technical Digest of OFC/IOOC'99 (Thursday, February 25), ThG4, pp. 90-92, San Diego, USA, 1999.

Chapter 8 Conclusions

The key objectives were defined for this thesis: obtaining a usable linear electro-optic effect in silica fibre and understanding of the mechanisms of thermal poling of silica fibre.

Nothing can be done without proper tools. Two sets of Mach-Zehnder interferometers were designed and constructed. These accurate MZI setups are the basis for the thermal poling experiments being carried out in this thesis.

The optimum thermal poling conditions of the boron-codoped germanosilicate fibre were first studied. The residual LEO coefficient induced by thermal poling increases as a ~2.7 power law with the poling voltage for the silica fibre. The optimum poling temperature ranges from ~250 °C to ~300 °C. The residual LEO coefficient initially increases as a single exponential process with the poling time until it reaches a peak value. After saturation, it decreases because of the depletion nonlinear region moving away from the fibre core. The optimum poling conditions also depend on the fibre constituents and the fibre geometry.

To improve the efficiency of optimizing the poling conditions for a certain fibre, the *in situ* thermal poling technique was employed. The advantage of this method is to optimize the poling conditions for any fibre device while it is being poled. The *in situ*

method becomes very convenient compared to the optimizing method where many fibre devices need to be poled and subsequently characterized.

Using the *in situ* thermal poling technique, it was found that the residual LEO coefficient also depends on the rate of change of poling temperature and the poling history of the fibre. A higher rate of change of poling temperature during initial poling results in a higher residual LEO coefficient. Pre-annealing of the fibre decreases the residual LEO coefficient.

The decay lifetime of the residual LEO coefficient of the boron-codoped germanosilicate fibre was studied. In contrast to the single exponential decay of the second-order nonlinearity induced by UV poling in bulk germanosilicate glass, the measured decay of the LEO coefficient has a good fit using a stretched exponential. The rate coefficient of the decay procedure measured at different temperatures was found to follow the Arrhenius relation. Using the Arrhenius analysis to extrapolate the lifetime at room temperature, an average decay rate of the LEO coefficient was estimated to be ~45 days at room temperature. Alternately, ignoring the early part of the decay process, which decays quickly, a more stable component of the process may be extracted with a decay rate of ~260 days. The decay analysis shows that the poled boron-codoped germanosilicate fibre has a short lifetime in the LEO coefficient and better glass constituents need to be investigated.

In the investigation of the mechanism of thermal poling of silica fibre, the effects of the frozen-in fields and the space charge distributions were revealed. An innovative technique was developed to measure both the magnitude and the direction of the frozen-in field. This method can also be used to measure the third order nonlinearity of the fibre core. It is interesting that the third order nonlinearity of the fibre core increases by a factor of ~2 after thermal poling with the poling voltage of 3.5 kV and the poling temperature of 250 °C. The factor depends on the poling conditions and the glass constituents.

Thermal poling of silica fibre basically consists of two processes: the faster linear process of charge migration and the subsequent single exponential process of charge ionization. The positive charges migrate from the anode to the cathode under the force of the poling field at the poling temperature higher than 200 °C. The charge migration leads to a negative charge depletion region near to the anode. The shielding field then exists between the migrated positive charge region and the negative charge depletion region, and has the direction opposite to the poling field. Because there is a strong electrical field between the anode and the negative charge depletion region, charge ionization takes place in this anodic region. The ionization process leads to an ionized positive charge region near to the anode. The ionization field then exists between the ionized positive charge region and the negative charge depletion region, and has the same direction as the poling field. Both the shielding field and the ionization field are frozen-in at room temperature and result in linear electro-optic effects in thermally poled fibres.

It is interesting that charge distributions in thermally poled fibre can move during poling. The negative charge depletion region and the ionized positive charge region move towards the cathode with increasing poling time. Consequently, the fibre core can see either the shielding field, or the ionization field, or both. That is, the optical mode can overlap with either the shielding field, or the ionization field, or both. The residual LEO coefficient decreases as a linear process with the poling time during the competition between the shielding field and the ionization field. The third order nonlinearity of the fibre core is fairly constant during this competition but it is still larger than that of unpoled silica fibre.

Finally, an application of the thermal poling induced LEO coefficient in silica fibre was demonstrated ----- a simple single-fibre intensity modulator. The intensity modulator is based on an electrically tunable Bragg grating. Furthermore, modulation of a Bragg grating during thermal poling could be another way for the *in situ* measurement to monitor evolution of the LEO coefficient.

In short, the linear electro-optic effect induced into silica fibres by thermal poling is due to the space charge effects and the frozen-in fields in poled silica fibres.

Appendix A Numerical Examples on Optical Waveguiding Properties of Twin-hole Fibres

A.1 Introduction

Due to the two holes of a twin-hole fibre, both the cutoff V value of the first higher order mode and the modal field distribution of the fundamental mode in the twin-hole fibres are very different from those in normal fibres without two holes. Using some numerical examples, this appendix provides insights to the effect of the two holes on the cutoff V value and the modal field distribution in the fibres used for poling.

Firstly, the modal field and cutoff wavelength of a twin-hole fibre with a rectangular core are calculated. Secondly, the cutoff value and the cutoff wavelength of twin-hole fibres are calculated while the distance from the anode to the core changes. Next, the evolution of the modal fields of both fundamental mode and first higher order mode of twin-hole fibres is studied when the distance from the anode to the core changes. Finally, the dispersion relations of optical fibres with circular core, optical fibres with elliptical core and those with rectangular core are compared to clarify the accuracy of the rectangular core approximation used in the previous calculations.

Modified Fourier Decomposition Method [A.1, A.2, A.3] is used to calculate the optical wave guiding properties of the scalar mode of the twin-hole fibres. The guided

modes of the fibre are denoted by E_{mn} (both m and n are integers) with $m-1$ and $n-1$ field zeros in $x-$ and $y-$ directions, respectively.

The twin-hole fibre structure with a rectangular core and two side circular holes is depicted in Fig. A.1 (a) and (b). d_1 and d_2 are diameters of the first and second hole. The two holes are separated by a space s. The two holes are filled with air of the refractive index n_{air}. The distance from the core to the anode is denoted as s_1 and the distance from the core to the cathode is denoted as s_2. $2a$ and $2b$ are the width and height of the rectangular core respectively. As a result, $s = s_1 + 2a + s_2$. The refractive indices of the core and the cladding are denoted as n_{core} and $n_{cladding}$.

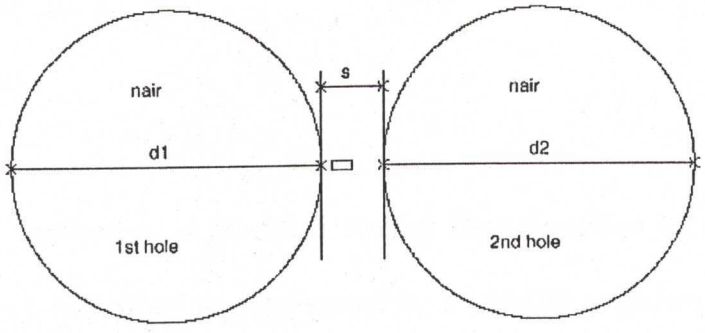

(a)

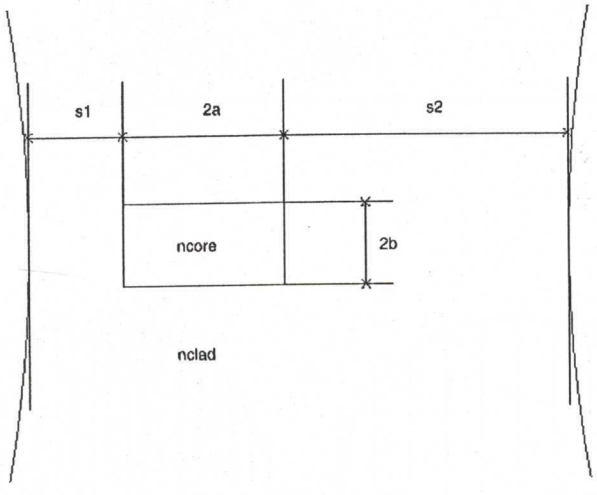

(b)

Fig. A.1 (a) Cross sectional geometry of a twin-hole fibre; (b) core geometry.

A.2 The Modal Field and the Cutoff Wavelength of a Twin-hole Fibre with Rectangular Core

One of the twin-hole fibre devices used for poling has the following parameters for calculations: $d_1 = d_2 = 100$ μm, $s = 20$ μm, $s_1 = 3.5$ μm, $s_2 = 10.5$ μm, $2a = 6$ μm,

$2b = 3$ μm, $n_{air} = 1.0$, $n_{core} = 1.4606$ and $n_{cladding} = 1.4571$. The operating wavelength λ is 0.6328 μm.

In the present application of Modified Fourier Decomposition Method, the circular holes of the twin-hole fibre are represented by rectangles as shown in Fig. A.2. The symmetric property of the structure about the y-axis is implemented in the calculation. 20 rectangles are used in the first hole and 10 rectangles are used in the second hole.

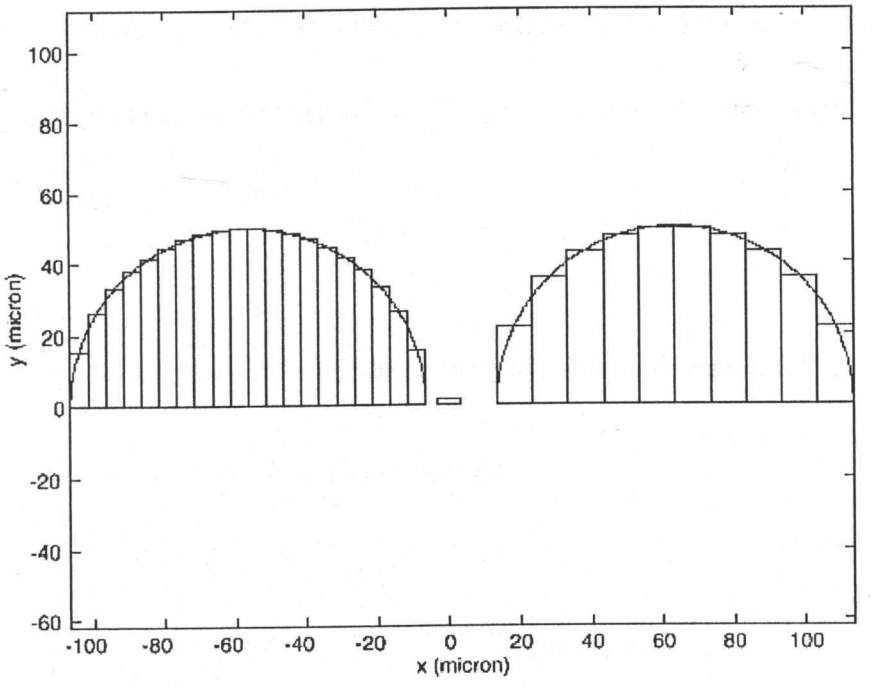

Fig. A.2 Two holes of the fibre are represented by rectangles.

The normalized propagation constant P^2 is defined as

$$P^2 = \frac{\left(\frac{\beta}{\kappa}\right)^2 - n_{clad}^2}{n_{core}^2 - n_{clad}^2}, \tag{A.1}$$

where β is the modal propagation constant and $\kappa = \frac{2\pi}{\lambda}$ is the wave number.

For the above fibre parameters, P^2 for the scalar fundamental mode, E_{11}, is given in Table A.1. The parameter N_m indicates the number of spatial frequency components used in the x-direction. The parameter N_n^e indicates the number of even spatial frequency components used in the y-direction. Accuracy of P^2 up to 4 decimal places is achieved using $N_m \geq 50$ and $N_n^e \geq 25$.

Table A.1 Convergence of the normalized propagation constant P^2 for the scalar fundamental mode E_{11}.

N_m	N_n^e	P^2
20	10	0.48675
30	15	0.48732
40	20	0.48741
50	25	0.48748
60	30	0.48751

The modal field distribution of E_{11} calculated using $N_m = 60$ and $N_n^e = 30$ is shown in Fig. A.3. The contour levels are at 10% interval, i.e. 90%, 80%, ..., 10%. The field distribution is not much affected by the two side holes and maintains its almost symmetrical shape.

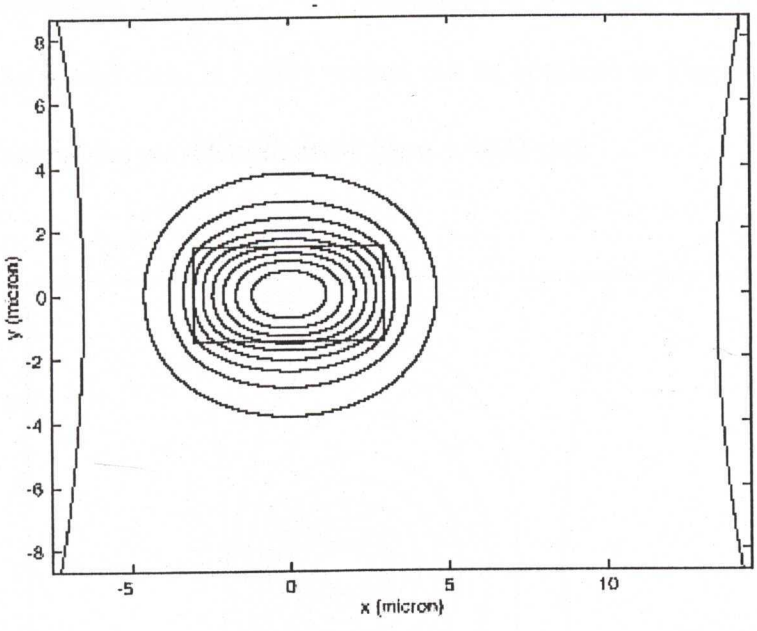

Fig. A.3 E_{11} modal field distribution

The cutoff value V_{co} and cutoff wavelength λ_{co} is related by

$$V_{co} = \frac{2\pi}{\lambda_{co}} \rho (n_{core}^2 - n_{clad}^2)^{\frac{1}{2}}, \tag{A.2}$$

where $\rho = \sqrt{ab}$. For the above fibre parameters, V_{co} for the scalar fundamental mode E_{11} is calculated as 0.9605 and V_{co} for the first higher order mode E_{21} is calculated as 1.8891. Using Eq. A.2, the wavelength range for single mode operation is given by

$$0.7130\mu m \leq \lambda \leq 1.4023\mu m. \tag{A.3}$$

Note that the fundamental mode E_{11} has a finite cutoff wavelength due to presence of two air holes besides the core. Fig. A.4 shows the modal field of the fundamental mode E_{11} at wavelength of 1.4 μm, which is close to cutoff (1.4023 μm). The normalized propagation constant, P^2, is calculated as 0.00088. It is clearly seen in Fig. A.4 that the modal field is highly spread out as opposite to Fig. A.3, where the calculation is done at the wavelength away from 1.4023 μm.

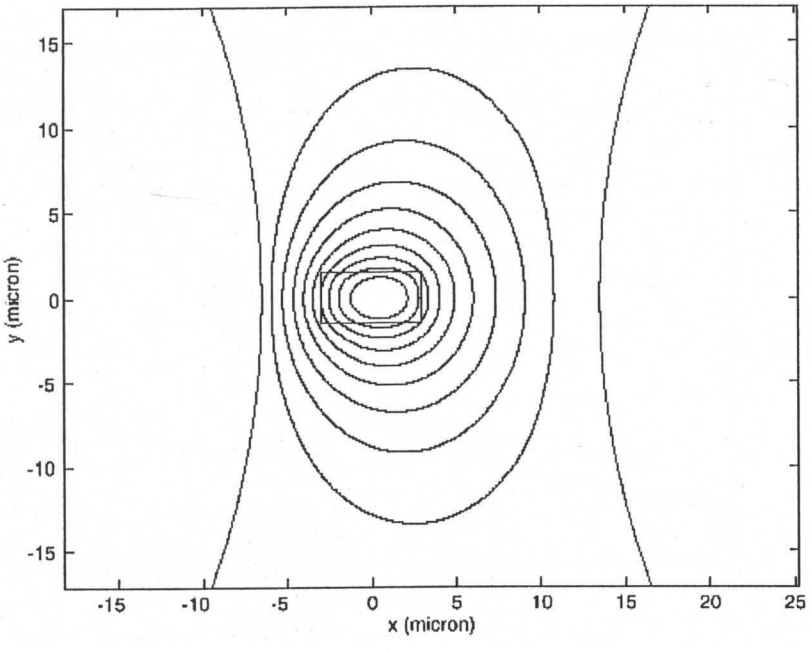

Fig. A.4 E_{11} modal field distribution at wavelength of 1.4 μm, which is close to cutoff (1.4023 μm).

A.3 Effect of the Distance From the Anode to the Core on the Cutoff Value and the Cutoff Wavelength of Twin-hole Fibres

While s_1 is varying from 3.5 μm to 0 μm and s_2 is changing respectively so that the hole spacing $s = s_1 + 2a + s_2$ maintains the same value of 20 μm, the cutoff values V_{co} for the first higher order mode E_{21} are calculated and shown in Fig. A.5.

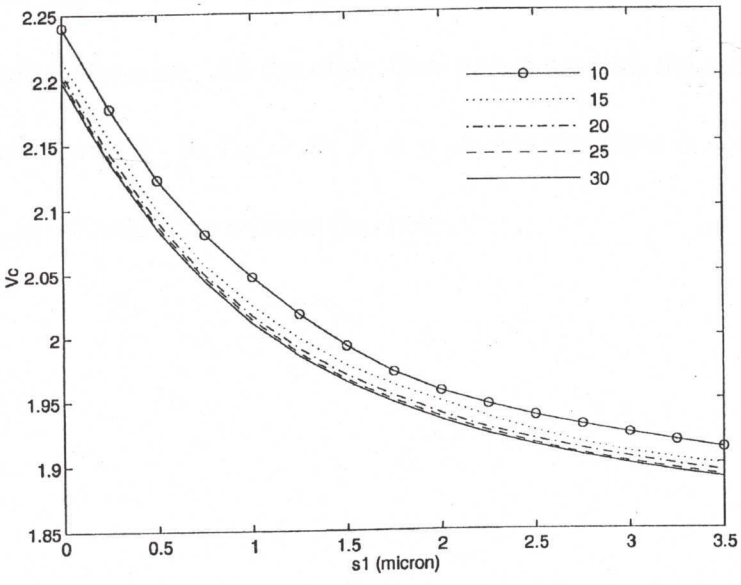

Fig. A.5 E_{21} mode cutoff value V_{co} as a function of s_1. In the graph, 10, 15, ..., 30 mean the accuracy of the computation. The large number is used, the more accurate computation is done.

As shown in the figure, the smaller the distance s_1, the higher the cutoff value V_{co} and the shorter the cutoff wavelength λ_{co}.

A.4 Effect of the Distance from the Anode to the Core on the Modal Fields of both the Fundamental Mode and the First Higher Order Mode of Twin-hole Fibres

To explain the cutoff results obtained in Fig. A.5, the normalized propagation constant P^2 of E_{11} and E_{21} is calculated against V from 0 to 4 as a function of the distance s_1 from the anode to the core. All the other fibre parameters are the same as before and the results are shown as in Fig. A.6. $s_1 = \infty$ means the fibre is considered to be a rectangular core normal fibre without two holes.

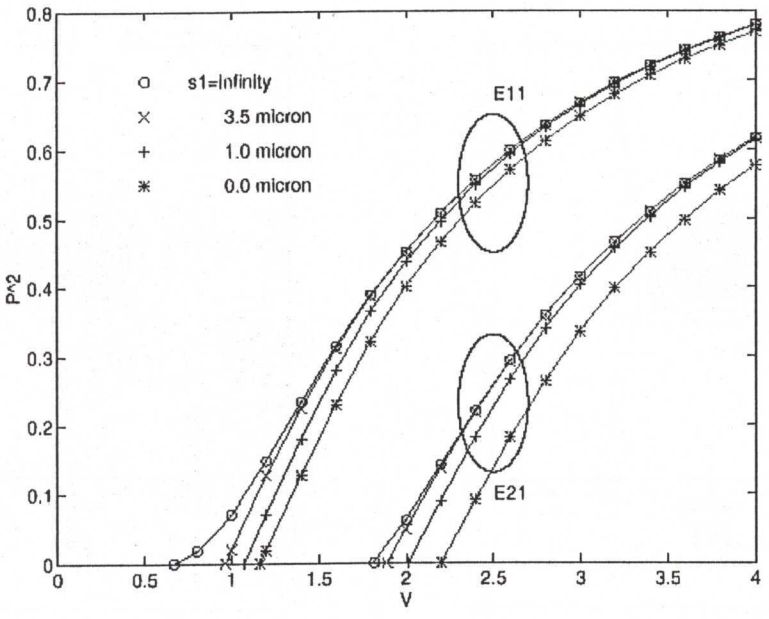

Fig. A.6 Dispersion relation as a function of the anode-to-core distance

It is clearly seen in Fig. A.6 that for E_{11} mode far from its cutoff, say $V > 1.6$, the difference in dispersion relation is tiny between the normal fibre ($s_1 = \infty$) and the twin-hole fibre with $s_1 = 3.5$ μm. For E_{11} mode close to its cutoff, say $V < 1.6$, P^2 of twin-hole fibres is smaller than their corresponding normal fibre without two holes. Among twin-hole fibres with the same V value, P^2 is getting smaller as s_1 decreases from 3.5 μm to 0 μm. This means that twin-hole fibres are less guided while the anode hole is getting closer to the core. To prove this, the modal field of E_{11} is calculated at $V = 1.2$ as a function of s_1. The results are shown in Fig. A.7. The contour levels are at 10% interval, i.e. 90%, 80%, ..., 10%. As shown in the figure, the closer the anode hole to the core, the more the field is pushed away from the core, and the more the field spreads out into the cladding.

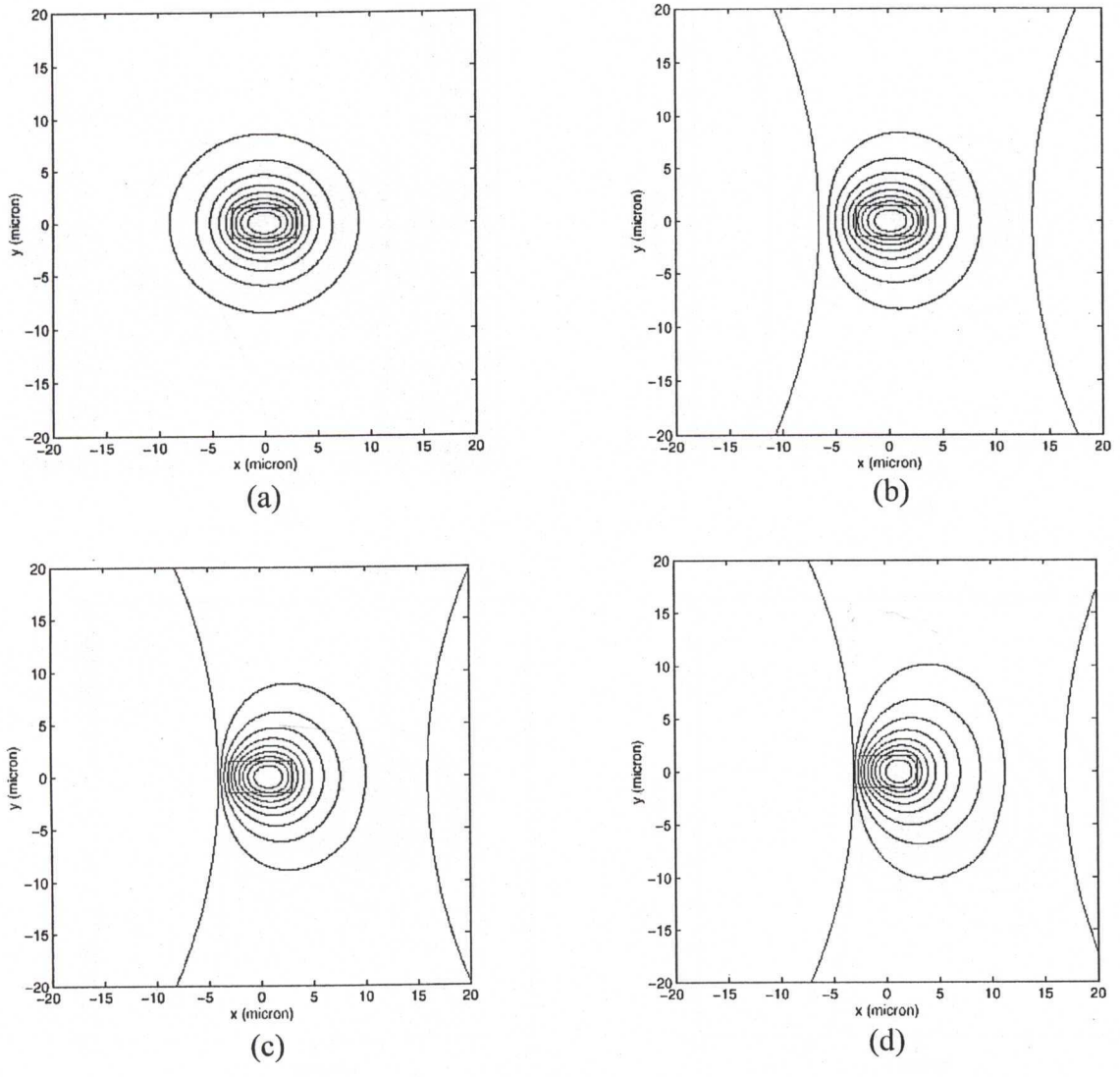

Fig. A.7 (a) E_{11} modal field at $V = 1.2$ and $s_1 = \infty$;

(b) E_{11} modal field at $V = 1.2$ and $s_1 = 3.5$ μm;

(c) E_{11} modal field at $V = 1.2$ and $s_1 = 1.0$ μm;

(d) E_{11} modal field at $V = 1.2$ and $s_1 = 0.0$ μm;

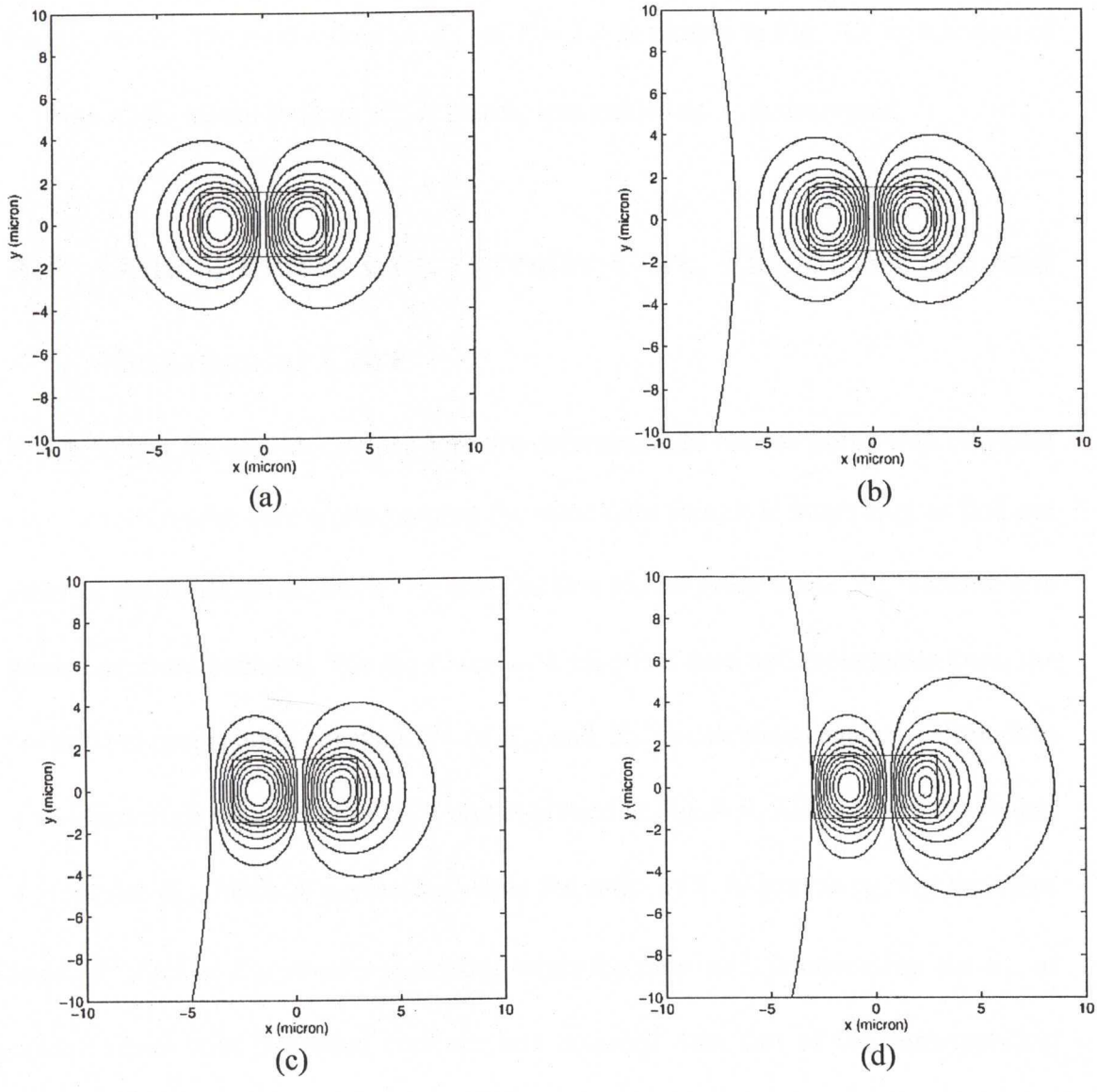

Fig. A.8 (a) E_{21} modal field at $V = 2.3$ and $s_1 = \infty$;

(b) E_{21} modal field at $V = 2.3$ and $s_1 = 3.5$ μm;

(c) E_{21} modal field at $V = 2.3$ and $s_1 = 1.0$ μm;

(d) E_{21} modal field at $V = 2.3$ and $s_1 = 0.0$ μm;

The dispersion relation for the first higher order mode E_{21} displays similar features to the E_{11} mode. The modal field of E_{21} at $V = 2.3$ is plotted in Fig. A.8 as function of s_1. Again, the modal field of E_{21} is getting less guided as s_1 is decreased

A.5 Optical Fibres with Circular Core, Elliptical Core and Rectangular Core

When optical fibres with circular core are deformed into optical fibres with elliptical core or rectangular core while keeping the same core area, it is interesting to find out whether the fundamental mode E_{11} and the first higher order mode E_{21} become less guided or more bounded. For the fibres with elliptical core and rectangular core, the normalized propagation constant P^2 of E_{11} and E_{21} is calculated against V from 0 to 4 at different core aspect ratio a/b and is plotted in Fig. A.9. As shown in the figure, P^2 for the E_{11} mode is decreasing while the ratio a/b is increasing. On the other hand, P^2 for the E_{21} mode is increasing while the ratio a/b is increasing. So E_{11} of optical fibres with deformed core are less bounded than that of the corresponding optical fibres with circular core. Oppositely, E_{21} of optical fibres with deformed core are more bounded than that of the corresponding optical fibres with circular core.

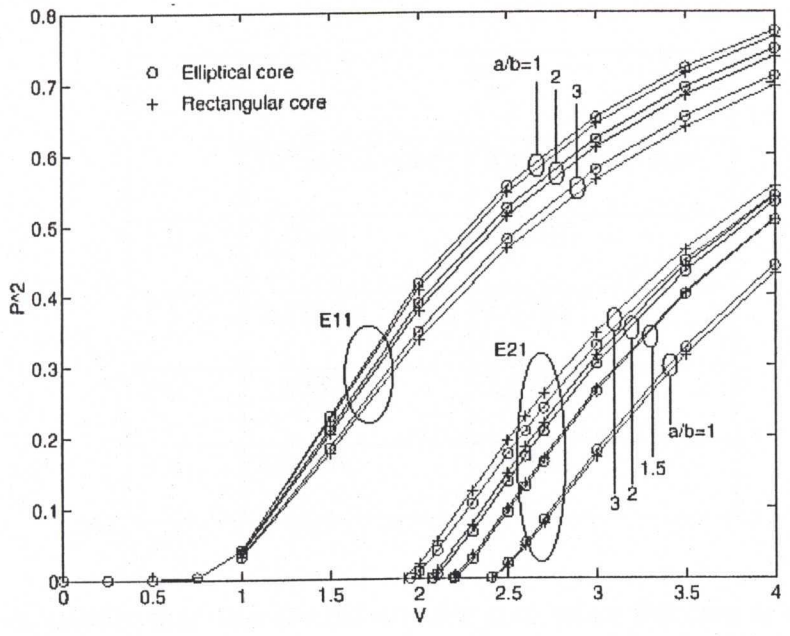

Fig. A.9 Dispersion relations as a function of aspect ratio a/b.

The cutoff value V_{co} of the E_{21} mode is obtained from the V values of the dispersion curve at $P^2 = 0$. Table A.2 summarizes these values V_{co} of optical fibres with elliptical and rectangular core at different aspect ratio a/b.

Table A.2 V_{co} of optical fibres with elliptical and rectangular core at different aspect ratio .

a/b	V_{co}	
	Elliptical core	Rectangular core
1.0	2.4048	2.4107
1.5	2.1916	2.1765
2.0	2.0757	2.0489
3.0	1.9506	1.9123

V_{co} becomes smaller than that for the circular core when the core is deformed. The more the core is deformed the smaller V_{co} becomes. This is because P^2 of E_{21} is increasing as the core is deformed from its circular shape. Since P^2 is larger, its V_{co} at $P^2 = 0$ tends to be smaller. It is also interesting to realize that there is an increasing difference of V_{co} between elliptical core and rectangular core when the core aspect ratio a/b is increased.

A.6 Conclusion

In Section A.2, the modal field of the fundamental mode E_{11} of a twin-hole fibre was calculated. It is interesting to realize that there is a cutoff value for the fundamental mode E_{11} of twin-hole fibre. In contrast, there is no a cutoff for the fundamental mode of a normal fibre without two holes. Section A.3 shows that the cutoff value V_{co} for

the first higher order mode E_{21} increases with the increasing distance s_1 from the core to the anode.

In Section A.4, it was found that E_{11} and E_{21} of twin hole fibres with rectangular core are less guided than their corresponding normal fibre with rectangular core. The modal fields become much less guided as the anode-to-core distance s_1 is decreased. So the cutoff values V_{co} is getting larger as s_1 is decreasing. A twin-hole fibre with larger V value (or larger core size, or shorter wavelength) is needed to counteract the pushing power of air anode hole and bring back modes from cutoff into guiding. The anode-to-core distance $s_1 = 3.5$ μm is a significant distance. As shown by the dispersion curves in Fig. A.6, the guiding properties of the twin-hole fibre with $s_1 \geq 3.5$ are almost the same as the guiding properties of a normal fibre without air holes. So the distance between the two holes (i.e. two electrodes), s_1, can be as close as $2a + 7.0$ μm, and the twin-hole fibre has almost the same optical wave guiding properties as a normal fibre without two holes.

Section A.5 shows that the cutoff value V_{co} for the first higher order mode E_{21} changes with the ratio of the two axes of the elliptical core. For example, when the ratio of the major axis to the minor axis is 2, V_{co} is ~2.0 instead of 2.4048.

A.7 References

[A.1] K. M. Lo, "Theory of Optical Fibre Modal Fields With Application to the Design of Evanescent Field Devices," PhD dissertation, University of Sydney, 1994.

[A.2] S. J. Hewlett and F. Ladouceur, "Fourier decomposition method applied to mapped infinite domains: Scalar analysis of dielectric waveguides down to modal cutoff," J. Lightwave Technol. **13**, 375 (1995).

[A.3] S. J. Hewlett, F. Ladouceur, and J. D. Love, "Second-mode cutoff in rectangular-core couplers using the Fourier decomposition method," Opt. Quantum Electron. **27**, 987 (1995).